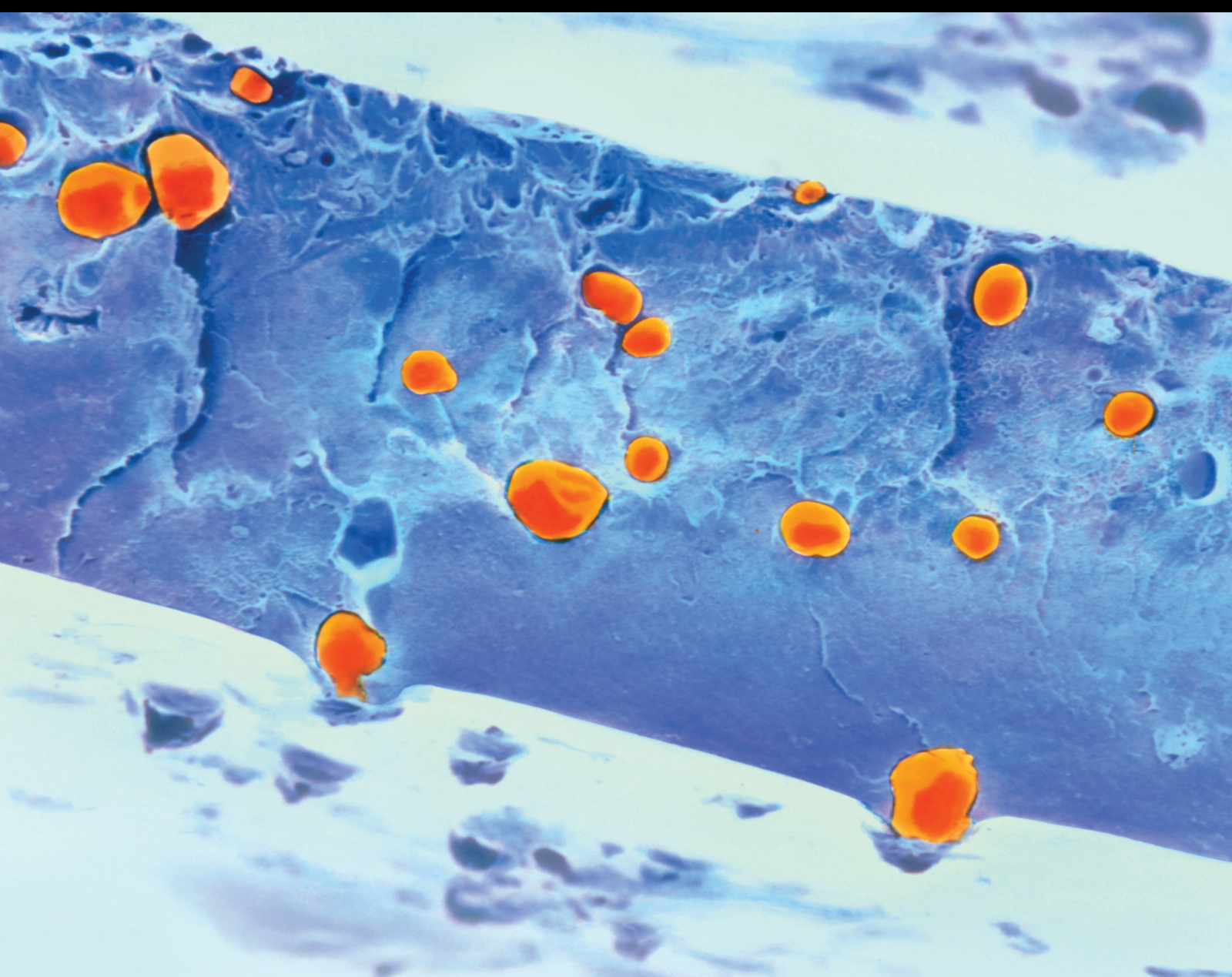


Stimuli-Responsive Smart Polymers and Structures: Characteristics and Applications

Lead Guest Editor: Junshi Zhang

Guest Editors: Gianluca Rizzello, Jianwen Zhao, Qi Shen, and Yanjie Wang



Stimuli-Responsive Smart Polymers and Structures: Characteristics and Applications

International Journal of Polymer Science

Stimuli-Responsive Smart Polymers and Structures: Characteristics and Applications

Lead Guest Editor: Junshi Zhang

Guest Editors: Gianluca Rizzello, Jianwen Zhao, Qi Shen,
and Yanjie Wang



Copyright © 2018 Hindawi. All rights reserved.

This is a special issue published in "International Journal of Polymer Science." All articles are open access articles distributed under the Creative Commons Attribution License, which permits unrestricted use, distribution, and reproduction in any medium, provided the original work is properly cited.

Editorial Board

- | | | |
|-------------------------------|---------------------------------|---------------------------------|
| Domenico Acierno, Italy | Nabil Ibrahim, Egypt | Hossein Roghani-Mamaqani, Iran |
| Luc Averous, France | Patric Jannasch, Sweden | Mehdi Salami-Kalajahi, Iran |
| Christopher Batich, USA | Nobuhiro Kawatsuki, Japan | Markus Schmid, Germany |
| Marc Behl, Germany | J.M. Kenny, Italy | Matthias Schnabelrauch, Germany |
| Laurent Billon, France | Saad Khan, USA | Shu Seki, Japan |
| Antonio Caggiano, Germany | Dirk Kuckling, Germany | Vitor Sencadas, Australia |
| Andrea Camposeo, Italy | Jui-Yang Lai, Taiwan | Robert A. Shanks, Australia |
| Wen Shyang Chow, Malaysia | Ulrich Maschke, France | Vito Speranza, Italy |
| Angel Concheiro, Spain | Subrata Mondal, India | Atsushi Sudo, Japan |
| Yulin Deng, USA | Toribio F. Otero, Spain | Hideto Tsuji, Japan |
| Maria Laura Di Lorenzo, Italy | Alessandro Pegoretti, Italy | Stefano Turri, Italy |
| Eliane Espuche, France | Önder Pekcan, Turkey | Hiroshi Uyama, Japan |
| Antonio Facchetti, USA | Zhonghua Peng, USA | Cornelia Vasile, Romania |
| Gianluca M. Farinola, Italy | Debora Puglia, Italy | Alenka Vesel, Slovenia |
| Marta Fernández-García, Spain | Miriam H. Rafailovich, USA | De-Yi Wang, Spain |
| Peter Foot, UK | Arthur J. Ragauskas, USA | Qinglin Wu, USA |
| Benny Dean Freeman, USA | Anjanapura V. Raghu, India | Huineng Xiao, Canada |
| Peng He, USA | Subramaniam Ramesh, Malaysia | Yiqi Yang, USA |
| Jan-Chan Huang, USA | Bernabé L. Rivas, Chile | Michele Zappalorto, Italy |
| Wei Huang, China | Juan Rodriguez-Hernandez, Spain | |

Contents

Stimuli-Responsive Smart Polymers and Structures: Characteristics and Applications

Junshi Zhang , Gianluca Rizzello, Jianwen Zhao, Qi Shen, and Yanjie Wang 
Editorial (2 pages), Article ID 8202635, Volume 2018 (2018)

Comparison of CMM and Micro-CT Volumetric Analysis of Polyethylene Tibial Knee Inserts in Total Knee Replacement

Wei Jiang , Cuicui Ji, Huaxing Xiao, Zhongmin Jin, and Yuntian Dai
Research Article (7 pages), Article ID 3601480, Volume 2018 (2018)

The Influence of Water and Solvent Uptake on Functional Properties of Shape-Memory Polymers

Ehsan Ghobadi , Axel Marquardt, Elias Mahmoudinezhad Zirdehi , Klaus Neuking, Fathollah Varnik, Gunther Eggeler, and Holger Steeb 
Research Article (15 pages), Article ID 7819353, Volume 2018 (2018)

Experimental and Numerical Study of the Interfacial Shear Strength in Carbon Fiber/Epoxy Resin Composite under Thermal Loads

Hongxiao Wang , Xiaohui Zhang , Yugang Duan, and Lingjie Meng
Research Article (8 pages), Article ID 3206817, Volume 2018 (2018)

Stimuli-Responsive Hydrogels Based on Polyglycerol Crosslinked with Citric and Fatty Acids

Leidy C. Solano-Delgado , César A. Bravo-Sanabria , Carolina Ardila-Suárez, and Gustavo E. Ramírez-Caballero 
Research Article (8 pages), Article ID 3267361, Volume 2018 (2018)

Dynamic Electromechanical Response of a Viscoelastic Dielectric Elastomer under Cycle Electric Loads

Junjie Sheng  and Yuqing Zhang
Research Article (14 pages), Article ID 2803631, Volume 2018 (2018)

Editorial

Stimuli-Responsive Smart Polymers and Structures: Characteristics and Applications

Junshi Zhang , **Gianluca Rizzello**, ² **Jianwen Zhao**, ³ **Qi Shen**, ⁴ and **Yanjie Wang**  ⁵

¹Department of Mechanical and Biomedical Engineering, City University of Hong Kong, Kowloon, Hong Kong

²Department of Systems Engineering, University of Saarland, Saarbrücken, Germany

³Department of Mechanical Engineering, Harbin Institute of Technology, Weihai, China

⁴Active Materials and Smart Living Laboratory, University of Nevada, Las Vegas, Las Vegas, NV, USA

⁵School of Mechanical and Electrical Engineering, Hohai University, Changzhou, China

Correspondence should be addressed to Junshi Zhang; jzhan26@cityu.edu.hk

Received 30 May 2018; Accepted 30 May 2018; Published 4 July 2018

Copyright © 2018 Junshi Zhang et al. This is an open access article distributed under the Creative Commons Attribution License, which permits unrestricted use, distribution, and reproduction in any medium, provided the original work is properly cited.

The functional polymers and structures can be actuated by the external stimulation, including the light, temperature, and electric field. Nowadays, various smart polymers are studied as soft sensors and actuators or are designed to compose the smart structures to own required performances. The typical soft smart polymers involve dielectric elastomers, ionic-polymer metal composites, hydrogel, shape memory polymers, and so on. During recent years, research on the stimuli-responsive polymers and structures has been extensively performed, especially the electro-responsive soft materials. This special issue is aimed at creating a multidisciplinary forum of discussion on the most recent research advances in synthesis, characterization, design, and application of soft smart polymer and structures, providing a potential guided outlook for future studies.

The knowledge and understanding of such functional materials are of great importance for our practical living. In this special issue, some investigations related to stimuli-responsive smart materials are shown, including different topics, such as dielectric elastomer, hydrogel, and shape memory polymer. In the paper “Dynamic Electromechanical Response of a Viscoelastic Dielectric Elastomer under Cycle Electric Loads,” J. Sheng and Y. Zhang explored the nonlinear dynamic performance of the viscoelastic dielectric elastomer when the AC voltage is applied. In this study, a thermodynamic model is set up to characterize the influence of viscoelasticity on the electromechanical and dynamic response of a viscoelastic DE. The time-dependent dynamic

deformation, the hysteresis, and the dynamic stability undergoing viscoelastic dissipative processes are investigated. In the paper “Stimuli-Responsive Hydrogels Based on Polyglycerol Crosslinked with Citric and Fatty Acids,” three hydrogels were studied with varying molar ratios of a crosslinking agent. It was found that crosslink amount, type, and size play a crucial role in swelling, thermal, mechanical, and stimuli-responsive properties. In the paper “Experimental and Numerical Study of the Interfacial Shear Strength in Carbon Fiber/Epoxy Resin Composite under Thermal Loads,” H. Wang et al. examined the influence mechanism of temperature on the interfacial shear strength between carbon fiber and epoxy resin matrices under various thermal loads using experimental and numerical simulation methods. To evaluate the change in IFSS as a function of the increase in temperature, a microbond test was performed under a controlled temperature environment from 23°C to 150°C. In the paper “The Influence of Water and Solvent Uptake on Functional Properties of Shape-Memory Polymers,” E. Ghobadi et al. have investigated the effects of different solvents (i.e., water, acetone, and ethanol) on the functional properties of SMP, by means of both experiments and numerical simulations. The aim of the proposed study is to understand whether targeted physical aging “prior to programming” can influence the functional properties of a commercially available SMP (Estane, Lubrizol, Oevel, Westerlo, Belgium). In the paper “Comparison of CMM and Micro-CT Volumetric Analysis of Polyethylene Tibial Knee Inserts

in Total Knee Replacement," W. Jiang et al. investigated the ultrahigh molecular weight polyethylene (UHMWPE) bearings, which are used for orthopaedic joint replacement. CMM and micro-CT measurement techniques are used for volumetric loss with gravimetric measurement as the reference. The comparison results indicate that gravimetric measurement remains the gold standard and the CMM measurement took less time and had better precision, accuracy, and repeatability compared to the micro-CT measurement technique.

Acknowledgments

We thank all the authors for their invaluable contributions and the reviewers for taking their invaluable time to review for this special issue.

*Junshi Zhang
Gianluca Rizzello
Jianwen Zhao
Qi Shen
Yanjie Wang*

Research Article

Comparison of CMM and Micro-CT Volumetric Analysis of Polyethylene Tibial Knee Inserts in Total Knee Replacement

Wei Jiang¹, Cuicui Ji,² Huaxing Xiao,¹ Zhongmin Jin,³ and Yuntian Dai¹

¹School of Mechanical and Automobile Engineering, Changzhou Institute of Technology, Changzhou, Jiangsu 213032, China

²School of Mechanical and Electrical Engineering, Hohai University, Changzhou, Jiangsu 213022, China

³Leeds Joint School, Southwest Jiaotong University, Chengdu, Sichuan 611756, China

Correspondence should be addressed to Wei Jiang; jwei@czust.edu.cn

Received 29 December 2017; Revised 22 March 2018; Accepted 22 April 2018; Published 19 June 2018

Academic Editor: Qi Shen

Copyright © 2018 Wei Jiang et al. This is an open access article distributed under the Creative Commons Attribution License, which permits unrestricted use, distribution, and reproduction in any medium, provided the original work is properly cited.

Ultrahigh molecular weight polyethylene (UHMWPE) bearings are used widely in orthopaedic joint replacement as a prominent material for improving the longevity, which is dramatically influenced by wear of polyethylene. Polyethylene tibial knee components from knee simulators under two different input conditions were analyzed using CMM and Micro-CT measurement techniques for volumetric loss with gravimetric measurement as reference. Based on the coordinates and image slices obtained, the surface curve fitting and image digitization methodology were used for the creation of nominal “original” surface in the case of no prewear data provided. The comparison results indicate that gravimetric remains the gold standard and the CMM measurement took less time and had better precision, accuracy, and repeatability compared to Micro-CT measurement technique.

1. Introduction

As an outstanding material for orthopaedic joint replacement, polyethylene can provide excellent abrasion resistance, low friction, high impact resistance, a self-lubricating surface, insignificant water absorption, good chemical resistance, high-energy absorption, and no temperature sensitivity in the human biological environment [1]. Ultrahigh molecular weight polyethylene (UHMWPE) components are being widely used in total knee replacement (TKR) as a bearing surface to improve the longevity, if well designed and properly implanted, products made of this material can function for more than fifteen years or even longer. Currently, the major issue in TKR is the wear of polyethylene and results in more than 16% failure of TKR [2]. Thus, wear measurement is very important for accurate determination of wear rate and volume loss in total knee replacements. The most standard method is gravimetric analysis [3, 4]. However, the fundamental issue with gravimetric measurement is that it needs a reference from which to calculate the wear. In addition, gravimetric measurement has limitations such as inclusion of wear debris in the polyethylene component, transfer of materials into the tibial tray, changes in mass of the

Polyethylene due to fluid uptake, and the cementation of the components [5], which may result in inaccurate volumetric determination from gravimetric analysis [6]. Since it is necessary to have a reference measurement for gravimetric analysis, it is not possible to use this method for retrieved samples. Therefore, to avoid these disadvantages, advanced volumetric measurement techniques such as coordinate measuring machine (CMM) [7] and micro computed topography (Micro-CT) [8, 9] have been used to determine the volume change of polyethylene in hip, knee, and spinal replacement devices and validated for accuracy and repeatability. The aim of this study was to compare CMM (Legex 322, Mitutoyo) and Micro-CT 100 (Scanco Medical, Busseldorf, Switzerland) measurement techniques for volumetric measurement of knee simulator specimen using gravimetric measurement of volume loss as reference.

2. Materials and Methods

A total of 12 UHMWPE tibial knee components (DePuy, UK), which were tested in six station knee simulators (University of Leeds, UK), were used for measurement. The wear tests were carried out by a colleague within the research

institution (C. Brockett) in 2009 and 2011 [10]. Two input profiles were used for the specimens, one is the ISO setup and the other is a standard CR150. Both CMM and Micro-CT measurement techniques were applied to obtain the three-dimensional (3-D) surface coordinates and images slices, respectively. In addition, the images slices acquired via Micro-CT were then transferred into coordinates with the help of image digitization. Therefore, the 3-D surface coordinates acquired from CMM and Micro-CT were analyzed volumetrically to investigate the comparison of those measurement techniques. Since prewear data such as original drawings and CAD models are not always available to determine the volume loss of tibial knee components, the original surface needs to be reconstructed. In this study, a 5th order polynomial curve surface fitting algorithm (1) was applied for the generation of original 3-D surface on the basis of undeformed region, which proved its effectiveness and accuracy based on simulated volume removal and computational tests (maximum errors equal to 0.2 mm^3 and 1.1 mm^3 , resp.) [11]. Prior to the surface fitting process, the wear region should be distinguished and removed from the database for accurate original surface reconstruction, which was considered as prewear data for volumetric analysis. As demonstrated in Figure 1, the wear region was determined according to the difference of Z value between two adjacent coordinates, it can be judged to be worn out when the difference is greater than 0.1 mm . It is worth noting that some clearly wrong coordinates need to be removed for accurate wear region identification. The methodologies of CMM and Micro-CT for volumetric measurements are detailed below.

$$\begin{aligned} f(x, y) = & P00 + P10x + P01y + P20x^2 + P11xy + P02y^2 \\ & + P30x^3 + P21x^2y + P12xy^2 + P03y^2 + P40x^4 \\ & + P31x^3y + P22x^2y^2 + P13xy^3 + P04y^4 + P50x^5 \\ & + P41x^4y + P32x^3y^2 + P23x^2y^3 + P14xy^4 + P05y^5, \end{aligned} \quad (1)$$

where P_{ij} are parameters in polynomial surface fitting algorithm, i is the degree in x , and j is the degree in y .

2.1. CMM. For CMM measurement, Trigene (MediChem International Ltd., Seven Oaks, UK) was used to clean the specimen before measurement. After removing from the knee simulator, the polyethylene inserts were cleaned using detergent water then soaked in 1% Trigene solution for 30 minutes to remove all visible serum and contaminants from the surface. Then, the inserts were soaked in isopropanol solution (Fisher Scientific, Loughborough, UK) mixed with water (70% isopropanol:30% water) and placed in an ultrasonic bath (VWR Labshop, IL, USA) for 10 minutes (IMBE simulator test protocol, Leeds University, UK). Afterwards, the components were stored in the weighing room, which is temperature and humidity controlled (21°C and 40%, resp.) and allowed to stabilize for a period of 48 hours. The change in mass was assessed using the AT 201 balance (Mettler Toledo Inc., Columbus, Ohio, USA), and the volumetric loss was calculated using the following equation, taking the

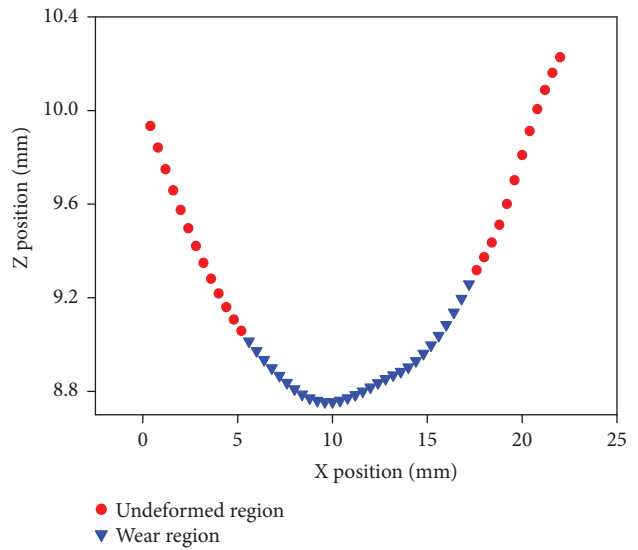


FIGURE 1: Identification of undeformed region.

density of polyethylene as 0.931 g/mm^3 [12]. The samples were measured using CMM (Legex 322, Mitutoyo, UK) with known wear volume determined using gravimetric analysis. It is important to note that the scan interval could influence the volumetric determination dramatically. As a result, an investigation of the influence of the CMM scan interval (0.1 mm, 0.2 mm, 0.5 mm, 1.0 mm, 1.5 mm, and 2.0 mm) was performed using an unworn tibial knee insert and the results indicate that with the increasing of CMM scan interval, the points decreased from 31,133 to 90 and the time consumed decreased from more than 8 hours to nearly 2 minutes, which result in the increase of volume difference from 0.1 mm^3 to 8.1 mm^3 (Figure 2). Therefore, 0.2 mm scan interval was used in this study to maintain the equilibrium between accuracy and time consumed. As illustrated in Figure 3, since there was no initial surface data provided, the coordinates of each condyle surface were measured and surface curve fitting methodology was used for volumetric analysis based on the reconstructed “original” surface [13]. The results obtained were compared against gravimetric measurements.

2.2. Micro-CT. For Micro-CT measurement, an accurate threshold was the key parameter for volumetric analysis using Micro-CT (Scanco Medical, Busseldorf, Switzerland). There are two methods to determine the threshold: one is based on gravimetric analysis and the other is reference to a known volume cylindrical reference specimen. Known volumetric difference from gravimetric measurement was essential for the first method to calculate the amount of wear in Micro-CT. However, the specimens before wear were not available. Hence, the latter method was used in this study to determine the threshold based on a cylindrical reference specimen with same material and known volume (936 mm^3). The in-built software image processing language (IPL) was applied to determine the threshold as 665. With the obtained threshold, two-dimensional greyscale image slices were transferred from original ISQ file and stored in

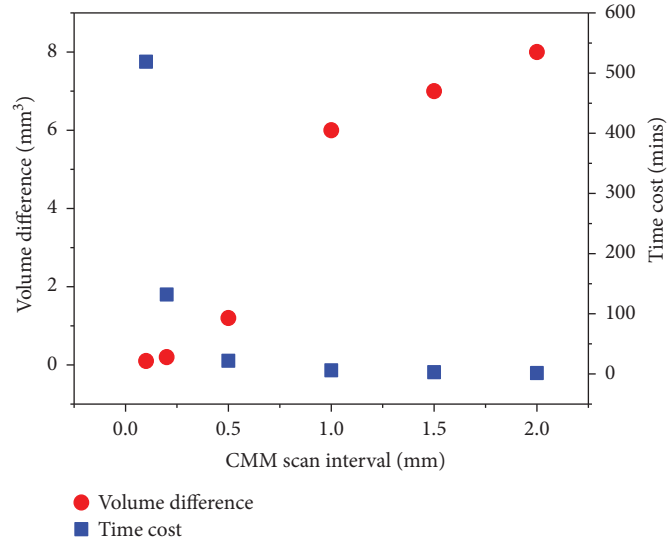


FIGURE 2: The influence of CMM scan interval on volume difference.

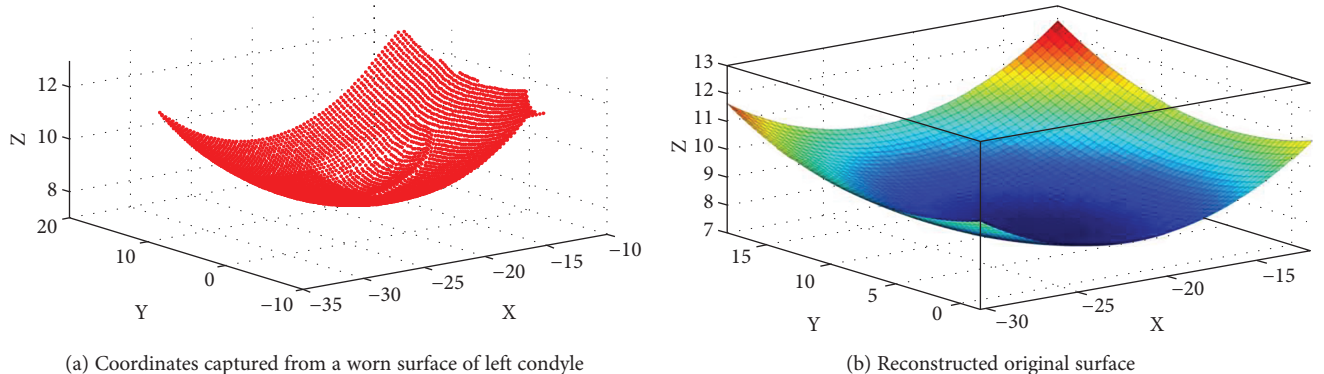


FIGURE 3: Surface coordinates obtained using CMM and reconstructed original surface for volumetric assessment.

the form of TIFF images and local iterative fitting method was used for 3-D reconstruction. Based on the image digitization method [13], the surface coordinates of the specimens were obtained for determination of the volume loss of the polyethylene specimens using surface curve fitting methodology. All measurements were performed three times on each specimen to determine an average volume change and 95% confidence limits (CL) calculated, to determine the repeatability of the measurement method. Table 1 demonstrates the parameters of Micro-CT scanner 100 during scanning, and the schematic diagram of Micro-CT procedure is illustrated in Figure 4.

3. Results and Discussion

The comparison of CMM and Micro-CT methodologies against gravimetric is shown in Table 2. At lower volumes, the volume calculated using CMM and Micro-CT measurement was close to gravimetric analysis. At higher volumes, both CMM and Micro-CT measurement overestimated wear compared to gravimetric volume and the volume loss determined using Micro-CT was higher than CMM. The measurement time cost for the CMM and Micro-CT was

approximately 40 minutes and 90 minutes per scan, respectively. It can be seen from Figure 5 that both CMM and Micro-CT measurement appear to be an overestimate compared to gravimetric measurement. Gravimetric measurement methodology is the standard method used in the determination of volume loss [3, 4]. However, fluid absorption and metallic debris inclusion may affect the measurement. Methodologies with greater accuracy and repeatability without these limitations are required. CMM and Micro-CT measurement techniques were used in this project to determine the volume loss of polyethylene tibial knee specimens and compared against gravimetric analysis, which was considered as the reference. However, it should be noticed that gravimetric measurement does not include creep whereas CMM and Micro-CT do as they are geometry-based measurement techniques. Besides, backside wear will be included in gravimetric measurement but not in CMM/Micro-CT in this project since geometry changes only in the left and right condyles of the tibial knee components were considered.

In this study, both CMM and Micro-CT analysis were based on the coordinates of the articulating surface. For CMM measurement, the coordinates were obtained directly from the scanning probe and stored on the PC in the form

TABLE 1: Scanning parameters of Micro-CT100.

Peak voltage	Current	Specimen holder	Integration time	Resolution	Gaussian
70 kVp	114 μ A	74 mm	300 ms	1024 \times 1024	0.8, 1

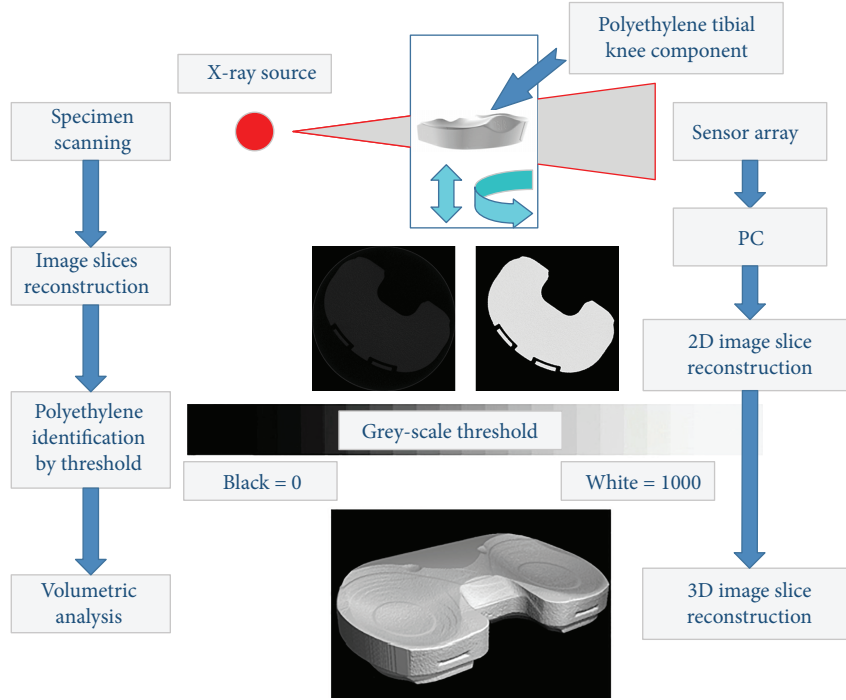


FIGURE 4: Schematic diagram of Micro-CT procedure.

TABLE 2: CMM and Micro-CT volumetric measurement results.

Specimen	Gravimetric (mm ³)	CMM (mm ³)	Micro-CT (mm ³)
Specimen 1	20.12	22.85	23.31
Specimen 2	18.41	19.52	21.15
Specimen 3	9.12	10.05	11.16
Specimen 4	9.96	10.87	11.86
Specimen 5	14.90	16.78	16.18
Specimen 6	11.02	12.16	13.35
Specimen 7	45.74	49.39	51.56
Specimen 8	38.87	41.76	45.47
Specimen 9	49.92	52.57	55.95
Specimen 10	47.44	51.26	53.68
Specimen 11	40.06	43.65	42.54
Specimen 12	37.47	39.61	41.39

of txt file for analysis. For Micro-CT measurement, the two-dimensional greyscale images were transferred into coordinates for volumetric analysis. The threshold is a key parameter in Micro-CT scanning and may vary depending on the type and manufacturer of the polyethylene tibial knee components [14]. It has been reported that differences in the measured volumetric wear may be due to errors in thresholding and in the scanner which affect the intensity of the image

[15]. In order to obtain accurate surface geometry, a known volume reference specimen with the same material and X-ray absorption as the specimens measured was used to determine the threshold, which was the most important parameter for image digitization. However, even with the determined threshold, the average repeatability of Micro-CT ($\pm 3.26 \text{ mm}^3$) was still higher than that of gravimetric measurement ($\pm 0.02 \text{ mm}^3$). The CMM ($\pm 0.89 \text{ mm}^3$) had better repeatability than Micro-CT, but still higher than gravimetric. Concordance correlation coefficients (CCC) [16] were used to evaluate the two measurement techniques against gravimetric measurement. As demonstrated in Figures 6(a) and 6(b), both CMM and Micro-CT measurement indicated higher wear compared to gravimetric analysis. With the help of web tool created by Lin and validated by Yu [17], the CCC, precision (Pearson correlation coefficient measuring how closely the observations deviate from the best-fit line), and accuracy (the closeness of the observations and target values in terms of both means and variances) coefficients were calculated, which are illustrated in Table 3. CMM (CCC = 0.990 and 0.979 for statistic and 95% CL, resp.) measurement shows a higher concordance than Micro-CT measurement (CCC = 0.975 and 0.947 for statistic and 95% CL, resp.) versus the gravimetric analysis, this is more likely due to the thresholding in Micro-CT and image digitization from two-dimensional greyscale image slices. Besides, both precision (1.000 and

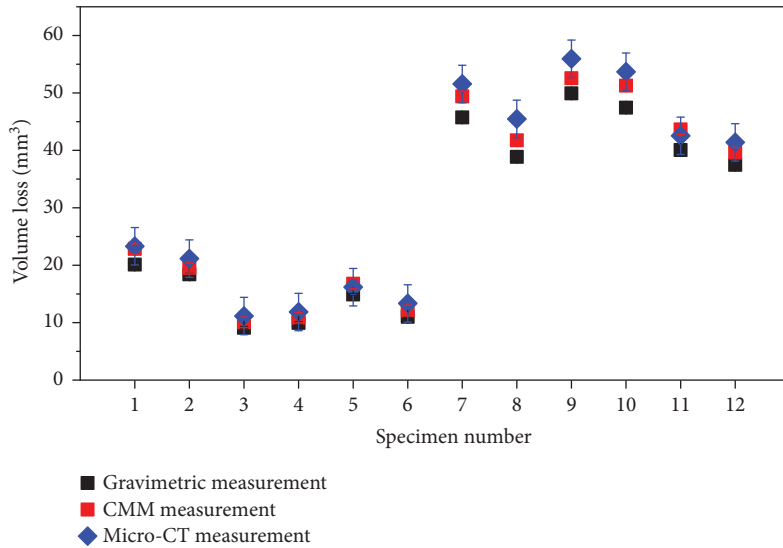


FIGURE 5: CMM and Micro-CT measurement results of laboratory specimens with 95% confidence limit.

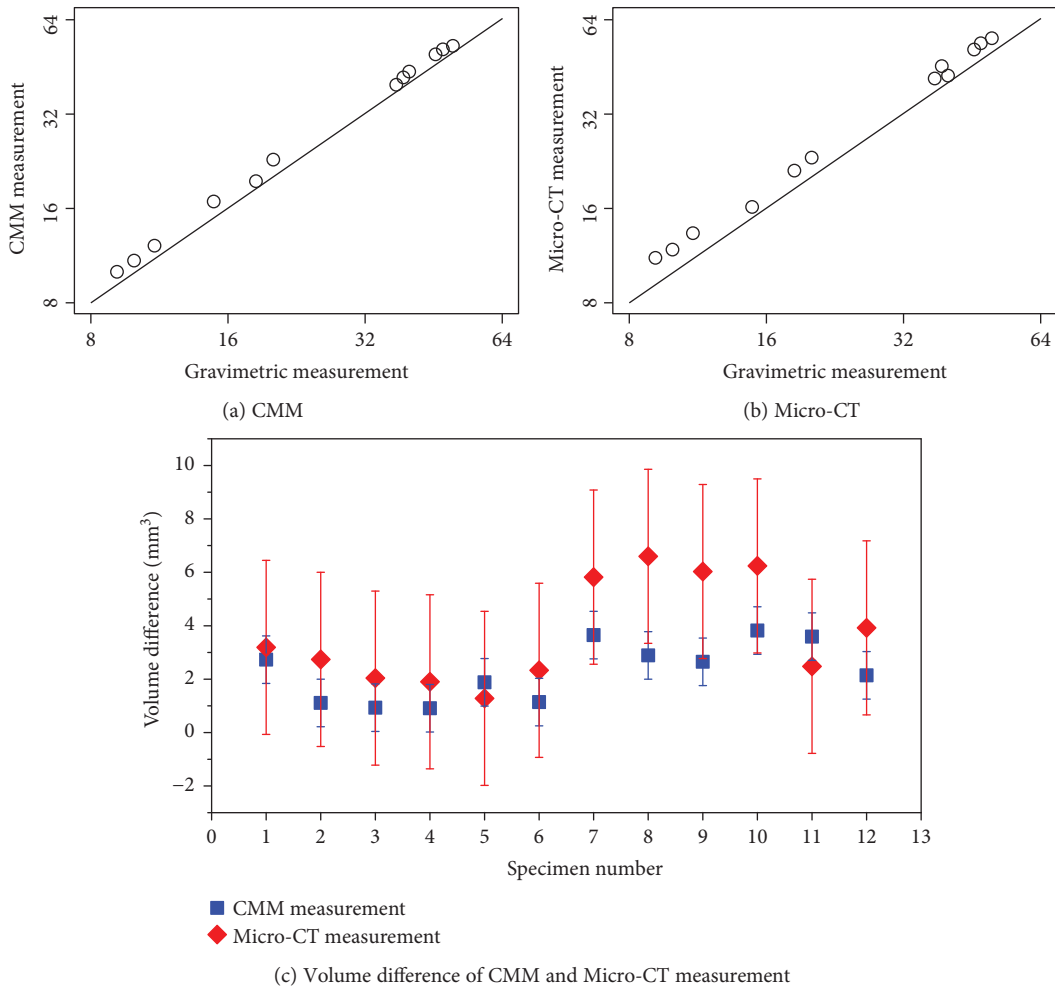


FIGURE 6: Comparison of CMM and Micro-CT volumetric analysis against gravimetric measurement.

0.999 for statistic and 95% CL, resp.) and accuracy (0.999 and 0.996 for statistic and 95% CL, resp.) of CMM measurement were greater than Micro-CT. In addition, as demonstrated in

Figure 6(c), the minimum and maximum volume difference of CMM analysis was 0.91 mm^3 and 3.82 mm^3 . The corresponding volume difference of Micro-CT analysis was

TABLE 3: CMM and Micro-CT measurement versus gravimetric measurement.

CMM measurement versus gravimetric measurement			
	CCC	Precision	Accuracy
Statistic	0.990	1.000	0.991
95% CL	0.979	0.999	0.980
Micro-CT measurement versus gravimetric measurement			
	CCC	Precision	Accuracy
Statistic	0.975	0.999	0.976
95% CL	0.947	0.996	0.949

1.90 mm³ and 6.60 mm³. These studies indicated that CMM had better precision and accuracy compared to Micro-CT analysis. Nevertheless, the voxel size used in the Micro-CT analysis was 79 µm and studies show that the volumetric measurements would be underestimated with the increasing of voxel size [18], lower voxel size and higher resolution could result in better volumetric determination compared to CMM measurement with scan interval of 0.2 mm, which needs further analysis.

Since the IPL software can determine the volume of the specimen, Micro-CT can also be used to determine the volume loss with reference data provided [19, 20], which is like gravimetric measurements. However, for retrievals or cases similar to the present study, due to the absence of prewear data, the reference surface is not available, surface curve fitting methodology based on CMM coordinates and image digitization would be more appropriate to determine the volume loss. Gravimetric measurement was used as reference in this study to investigate the surface curve fitting methodology based on CMM and Micro-CT measurement techniques. Both CMM and Micro-CT can be used for retrievals when no prewear data exists; however, more specimens should be measured to investigate the applicability and accuracy of the method at higher volume loss, especially when no unworn area was available as reference for surface curve fitting.

4. Conclusions

In summary, gravimetric volume analysis remains the most accurate and easiest method to determine the volume loss of polyethylene specimens. However, gravimetric analysis cannot be used at all for retrieval studies, which is an important area of interest in clinical performance. CMM and Micro-CT are alternative measurement techniques used for volume loss determination. In the study, scan interval of 0.2 mm was adopted to balance the accuracy and time cost for CMM measurement and a known volume cylindrical reference with the same material was used for accurate greyscale threshold determination. Since no prewear data was available for reference, a 5th polynomial surface curve fitting algorithm was performed to reconstruct a nominal “original” surface based on the unworn surface. In addition, both CMM and Micro-CT techniques could determine the back-side wear of tibial knee inserts, which is not available for gravimetric measurement. The CMM measurement took

less time and had better precision, accuracy, and repeatability compared to Micro-CT measurement technique.

Conflicts of Interest

The authors declare that there is no conflict of interest regarding the publication of this paper.

Acknowledgments

This research is part of Wei Jiang’s PhD thesis in the University of Leeds and was supported by the EPSRC, the Centre of Excellence in Medical Engineering funded by the Wellcome Trust and by the NIHR Leeds Musculoskeletal Biomedical Research Unit (LMBRU), the Applied Basic Research Programs of Science and Technology Commission Foundation of Jiangsu Province (BK20150256), the National Natural Science Foundation of China (51505126), the Prospective Project of Jiangsu Science and Technology Department (BY2016031-02), and Scientific Research Foundation of Changzhou Institute of Technology (YN1512, YN1626).

References

- [1] S. M. Kurtz, *UHMWPE Biomaterials Handbook: Ultra High Molecular Weight Polyethylene in Total Joint Replacement and Medical Devices*, Academic Press, 2009.
- [2] B. C. Carr and T. Goswami, “Knee implants - review of models and biomechanics,” *Materials & Design*, vol. 30, no. 2, pp. 398–413, 2009.
- [3] S. Affatato, B. Bordini, C. Fagnano, P. Taddei, A. Tinti, and A. Toni, “Effects of the sterilisation method on the wear of UHMWPE acetabular cups tested in a hip joint simulator,” *Biomaterials*, vol. 23, no. 6, pp. 1439–1446, 2002.
- [4] D. D. D’Lima, J. C. Hermida, P. C. Chen, and C. W. Colwell, “Polyethylene cross-linking by two different methods reduces acetabular liner wear in a hip joint wear simulator,” *Journal of Orthopaedic Research*, vol. 21, no. 5, pp. 761–766, 2003.
- [5] P. Bills, L. Blunt, and X. Jiang, “Development of a technique for accurately determining clinical wear in explanted total hip replacements,” *Wear*, vol. 263, no. 7-12, pp. 1133–1137, 2007.
- [6] L. A. Blunt, P. J. Bills, X. Q. Jiang, and G. Chakrabarty, “Improvement in the assessment of wear of total knee replacements using coordinate-measuring machine techniques,” *Proceedings of the Institution of Mechanical Engineers, Part H: Journal of Engineering in Medicine*, vol. 222, no. 3, pp. 309–318, 2008.
- [7] M. Spinelli, S. Carmignato, S. Affatato, and M. Viceconti, “CMM-based procedure for polyethylene non-congruous unicompartmental knee prosthesis wear assessment,” *Wear*, vol. 267, no. 5-8, pp. 753–756, 2009.
- [8] M. G. Teeter, D. D. R. Naudie, K. D. Charron, and D. W. Holdsworth, “Three-dimensional surface deviation maps for analysis of retrieved polyethylene acetabular liners using micro-computed tomography,” *Journal of Arthroplasty*, vol. 25, no. 2, pp. 330–332, 2010.
- [9] S. Affatato, F. Zanini, and S. Carmignato, “Quantification of wear and deformation in different configurations of polyethylene acetabular cups using micro X-ray computed tomography,” *Materials*, vol. 10, no. 3, p. 259, 2017.

- [10] C. Brockett, A. Abdelgaiad, T. Haythornthwaite, C. Hardaker, J. Fisher, and L. Jennings, “The influence of simulator input conditions on the wear of total knee replacements: An experimental and computational study,” *Proceedings of the Institution of Mechanical Engineers, Part H: Journal of Engineering in Medicine*, vol. 230, no. 5, pp. 429–439, 2016.
- [11] W. Jiang, C. Ji, Z. Jin, and Y. Dai, “CMM-based volumetric assessment methodology for polyethylene tibial knee inserts in total knee replacement,” *Applied Bionics and Biomechanics*, vol. 2018, Article ID 9846293, 6 pages, 2018.
- [12] C. L. Brockett, L. M. Jennings, and J. Fisher, “The wear of fixed and mobile bearing unicompartmental knee replacements,” *Proceedings of the Institution of Mechanical Engineers, Part H: Journal of Engineering in Medicine*, vol. 225, no. 5, pp. 511–519, 2011.
- [13] J. Wei, J. Fisher, Z. Jin, K. W. Ruth, and C. L. Brockett, *Wear Measurement of Polyethylene Components in Total the Knee Replacement*, [PhD Thesis], University of Leeds, Leeds, LS2 9JT, UK, 2014.
- [14] N. Otsu, “A threshold selection method from gray-level histograms,” *IEEE Transactions on Systems, Man, and Cybernetics*, vol. 9, no. 1, pp. 62–66, 1979.
- [15] V. Kinzel, M. Scaddan, B. Bradley, and D. Shakespeare, “Varus/valgus alignment of the femur in total knee arthroplasty. Can accuracy be improved by pre-operative CT scanning?,” *The Knee*, vol. 11, no. 3, pp. 197–201, 2004.
- [16] L. Lin, “Overview of agreement statistics for medical devices,” *Journal of Biopharmaceutical Statistics*, vol. 18, no. 1, pp. 126–144, 2007.
- [17] L. Lin, A. S. Hedayat, and W. Wu, *Statistical Tools for Measuring Agreement*, Springer, 2012.
- [18] D. Maret, N. Telmon, O. A. Peters et al., “Effect of voxel size on the accuracy of 3D reconstructions with cone beam CT,” *Dentomaxillofacial Radiology*, vol. 41, no. 8, pp. 649–655, 2012.
- [19] M. G. Teeter, J. S. Milner, D. D. R. Naudie, and S. J. MacDonald, “Surface extraction can provide a reference for micro-CT analysis of retrieved total knee implants,” *The Knee*, vol. 21, no. 4, pp. 801–805, 2014.
- [20] M. G. Teeter, D. D. R. Naudie, D. D. McErlain et al., “In vitro quantification of wear in tibial inserts using microcomputed tomography,” *Clinical Orthopaedics and Related Research®*, vol. 469, no. 1, pp. 107–112, 2011.

Research Article

The Influence of Water and Solvent Uptake on Functional Properties of Shape-Memory Polymers

Ehsan Ghobadi¹, Axel Marquardt,² Elias Mahmoudinezhad Zirdehi¹,³ Klaus Neuking,² Fathollah Varnik,³ Gunther Eggeler,² and Holger Steeb^{1,4}

¹Institute of Applied Mechanics (CE), University of Stuttgart, Stuttgart, Germany

²Institute for Materials, Ruhr-University Bochum, Bochum, Germany

³ICAMS, Ruhr-University Bochum, Bochum, Germany

⁴SimTech, University of Stuttgart, Stuttgart, Germany

Correspondence should be addressed to Ehsan Ghobadi; ehsan.ghobadi@mechbau.uni-stuttgart.de

Received 28 December 2017; Revised 8 April 2018; Accepted 8 May 2018; Published 28 May 2018

Academic Editor: Gianluca Rizzello

Copyright © 2018 Ehsan Ghobadi et al. This is an open access article distributed under the Creative Commons Attribution License, which permits unrestricted use, distribution, and reproduction in any medium, provided the original work is properly cited.

In this contribution, diffusion of water, acetone, and ethanol into a polymer matrix has been studied experimentally and numerically by finite element approaches. Moreover, the present study reports an assessment of different thermomechanical conditions of the shape-memory (SM) performance, for example, stress- or strain-holding times in stress- or strain-controlled thermomechanical cycles and the effect of maximum strain. According to the results presented here, the uptake of acetone in Estane is much higher than ethanol and follows classical Fickian diffusion. Further, a series of thermomechanical measurements conducted on dry and physically (hydrolytically) aged polyether urethanes revealed that incorporation of water seems to have an appreciable impact on the shape recovery ratios which can be attributed to the additional physical crosslinks. However, no obvious difference in shape fixation of dry and physically (hydrolytically) aged samples could be recognized. Furthermore, by decreasing the strain-holding time, shape recovery improves significantly. Moreover, the shape fixity is found to be independent of holding time. The shape recovery ratio decreased dramatically with an increase in the stress-holding time.

1. Introduction

The thermally induced shape-memory effect (SME) of a system is an ability to maintain a temporarily fixed deformation that is established after the application of a specific thermomechanical treatment called programming [1]. Such programmed polymers can shift back to their original shape, when exposed to heat and pass a certain temperature called transition temperature (θ_{sw}) [1]. The temperature θ_{sw} is related to the thermal transition of switching domains and can be the glass (θ_g) or the melting temperature (θ_m) [2].

Such programming procedure consists of three steps: (I) heating and deforming above θ_{sw} , (II) cooling to $\theta < \theta_{sw}$ to solidify the switching domains, and (III) unloading at this temperature to obtain a programmed fixed shape [3].

The recovery of a SMP is performed by entropy acquirement of switching domains, when moving from an oriented (programmed) configuration to a random coil (recovered) chain conformation by heating to $\theta > \theta_{sw}$ [4].

Functional properties of SMPs are normally studied by cyclic thermomechanical tests [5, 6]. Characteristic functional properties for the quantification of the SME are the shape fixity ratio (R_f) and the shape recovery ratio (R_r). R_f describes the capability of a polymer to temporarily fix an applied deformation, whereas R_r expresses how well the original shape is recovered.

Several parameters can alter the functional properties of polymers. Among them are, for example, the maximum strains during programming or the holding time after deformation. It was observed that the functional properties

of thermally induced SMPs can also be significantly affected or even triggered by the uptake of solvents [7–10]. This can lead to chemical or physical aging [11–13]. Influencing the functional properties of SMPs through chemical aging is irreversible. In such processes, the chemical structure of the system is irreversibly changed, for example, in hydrolytically degraded polymers [13, 14]. In contrast, physical aging occurs when the molecular structure of the polymer does not change. Physical aging is reversible, so that the physically aged sample can be brought back to its initial state with some measures, for example, heating and drying [15].

The shape-memory capability of a system in vicinity to humidity or solvents can be strongly changed, before, during, and after programming [16, 17]. For instance, the worsening of shape recovery of a programmed polymer is an effect of physical aging because of humidity uptake which starts right after the first day of keeping them at a temperature lower than their glass transition temperature (θ_g) that may cause an incomplete, premature loss of the programmed shape [18]. This is the main reason why SMPs have a certain lifetime and have to be stored and maintained under particular conditions [19].

The observation that humidity can substantially influence the functional properties of SMPs has gained abundant attraction in recent years and is of great relevance for numerous medical applications [20, 21]. This has motivated the development of moisture-triggered SME [16–18]. The fundamental mechanisms of moisture triggering are either destabilization and elimination of hydrogen bonds [9], water-induced dissolution of crystalline domains [22], or degradation of switching domains responsible for shape fixation and recoiling of the chain segments during recovery [7].

Although accidental life-altering processes of polymers through physical or chemical aging are not prepossessing and desirable, *targeted aging* of materials before practical applications is required. Therefore, one important question is how functional properties of a SMP change, if it is “meaningfully” and “targeted” aged before programming (e.g., by introducing solvent molecules into the polymer matrix)? To our best knowledge, there is no systematic research to answer this question. Therefore, the aim of this study is to explore, whether targeted physical aging “prior to programming” can influence the functional properties of a commercially available polyether urethane (Estane, Lubrizol, Ovele Westerlo, Belgium). For this reason, dry and physically aged samples have been prepared. Physical aging was performed through the uptake of three different solvents: acetone (C_3H_6O), ethanol (C_2H_6O), and water (H_2O), and their sample-specific transport behavior was numerically studied. Moreover, the related changes in θ_g were discussed experimentally and numerically by molecular dynamics (MD) simulations.

It was observed that the incorporation of the above-mentioned solvents into the polymer matrices significantly changed the shape-memory capability of Estane. However, in the present contribution, only the results for hydrolytically (physically) aged samples will be discussed. This is because of the fact that the amount of diffused acetone and ethanol in

the polymer samples at the single steps of the shape-memory cycle could not be controlled, so that at the end of experiments unpredicted desorption effects have been observed and the data were not reproducible. For water-swollen samples, on the other hand, no significant mass change was detected.

Following the previous studies with Estane [23] and experimental water sorption investigations performed here, a maximum mass gain of 3 wt.% to 3.1 wt.% can be expected.

For the quantification of functional properties of Estane, cyclic thermomechanical tests consisting of two subsequent cycles with a uniaxial strain of $\varepsilon_m = 10\%$ was applied for dry and hydrolytically aged samples. Additionally, the same procedure was repeated with different holding times and with different maximum strains of $\varepsilon_m = 30\%, 60\%, 100\%$, and 150% for both dry and hydrolytically aged samples.

2. Materials and Methods

2.1. Materials. In the present contribution, aliphatic SM-polyurethane Estane (designation: ETE75DT3 NAT022) granulates (Lubrizol, Ovele Westerlo, Belgium) have been processed using an injection molding machine (Arburg Allrounder 270M 500-210, Lossburg, Germany). Processing steps and detailed sample preparation stages have been explained in [24, 25]. Molecular weight and weight distribution of Estane have been determined by Gel permeation chromatography, and results can be found in Supplement I. Fig. S1 shows size-exclusion gel permeation chromatography analysis of Estane. Here, an average molecular weight of 126 kg/mole was determined.

For solvent uptake and physical aging operations, three different solvents have been used: deionized water H_2O (HPLC grade, VWR Chemicals, Darmstadt, Germany), ethanol C_2H_6O (analytical reagent grade, absolute 99.8 + %, certificated for analysis, Fisher Scientific UK), and acetone C_3H_6O (analytical reagent grade, certificated for analysis, Fisher Scientific UK).

2.2. Numerical Investigations. Numerical investigations of Fickian diffusion have been studied with the commercial Finite Element software package COMSOL 5.0 Multiphysics.

Modeling the θ_g of dry and physically (hydrolytically) aged polymer samples has been performed through MD simulations with the MD software package LAMMPS, developed at Sandia National Laboratories [26]. Here, a generic model of a polymer with a finite extensible nonlinear elastic (FENE) potential has been employed, which allows to focus on generic rather than material-specific aspects. All simulations were performed in an *NPT* (number of molecules, pressure, and temperature constant) ensemble using Nose-Hoover thermostat and barostat to apply desired temperature and pressure. The equations of motions are integrated with the velocity Verlet algorithm.

The presented atomistic model is built up of 156 chains of 64-bead length, along with various numbers of small particles. The nonbonded interactions are modeled by the Lennard-Jones (LJ) potential $U_{\alpha\beta}^{LJ}$, and the connectivity of

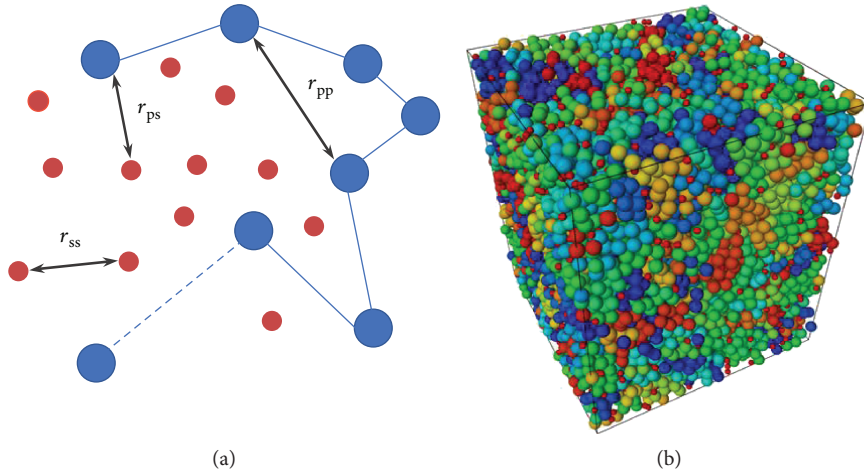


FIGURE 1: (a) A schematic view of the model used in the MD simulations. (b) A snapshot of the simulation box containing polymers and small molecules. Different chains are shown with different colors to improve visibility. Small molecules appear as small red spherical particles.

covalent bonds along the chains is ensured via the FENE potential U_{FENE} as follows:

$$U_{\text{FENE}} = -\frac{1}{2}KR_0^2 \left[\ln \left(1 - \left(\frac{r}{R_0} \right)^2 \right) \right],$$

$$U_{\alpha\beta}^{\text{LJ}} = 4\epsilon_{\alpha\beta} \left[\left(\frac{\sigma_{\alpha\beta}}{r_{\alpha\beta}} \right)^{12} - \left(\frac{\sigma_{\alpha\beta}}{r_{\alpha\beta}} \right)^6 \right], \quad (1)$$

where $\epsilon_{\alpha\beta}$, $\sigma_{\alpha\beta}$, $r_{\alpha\beta}$, $k = 30\epsilon_{\text{pp}}/\sigma_{\text{pp}}^2$, r , and $R_0 = 1.5\sigma_{\text{pp}}$ are the van der Waals (vdW) potential strength, the distance with zero potential energy, interatomic distance, strength factor of bonded potential, covalent bond length, and the breaking limit of the bonds, respectively. It should be noted that $\alpha, \beta \in \{\text{p}, \text{s}\}$ and p and s stand for polymer and small molecules (solvents), respectively. The quantity σ_{pp} is chosen to equal to 1, and the size of small particles is adjusted by setting $\sigma_{\text{ss}} = 0.5\sigma_{\text{pp}}$. The quantity σ_{ps} is obtained by the arithmetic mean of σ_{pp} and σ_{ss} .

Figure 1(a) shows a schematic view of the chain segment of the polymer in the vicinity of solvent molecules. As depicted in this picture, the distances between atoms of polymers and solvents are represented with r_{pp} , r_{sp} , and r_{ss} , where r_{pp} is the distance between atoms of polymers, r_{ps} between atoms of polymers and solvents, and r_{ss} between atoms of solvents, respectively. Moreover, in Figure 1(b), a snapshot of the simulation box is also shown. For the construction of initial polymer chains, the monomers are placed regularly on a 3D grid after which the system is melted at a relatively high temperature of $\theta = 2$ ($\theta_g = 0.44$ for the present model and all quantities in LJ units) to achieve statistically random distributions of chain conformations. It should be noted that for the sake of data interpretation, three independent packing models were built and simulations were performed for all three samples. The results shown here are an average out of three.

2.3. Experimental Sorption and Diffusion Studies. Prior to any experiment, the injection-molded plates of Estane with a thickness 2 mm have been kept in a vacuum desiccator to keep them dry. Afterwards, the plates were cut to round discs of diameter 44.5 mm with a mass of 3.777 ± 0.017 g. For sorption and diffusion experiments, these plates were positioned in reaction vessels containing 200 ml of water, ethanol, or acetone. The temperature of the reaction vessels has been controlled through a temperature-controlled water bath. Afterwards, each specimen was dried carefully dabbing the wet surfaces with a wad of lint-free cotton wool and then reimmersed into the reaction vessel. It should be noted that the measuring time was kept below 30 s to keep evaporation processes at a minimum. Moreover, weights were measured using an analytical balance of a type Sartorius A200S (Göttingen, Germany; resolution: 0.1 mg). The weight gain during sorption experiments is described as the solvent mole uptake by $m_p = 100$ g of polymer:

$$c_t = \frac{m_s}{(M_s) \times (m_p)} \times 100\%, \quad (2)$$

where m_s is the mass of sorbed solvent and M_s is its molar mass and m_p denotes the mass of the polymer.

2.4. Thermorheological Characterization. Using rectangular samples with dimensions of $W \times H \times L: 2 \times 10 \times 50$ mm³, dynamic mechanical thermal analysis (DMTA) experiments were accomplished in torsion mode with a stress-controlled rheometer with integrated Peltier-based temperature chamber (Anton Paar Physica MCR 301 plus CTD 180, Graz, Austria). During the torsion DMTA tests, a small uniaxial tensile force of around 0.5 N is superimposed to maintain the specimen under net tension. Thereupon, harmonic twist rotations with prescribed amplitude (0.01%) and constant frequency of 10 Hz were executed while the samples were heated in predefined temperature intervals at a constant heating rate of 0.25°C/min and the resulting harmonic

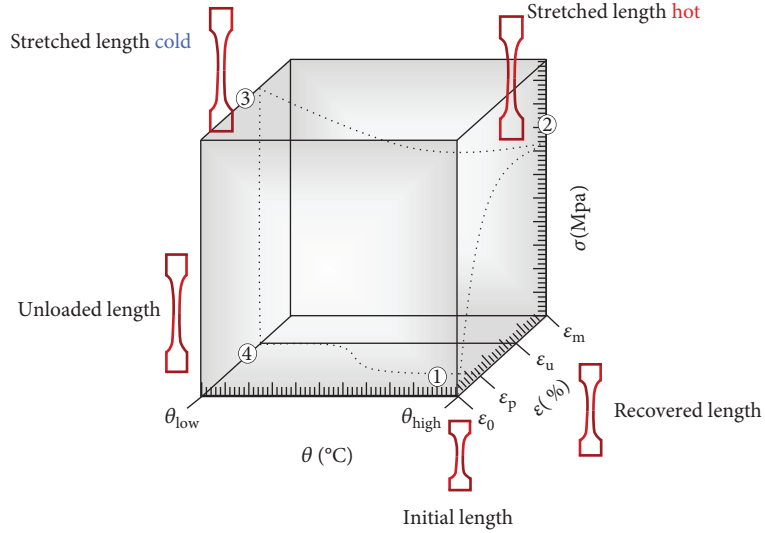


FIGURE 2: Schematic representation of a cyclic uniaxial thermomechanical tensile test in the σ - θ - ϵ diagram.

torque as well as the phase lag ϕ or loss factor $\tan \phi$ was measured. Such temperature sweep experiments provide important insights into the effective viscoelastic properties of the investigated material [27]. Here, the characteristic material properties like θ_g can be determined through the sample's response to the applied periodic loadings. Again here, the experiments have been repeated two more times and the results originate from an average out of all three runs.

2.5. Cyclic, Thermomechanical Tensile Tests. For tensile tests, Estane sheets were punched to dumbbell specimens of type 5A of DIN EN ISO 527-2 ($W \times H \times L: 2 \times 10 \times 75 \text{ mm}^3$). The gauge length of specimens is 25 mm. Cyclic, thermomechanical tensile tests were performed on a spindle-driven testing machine (Schenck Trebel RM50, Germany) with an adjusted strain and compression capacity of $\pm 500 \text{ N}$. The machine was equipped with a heating/cooling chamber (Fresenberger TK18.400.100, Wipperfürth, Germany). The temperature was PID-controlled (Eurotherm 3508, Limburg, Germany) so that temperatures in the range of -100 to 400°C could be adjusted and kept constant with a precision of $\pm 1^\circ\text{C}$. Each cycle consisted of a SM creation procedure (SMCP) under strain-controlled modes and recovery modes. In the programming part, the samples were heated up from room temperature to the upper working temperature of $\theta_{high} = 70^\circ\text{C}$ with a moderated heating rate of $3^\circ\text{C}/\text{min}$. Following that, temperature θ_{high} was fixed and, in a strain-controlled mode, the samples were deformed up to the maximum uniaxial strain of ϵ_m at a rate of $0.0051/\text{s}$. Subsequently, the deformed specimens were kept constant at θ_{high} for different holding times t_h . Under constant strain conditions, the specimens were then cooled down to a lower temperature of $\theta_{low} = 10^\circ\text{C}$ with a cooling rate of $3^\circ\text{C}/\text{min}$ and equilibrated for 40 min. Afterwards, the temporarily fixed strains ϵ_u were achieved along with the removal of stress. Under stress-free conditions, the recovery parts were induced by heat up of

the programmed samples to $\theta_{high} = 70^\circ\text{C}$ with the same heating rate as mentioned before and equilibrated for 40 min. Finally, the shape fixity and shape recovery ratios were measured for the quantification of the SME. Figure 2 demonstrates all steps of the thermomechanical tensile test cycle in a stress-temperature-stain (σ - θ - ϵ) diagram. These five steps of a cyclic uniaxial thermomechanical tensile test are based on strain-controlled programming and a stress-free recovery procedure. It should be noted that the thermomechanical tensile test was repeated once more ($N = 2$). However, only the results of the second cycle have been used for data interpretation, as the first cycle was utilized to erase the history of the system [28]. The results for the first cycle can be found in Supplement I. The following 2nd cycle could allow two different strain regimes with respect to the previous cycle ($N = 1$) in which the samples were stretched in a strain-controlled setting up to the maximum strain ϵ_m . In subsequent thermomechanical tensile tests ($N > 1$), the sample in a strain-controlled process can be stretched up to the previous maximum strain $\epsilon_{m2} = \epsilon_{m1} - \epsilon_{u2}$, which is called *strain length approach*. Comparatively, it can be stretched with additional previous maximum strains $\epsilon_{m2} = \epsilon_{m1}$. This approach is called *subsequent additional strain* [29]. In this contribution, samples have been stretched in the second cycle up to ϵ_{m2} according to strain length approach. These experiments have also been performed three times, and the results descend from the average out of them.

For the quantification of the SME of polymer samples, the shape fixity ratio $R_f(N)$ and shape recovery ratio $R_r(N)$ have been determined as important functional properties of the system. The shape fixity ratio $R_f(N)$ is the ratio of the strain in a stress-free state after removing the tensile stress in the N^{th} cycle $\epsilon_u(N)$ and the maximum strain $\epsilon_m(N)$. The shape recovery ratio $R_r(N)$ is on the other hand the ratio between the remaining strain after the N^{th} cycle to the remaining strain in the previous cycle and can be determined from strain values according to

$$R_f = \frac{\varepsilon_u(N)}{\varepsilon_m} \times 100\%, \quad (3)$$

$$R_r = \frac{\varepsilon_m - \varepsilon_p(N)}{\varepsilon_m - \varepsilon_p(N-1)} \times 100\%.$$

Here, $\varepsilon_p(N)$ is the recovered strain of the sample at the end of the recovery step.

2.6. Study of Diffusion Behavior. If the mode of diffusion is of Fickian type, then the diffusion rates of small molecules are faster than the relaxation process of polymer chains [30]. According to Fick's 1st law, moisture sorption occurs only by diffusion and the diffusion flux $\mathbf{j}(\mathbf{x}, t)$ is directly proportional to the gradient of its concentration:

$$\mathbf{j} = -D \operatorname{grad} c, \quad (4)$$

where $c(\mathbf{x}, t)$ is the sorbent concentration with units mol/m³ and D is the (isotropic) diffusion coefficient or diffusivity of a homogenous sample with units of m²/s. The process of diffusion into the sample has therefore the following form:

$$\operatorname{div} \mathbf{j} + \alpha \frac{\partial c}{\partial t} = 0, \quad (5)$$

$$\alpha \frac{\partial c}{\partial t} - D \operatorname{div} (\operatorname{grad} c) = 0. \quad (6)$$

To determine the changes of concentration of sorbents inside the sample at each point and time, (6) should be solved with respect to boundary conditions:

$$c = \bar{c}, \quad \forall \bar{c} \in \Gamma_D \times t, \quad (7)$$

$$\mathbf{j} \cdot \mathbf{n} = \bar{j}, \quad \forall \bar{j} \in \Gamma_N \times t,$$

at the Neumann boundary Γ_N and the Dirichlet boundary Γ_D and initial conditions in the sample's domain Ω at $t = t_0$:

$$c = c_0, \quad \forall c_0 \in \Omega \times t_0. \quad (8)$$

Multiplying diffusion Equation (6) with a test function (δ_c) and integrating by parts over the domain of the sample leads to the weak form:

$$\int_{\Omega} \alpha \partial_t(c) \delta c dV + \int_{\Omega} [D \operatorname{grad} c \cdot \operatorname{grad} \delta c] dV = \int_{\Gamma_N} \bar{j} \delta c. \quad (9)$$

Equation (9) is discretized with standard (Lagrangian) finite elements in the spatial domain. Applying an implicit backward Euler time stepping scheme, it could be solved numerically and the evolution of concentration $c(\mathbf{x}, t)$ can be analyzed for different sample geometries. Here, we investigate the mentioned samples of dimensions $W \times H \times L: 2 \times 10 \times 50$ mm³. The temporal concentration changes of the center of the mass of the sample have been recorded for three different probe molecules: acetone, ethanol, and water.

In addition to sorption, permeability is also important. The transport of small molecules inside polymers occurs through a solution-diffusion mechanism. This means that small molecules are first sorbed by the sample and then diffused inside it. The total amount of diffusion depends

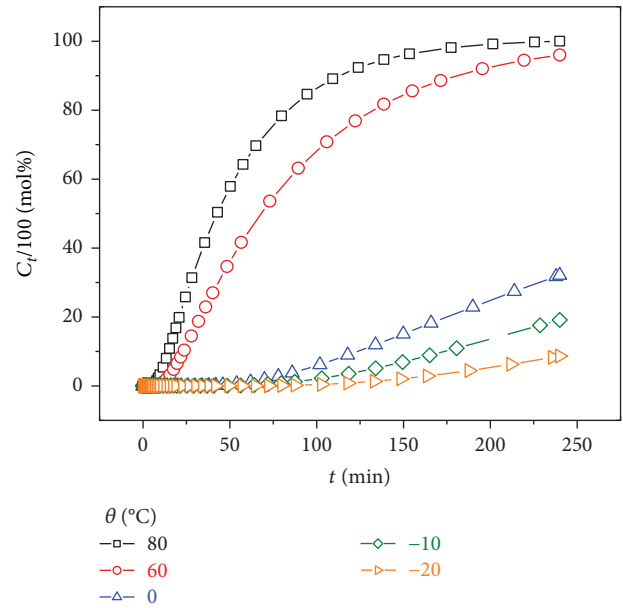


FIGURE 3: Simulation results for the temporal development of the changes in concentration of acetone in the middle of Estane samples with rectangular shapes ($W \times H \times L: 2 \times 10 \times 50$ mm³) at different temperatures.

upon the existing number of probe molecules between two successive layers. For this reason, isotropic permeability ζ is introduced as

$$\zeta = D S, \quad (10)$$

where S is the solubility parameter with the unit of pascal^{1/2}.

In addition to numerical solution of diffusivity, the diffusion coefficient D can be calculated by a 1-dimensional analytical solution after an appropriate mathematical computation. A well-known analytical solution of $c(x)$ for a 1-dimensional boundary value problem solution is developed by Crank [31], which is the most suitable for moderate and long-term experiments. More details about the numerical solution of Fick's law can be found in Supplement I Section S2.

3. Results and Discussions

3.1. Diffusion Behavior of Small Molecules into Estane Samples. The Fickian conduct of acetone, ethanol, and water inside Estane is studied at different temperatures experimentally and by the mean of finite element simulations. Since the qualitative behavior of the diffusion processes of the mentioned solvents into Estane is similar, only the results for acetone are shown here.

The simulation results for the temporal evolution of the concentration of acetone in the middle of the sample ($W \times H \times L: 2 \times 10 \times 50$ mm³) for different temperatures modeled are shown in Figure 3. As can be recognized from this picture, the amount of acetone molecules which are diffused inside the sample, increases with temperature and the concentration profile has a biphasic form. Below θ_g ,

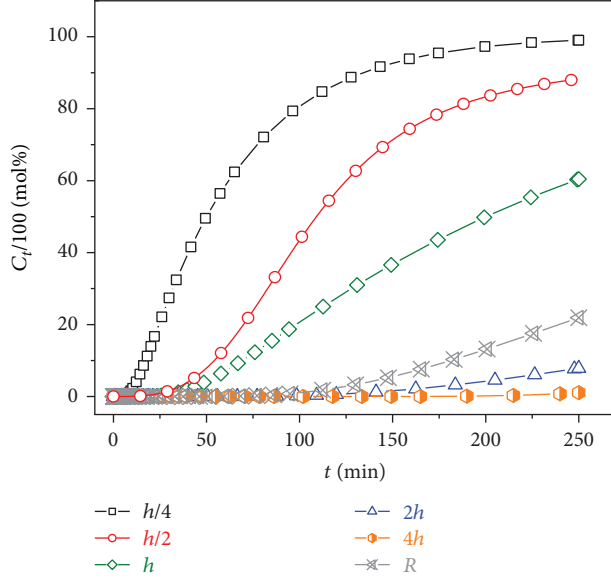


FIGURE 4: Simulation results of the influence of sample geometry on the amount of sorbed acetone at $\theta = 20^\circ\text{C}$. Rectangular samples have the dimension: $W \times H \times L: 2 \times x \times 50 \text{ mm}^3$, where x changes from $h/4$ to $4h$ and h is equal to 10 mm. Cylindrical sample is 2 mm thick and has a radius of $R = h$ mm.

the increase of acetone concentration is clearly lower than that of above θ_g and a maximum amount of about 30% could be achieved at $\theta = 0^\circ\text{C}$. Moreover, as reported in [30], isothermal short-time and long-time experiments lead to similar data, meaning that the diffusion of all three small molecules in Estane shows no significant concentration dependency. However, once the θ_g of the polymer is exceeded, the higher number of molecules is diffused as a result of activation volume according to Eyring's theory [32], so that after 175 minutes, the sample is totally saturated at $\theta_g = 80^\circ\text{C}$. With an increase in temperature, the tortuous route of small penetrants decreases and the system reaches its equilibrium.

Another interesting parameter influencing the saturation time of the sample is the geometry as depicted in Figure 4. Here, at $\theta = 20^\circ\text{C}$, the simulation results for temporal changes of acetone concentration in the middle of rectangular and round disk Estane samples have been illustrated for different dimensions. As anticipated, samples with smaller widths are saturated faster than others. Intriguingly, in contrast to the first example, cylindrical specimens with the radius: $R = h$, are saturated faster than the sample with $W = 2h$.

The results of the diffusion coefficients for the sorption of acetone, ethanol, and water into Estane at three different temperatures are summarized in Table 1, respectively. It can be concluded from this table that the diffusivity shows no systematic dependence on the size of probe molecule, as acetone is the biggest and water is the smallest molecule in this study (Figure 5). This is because of the fact that the molecular mobility does not depend on the probe size.

More important is the correlation between the boiling point of the molecules and their evaporation energies. Molecules with higher boiling points and evaporation energies

TABLE 1: Diffusion coefficient (D) for sorption of acetone, ethanol, and water into Estane samples at three different temperatures (θ).

Probe molecules	$\theta (\text{ }^\circ\text{C})$	$D \times 10^{-14} (\text{m}^2/\text{s})$
Acetone	0	4.217
Acetone	40	13.575
Acetone	80	30.535
Ethanol	0	0.007
Ethanol	40	0.464
Ethanol	80	1.861
Water	0	0.001
Water	40	0.041
Water	80	0.162

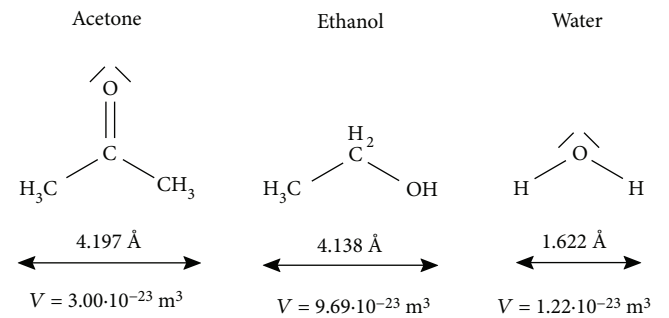


FIGURE 5: Structure formula and size of acetone, ethanol, and water, considering a spherical model [33]. The volume of the solvents and their radii are calculated from their densities at $\theta = 20^\circ\text{C}$ [34, 35].

have smaller diffusivities [35]. Sun and Chen [36] could achieve comparable results about the independence of the size of substituted probe molecules on the sorption and the diffusion processes into polyurethane/polymethyl methacrylate samples.

While the diffusivity of acetone at -10°C , that of ethanol at 19°C , and that of water at 91°C are equal, the amount of solvent uptake inside the Estane is different as shown in Figure 6. As previously mentioned, here, other parameters like solubility play important roles. Therefore, as can be concluded from the offset of Figure 6, at the beginning, acetone is diffused faster into Estane and then water and finally ethanol. However, after 150 min, ethanol diffuses clearly faster than others and a higher amount could be achieved.

As explained before, the dependency of the diffusion rate and the permeation upon temperature in sorption and desorption processes are evident [37]. To evaluate the activation energy of diffusion, its temperature dependency should be evaluated using the Arrhenius law.

$$D = D_0 \exp \left[-\frac{E_a}{R\theta} \right]. \quad (11)$$

Here, E_a is the activation energy, θ the absolute temperature, and R the universal gas constant equal to $8.314 \text{ J/mol}\cdot\text{K}$.

Figure 7 shows the plot of $\ln(D)$ versus θ for three studied solvents. As the graph implies, an almost linear dependency can be observed for Estane solvent samples during this temperature range. The values of activation energy for

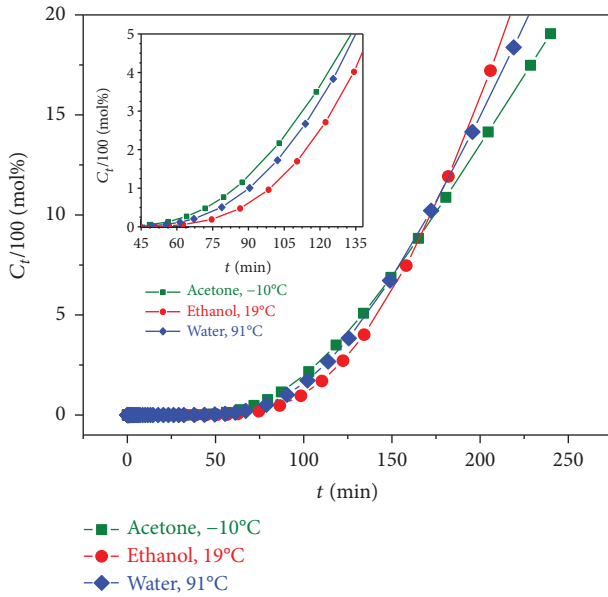


FIGURE 6: Simulation results of the temporal development of the concentration of acetone, ethanol, and water inside the rectangular sample ($W \times H \times L: 2 \times 10 \times 50 \text{ mm}^3$) at $\theta = -10, 19$, and 91°C , respectively.

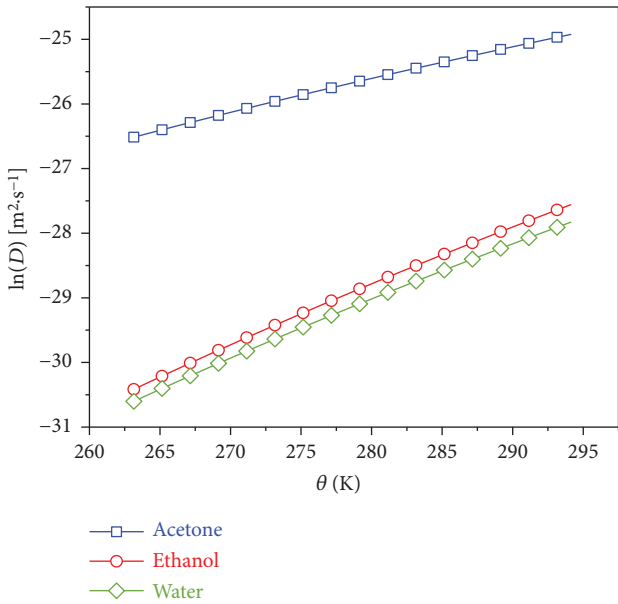


FIGURE 7: The temperature dependency of diffusion coefficients of three different solvents (acetone, ethanol, and water) inside Estane to demonstrate the dependence of $\ln(D)$ versus θ for the sorption process. The data are obtained from experimental weight gain measurements.

diffusion (E_0) can be simply calculated using regression analysis from plots depicted in Figure 7. The apparent activation energies of acetone, ethanol, and water read 32, 58.3, and 56.5 kJ/mol, respectively. These results are in good agreement with activation energies of the same small molecules in similar polyurethanes [30].

TABLE 2: Solubility parameter of Estane, acetone, ethanol, and water as a summation of square Hildebrand and Scott components δ_d , δ_p , and δ_h . Data from the handbook of Hansen solubility parameters [38].

Sample	Solubility parameter δ ((MPa) $^{-0.5}$)
Generic polyurethane	42
Acetone	33
Ethanol	44
Water	73

In addition to diffusivity, the cohesive energy density (CED) and Hildebrand's solubility parameter can be used to calculate the permeability of the sorbents in polymer samples [38]. Hildebrand's solubility parameter $\delta = \sqrt{\text{CED}}$ is a numerical estimation to indicate the strength of the molecular interaction between solvents and polymers. Materials with the same solubility parameter incline to dissolve in each other. The CED can be understood as the total amount of energy needed to completely remove a unit material volume from its neighbors to infinite separation. This value can be calculated in, for example, MD simulations as an increase in energy per mole material when all intermolecular forces have vanished [20]. The calculated solubility parameters of a representative polyurethane similar to Estane and three solvents are summarized in Table 2. In this contribution, the derivation of cohesive energy density is based on three solubility parameters which have been first introduced by Hildebrand and Scott [38]. Here, it is assumed that the square root of cohesive energy density is a summation of three contributions: dispersion interaction δ_d , representing the van der Waals type of nonpolar attractive interactions, the δ_p for interactions between permanent molecular dipoles, and the δ_h representing a hydrogen type of bonding (H-bonds), which in Hansen's approach not only addresses interactions related to H-bonds but also integrates other interactions.

It is clear that the solubility of polyurethane in water is weak and in acetone or ethanol clearly better, indicating that the affinity of polyurethane (Estane) is more toward ethanol or acetone. Moreover, the permeability and solubility parameters are in the same order.

Finally, the thermodynamic parameters for diffusion can be calculated using van't Hoff's relation [39]:

$$\log K_s = \left(\frac{\Delta S}{2.303R} \right) - \left(\frac{\Delta H}{2.303R\theta} \right). \quad (12)$$

Here, (ΔH) and (ΔS) are the values of change in enthalpy and entropy, respectively, and K_s is the equilibrium sorption constant, which can be estimated from the following equation:

$$K_s = \frac{n_s^{\text{eq}}}{m_p}, \quad (13)$$

where n_s^{eq} denotes the number of moles of the sorbed solvent at the equilibrium. The values of ΔH and ΔS are listed in Table 3. These values were calculated from the slope and intercept of the plot of $\ln(K)$ versus $(1/\theta)$. As can be noticed

TABLE 3: Thermodynamic parameters for sorption in Estane and studied solvents.

Thermodynamic parameters	Estane/ acetone	Estane/ ethanol	Estane/ water
ΔS (kJ/mol/K)	8.58×10^{-3}	4.84×10^{-3}	≈ 0
ΔH (kJ/mol)	0.06	0.026	≈ 0

for sorption, the values of ΔH are for all positive sorbents and in the range of 0.0267–0.06 kJ/mol. These positive values of ΔH are an indication for endothermic sorption dominated by the Fickian mode as a result of new pore creation inside the sample.

3.2. Determination of Functional Properties of Dry and Hydrolytically Aged Estane. Now that the diffusion of small molecules into polymer matrices has been studied, one can investigate the influence of such low molecular weight compounds on the shape-memory properties of the mentioned polyether urethane samples. As outlined before, in this part, we only concentrate on the effects of physical (hydrolytical) aging on the functional properties of Estane and the influence of other solvents will be discussed in a separate contribution.

In order to be able to investigate the influence of physical aging on the functional properties of Estane, the θ_g of both dry and physically (hydrolytically) aged samples should be first determined and compared.

For θ_g determination of dry Estane, temperature sweep tests of DMTA experiments were performed. The measured storage shear modulus (G') and loss shear modulus (G'') for dry Estane are depicted together with the results for physically (hydrolytically) aged samples in Figure 8. As can be observed from this picture, the storage modulus of dry samples starts gradually decreasing with temperature until the temperature reaches the θ_g of Estane (around 54°C), where because of morphological softening a rapid decrease in the stiffness can be recognized. The G'' on the other hand increases very slightly up to this temperature and sharply decreases from there on with increasing temperature.

On the other hand, the influence of hydrolytic aging on the θ_g of Estane is evident. Polymer chains of dry samples are relaxed and in entangled conformation. After physical (hydrolytical) aging, which takes place through diffusion of water molecules, the relaxed polymeric chains are pulled apart from each other and chains experience an internal stress (residual stress) that is counteracted by the tendency of polymer chains to return back to their relaxed minimum energy state.

The amount of water uptake for Estane was characterized by mass gain experiments and was found to be around 3 wt.% to 3.1 wt.% at room temperature after one week being settled in a water bath. As can be observed from Figure 8, the mechanical properties of physically (hydrolytically) aged samples are different from that of dry ones. This polymer softening (plasticization) effect [40] can be understood as a consequence of a water-induced swelling effect [41] which

results in an increase of free volume between polymer chain segments and therefore, in an increase of chain mobility, was approved also by atomistic simulation studies [20, 21]. Moreover, the presented evolution of the loss factor depicted on the right-hand side of Figure 8 reveals that the incorporation of water and consequentially the plasticization effect result in a shift of θ_g to lower values. From this result, such a shift towards lower θ values with $\theta_g^{\text{wet}} = 48^\circ\text{C}$ becomes obvious. This result could be approved qualitatively by atomistic simulation studies as shown in Figure 9.

It can be observed that the θ_g decreases with the number density of small particles, diffused into a polymer melt. This trend is in accordance with experimental results shown in Figure 8, where the size of small molecules is smaller than the Kuhn length of the studied polymer. In this figure, $\theta_{g,0}$ stands for θ_g of pure polymers with the same chain length and in the same pressure. The Kuhn length is a theoretical concept, which relates the number of conceptual segments in a real polymer chain to the number of segments in an equivalent freely jointed chain model. Since our model chain is chosen to be freely jointed already from the setup, one finds that the Kuhn length is of the order of one bead size (σ_{pp}). Therefore, when the size of small particles is smaller than the Kuhn length for polymers, it is observed that increasing the concentration of small particles leads to the reduction of θ_g in both MD simulations and experimental works.

We are aware of the fact that real samples do always contain a distribution of chain lengths and that this may be important for the observed properties. However, in order to gain a first qualitative understanding and for the sake of simplicity, we first focused on a monodisperse system. As mentioned above, despite this simplicity, the model predicts a decrease of θ_g upon adding small molecules which is qualitatively in line with experimental results on storage and loss moduli shown in Figure 8, where the temperature corresponding to the maximum of the loss factor is shifted to lower temperatures by adding small molecules (physically (hydrolytically) aged sample). As the next step, it would be indeed very interesting to account for the effect of polydispersity. In view of the computational challenge, we would like to postpone this task to a future work.

3.3. Shape-Memory Properties

3.3.1. Shape-Memory Response, Influence of Holding Time. The influence of holding time following the maximum strain of $\varepsilon_m = 30\%$ on the SM performance of dry and physically (hydrolytically) aged samples was investigated. Here, dry and physically (hydrolytically) aged specimens have been programmed according to the description mentioned in Section 2.5, which will be explained briefly here. Estane polymer samples were stretched uniaxially at $\theta_{\text{high}} = 70^\circ\text{C}$ during programming from the initially nonstretched extension $\varepsilon_0 = 0\%$ to the maximum strain of $\varepsilon_m = 30\%$ and held at this temperature for different holding times in the range of 6–6000 s. Afterwards, the stretched samples were cooled down from θ_{high} to $\theta_{\text{low}} = 10^\circ\text{C}$, while the stress was kept constant

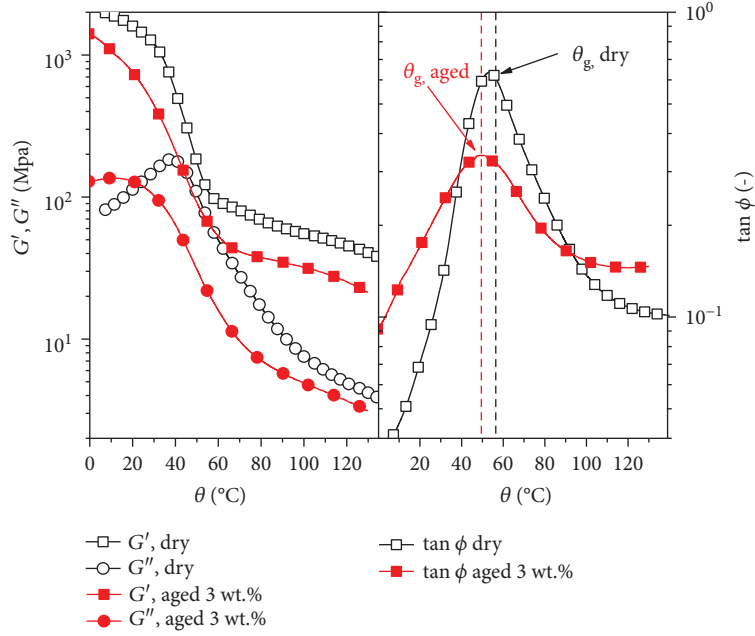


FIGURE 8: Comparison of the thermomechanical properties of dry (open symbols) and physically (hydrolytically) aged (solid symbols) Estane obtained from DMTA experiments. Left: changes of storage- (G') and loss modulus (G'') for dry (open symbols) and physically (hydrolytically) aged samples (solid symbols) in temperature sweep tests. Right: comparison of loss factor $\tan (\phi)$ of dry (open symbols) and (hydrolytically) aged samples (solid symbols) [24].

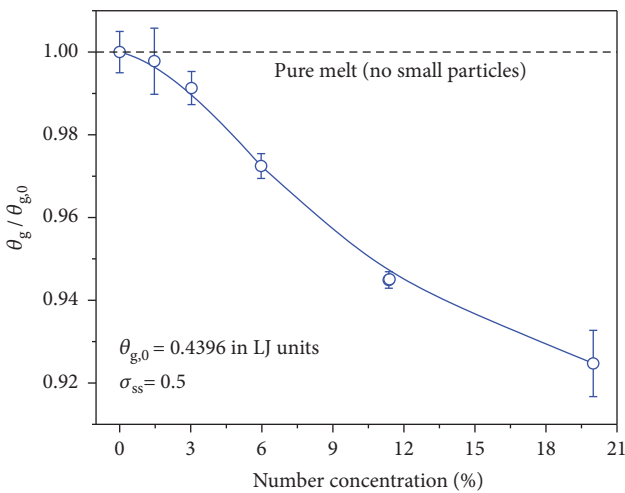


FIGURE 9: Results of MD simulations on θ_g versus the concentration of small molecules, which diffuse into a polymer melt. The polymer melt is modelled here as a coarse-grained linear chain. The small molecules are spherical Lennard-Jones (LJ) particles. Despite the generic feature of the model, the qualitative trend observed here is in agreement with experiments [41]. Results from calculations performed on three independent packing models.

to solidify the oriented polymer chains. After cooling, the samples have been unloaded by releasing the stress and keeping them at θ_{low} , which resulted in temporary fixed strain ε_u . In the last step, under a stress-free condition, the samples have been brought to θ_{high} , where the final recovered strains ε_p are achieved.

In Section S3 of Supplement I, Fig. S2 demonstrates the whole SM cycle in two subsequent runs in the stress-temperature-strain (σ - θ - ε) diagram for dry Estane stretched up to $\varepsilon_m = 30\%$.

The evolution of normalized strain with time in recovery modulus for both samples together with the measured shape fixities as a function of time for different holding times $t_h = 6, 60, 600$, and 6000 s is depicted in Figure 10. Complementarily, the calculated shape fixities and shape recoveries for the second cycle are listed in Table 4. For comparison reasons, the results for the first cycle are summarized in Table S1 of Section S3 in Supplementary I. A thorough concerned description of results is also included.

As can be observed from Figures 10(a) and 10(b), the reduced strains ($\varepsilon/\varepsilon_0$) for both dry and physically (hydrolytically) aged samples during the recovery processes in the second thermomechanical cycle decrease with a sigmoidal function until it reaches the θ_g of Estane. For dry samples, the rate of normalized strain began to slow down after 1500 s. By relaxation times larger than 1500 s, a steady normalized strain magnitude (equilibration) has been achieved. Figures 10(a) and 10(b) show that the increase in holding time has two effects on the functional properties of dry and physically (hydrolytically) aged specimens: it resulted in (1) a slower shape recovery rate and (2) a lower shape recovery ratio. Interestingly, obvious higher recovery ratios were obtained for physically (hydrolytically) aged samples. A possible reason for better functional properties of physically (hydrolytically) aged specimen could be presumed in the creation of additional physical crosslinks and different stabilizations of the polymer matrices through H-bond networks, which are created through absorbed water molecules. This

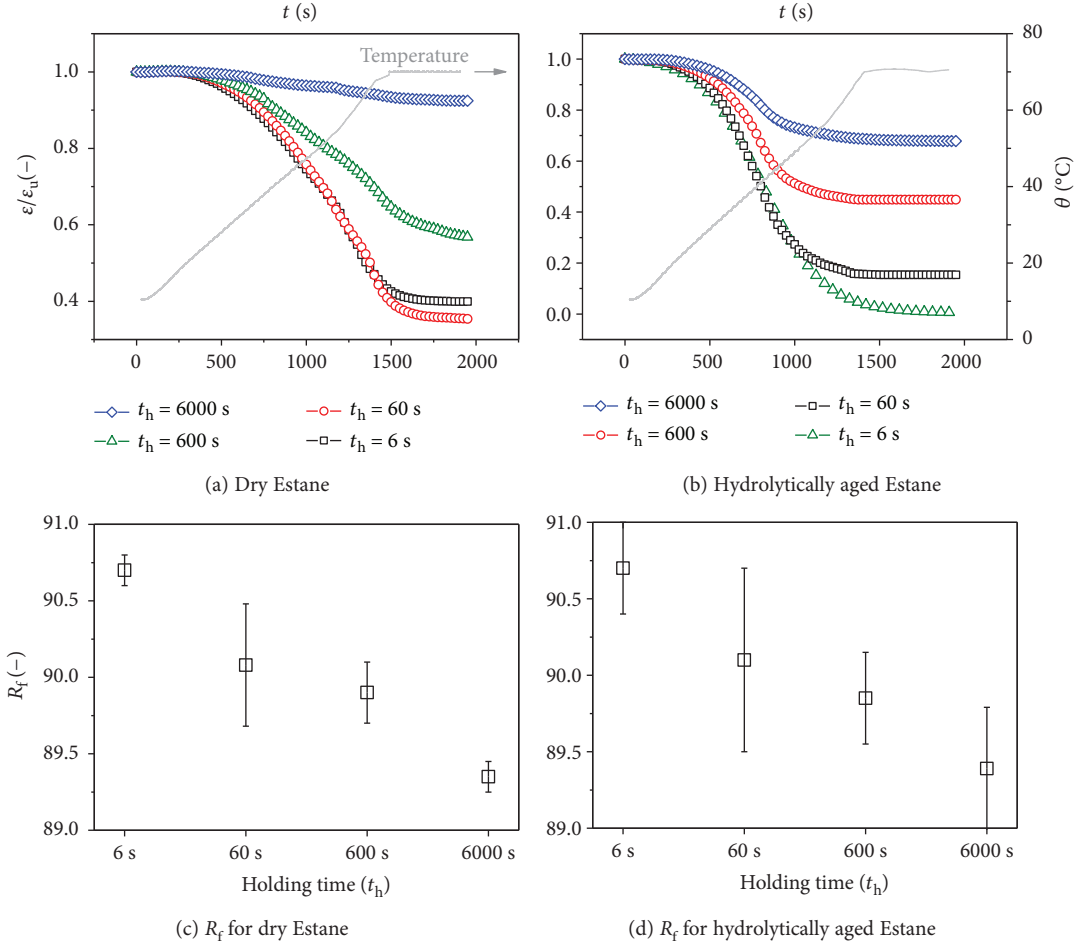


FIGURE 10: Development of reduced strains of (a) dry- and (b) physically (hydrolytically) aged Estane samples with 3 wt.% water during the recovery process in the 2nd cycle with different holding times (from 6 to 6000 s) after stretching up to $\varepsilon_m = 30\%$ at $\theta_{high} = 70^\circ\text{C}$ in a cyclic thermomechanical tensile test. Achieved shape fixity ratio of (c) dry- and (d) physically (hydrolytically) aged Estane samples with 3 wt.% water after two successive cycles. Results are the average of three similar test runs. The corresponding θ values are plotted as gray lines with respect to the right ordinate.

TABLE 4: Shape-memory properties of dry and physically (hydrolytically) aged Estane programmed at $\theta = 70^\circ\text{C}$. The results for the first cycle can be found in the Supplement I.

Holding time (s)	R_f (2) (%)	R_f (2) (%)
Dry samples		
6	90.71 ± 5.26	65.00 ± 7.01
60	90.11 ± 5.00	60.20 ± 4.14
600	89.84 ± 4.06	43.71 ± 4.23
6000	89.36 ± 4.75	8.00 ± 3.37
Physically (hydrolytically) aged samples		
6	91.99 ± 5.79	99.01 ± 5.23
60	92.15 ± 5.97	85.01 ± 3.67
600	90.08 ± 6.78	55.12 ± 4.46
6000	90.16 ± 9.63	33.86 ± 6.12

shows that even after heating processes during two cycles, the remaining water molecules participate in the recovery procedure and cause an improved shape recovery. The

simulation results on SM properties of wet polyesters approve our results [42].

At elevated temperatures after deformation, if higher holding time is applied to the material, more time is given to the configurational changes to take place. This means that the material exhibits more resistance against locking in the strain and reasonably lower shape recovery. It was realized that there are chain regions in the molecular network of polymers which are normally inactive in quasistatic deformations but become stretched during fast deformations. The aforementioned regions have loose connectivity to the main load-bearing network and can reach a lower energy state when enough time is given. The relaxation process in polymers involves rapid readjustments of the kinks in local scales and slow rearrangement of the convolutions in long-range scales [43]. One presumption for this observation would be the chain alignment in the polymer matrices with time and consequently the increase in crystalline portions, which needs additional investigations through, for example, wide-angle X-ray scattering (WAXS) experiments [6]. Nevertheless, the number of crystalline portions of unstretched

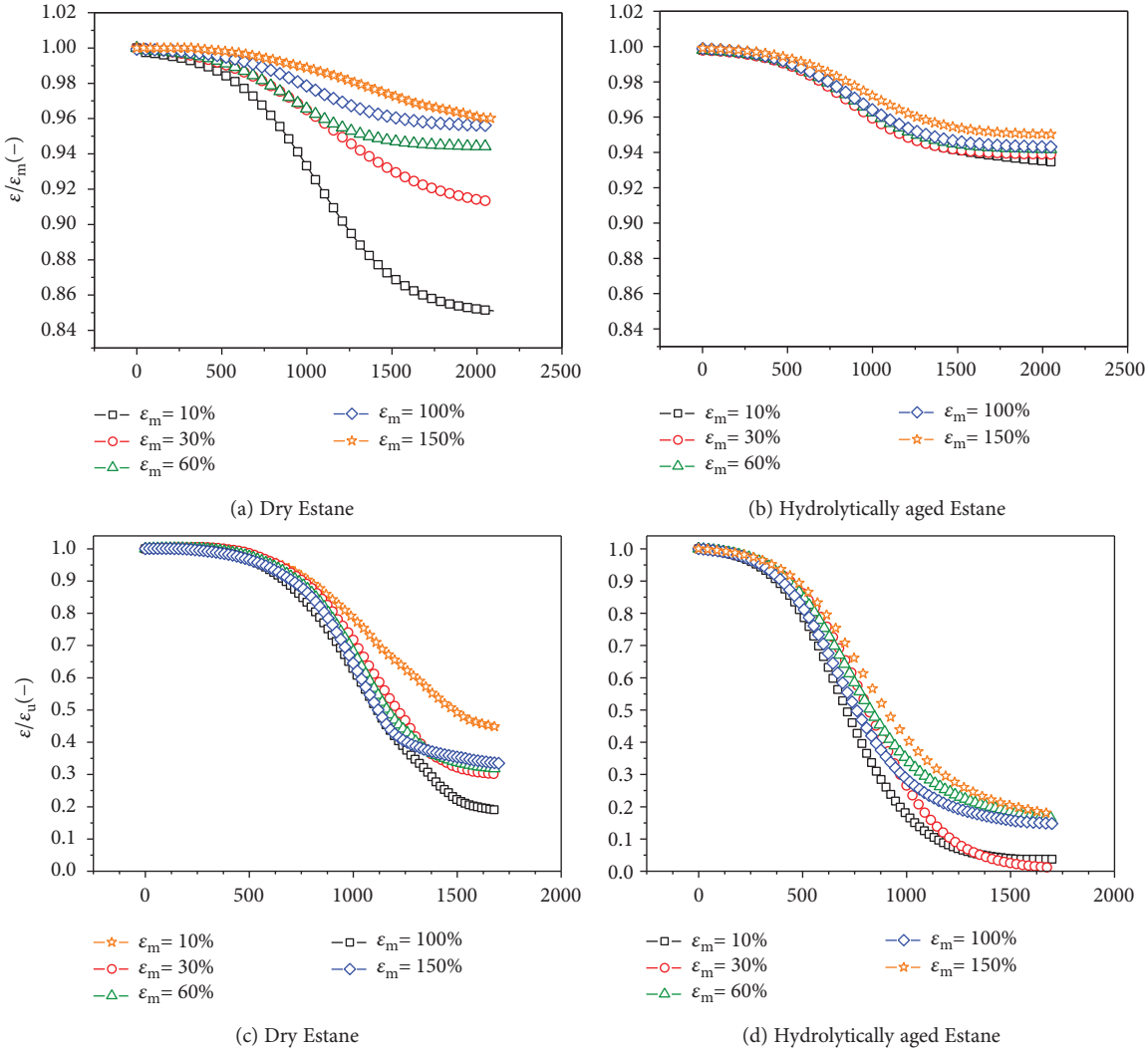


FIGURE 11: Development of reduced strain values ($\varepsilon/\varepsilon_m$) for (a) dry- and (b) physically (hydrolytically) aged Estane samples during the unloading process in the 2nd cycle stretched up to different maximum strains ε_m (from 10% to 150%) at $\theta_{low} = 10^\circ\text{C}$ in a cyclic thermomechanical tensile test. Development of reduced extension values ($\varepsilon/\varepsilon_u$) for (c) dry- and (d) physically (hydrolytically) aged Estane samples during the recovery process in the 2nd cycle stretched up to different maximum strains ε_m (from 10% to 150%) at $\theta_{high} = 70^\circ\text{C}$ in a cyclic thermomechanical tensile test.

samples could be analyzed by differential scanning calorimetry (DSC) measurements. Such an experiment has been performed for dry Estane, and the results for two successive runs are depicted in Fig. S3 of Section S4 of Supplementary I.

The final achieved shape fixity ratios for both dry and physically (hydrolytically) aged samples are depicted in Figures 10(c) and 10(d). It can be noticed that the shape fixity ratio of water swollen samples do not contradict with the R_f of the dry specimen between experimental errors. It is believed that at θ_{low} the mobility of chains and water molecules is so limited that no different shape fixation can be observed correspondingly. Moreover, it can be perceived that all samples showed good shape fixation in the range of 89–91%, cf Table 4. Moreover, in the range of experimental errors, shape fixation does not change too much with increasing holding times for both dry and physically (hydrolytically) aged samples. In the literature, one finds different outcomes.

While in [44], it was demonstrated that an increase in holding time would improve the shape fixation; exactly the opposite case was reported in [45]. Therefore, it can be concluded that the holding time in stress-controlled experiments may affect the SM properties of the samples totally different [46].

3.3.2. Shape-Memory Response, Influence of Maximum Applied Strain. Another parameter influencing the functional properties and thermomechanical performance of SMPs is the final maximum strains during programming. Therefore, in the next step, dry and physically (hydrolytically) aged samples have been stretched during programming up to different final strains ε_m in the range of 10% to 150%. It is noteworthy to mention that the holding time was $t_h = 6$ s for all cycles.

Figure 11 shows the development of relative strain values of dry and physically (hydrolytically) aged polymer samples during unloading and recovery steps. The calculated shape

TABLE 5: Shape-memory properties of dry and physically (hydrolytically) aged Estane programmed at $\theta = 70^\circ\text{C}$. The results for the first cycle can be found in Supplement I.

Maximum strain ϵ_m (-)	R_f (2) (%)	R_r (2) (%)
Dry samples		
10%	85.07 ± 3.44	81.02 ± 6.21
30%	91.46 ± 5.75	71.11 ± 6.94
60%	94.47 ± 5.39	69.98 ± 7.34
100%	95.60 ± 6.18	67.18 ± 8.56
150%	95.84 ± 4.28	56.14 ± 6.33
Physically aged samples		
10%	93.41 ± 4.25	99.03 ± 3.67
30%	91.99 ± 5.79	95.24 ± 5.23
60%	93.90 ± 5.43	88.20 ± 4.97
100%	94.65 ± 7.63	87.52 ± 6.12
150%	95.60 ± 6.18	84.33 ± 6.18

fixities and shape recoveries of the samples for the second cycle are summarized in Table 5. Again, corresponding supportive results for the first runs can be found in Table S2 of Section S3 of Supplementary I.

As can be observed from Figures 11(a) and 11(b), the different applied maximum strains influenced the shape fixity process of both dry and physically (hydrolytically) aged samples at $\theta_{low} = 10^\circ\text{C}$. This shows that at θ_{low} polymer samples exhibited elastic response to the applied stretching, but the least part of elongation recovers right after unloading. Although reorientation of polymer chains at this temperature is hard, by increasing final elongations, the amount of unrecoverable strains seems to raise with ϵ_m .

The relative strain values ϵ/ϵ_m presented in Figures 11(a) and 11(b) can be understood as the development of the apparent shape fixity ratio $R_{f,app}$ during unloading at $\theta_{low} = 10^\circ\text{C}$. After a time period of approx. 30 min, the decay in ϵ/ϵ_m is almost completed for dry samples and a plateau value in the range of $R_{f,app} = 85\%-96\%$ was reached. In comparison, the shape fixation of physically (hydrolytically) aged samples approaches the plateau domain in less time. For physically (hydrolytically) aged Estane, the apparent shape fixity ratio is distinctly higher and in the range of $R_{f,app} = 93\%-96\%$. As depicted in Figures 11(a) and 11(b), a rise in ϵ_m resulted in an increase of $R_{f,app}$ from 85% for $\epsilon_m = 10\%$ to 96% for $\epsilon_m = 150\%$ for dry samples and an increase from 93% for $\epsilon_m = 10\%$ to 96% for $\epsilon_m = 150\%$ for physically (hydrolytically) aged samples.

The development of averaged strain values in relative units ϵ/ϵ_u for both dry and physically (hydrolytically) aged specimens is illustrated in Figures 11(c) and 11(d). Both dry and physically (hydrolytically) aged Estane showed qualitatively similar recovery behavior, whereby a plateau value could be attained for times larger than $t > 30$ min. For the recovery step, the normalized representation of ϵ/ϵ_u as a function of time shows an obvious dependency on the maximum strains (cf Table 5). It can be revealed that with increasing maximum strains ϵ_m , the shape recoverability

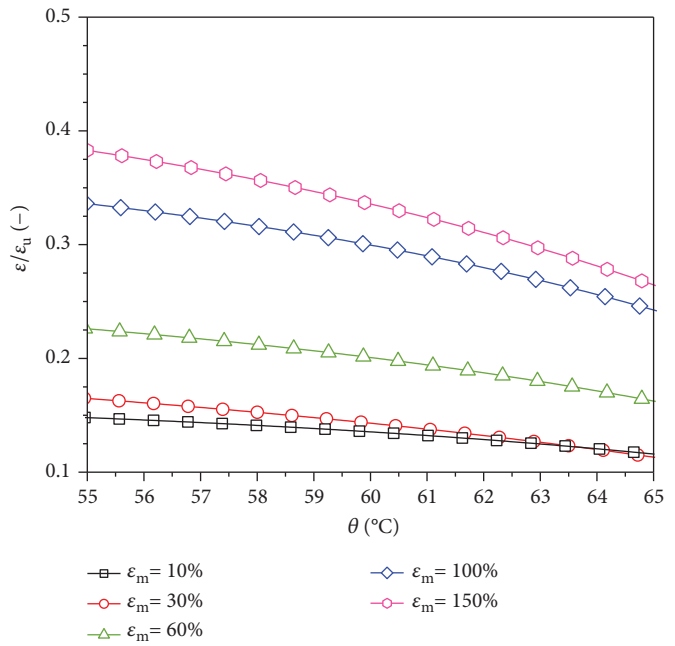


FIGURE 12: Development of reduced ϵ values for dry Estane during the recovery process in the 2nd cycle stretched up to different maximum strains ϵ_m (from 10% to 150%) at $\theta_{high} = 70^\circ\text{C}$ in a cyclic thermomechanical tensile test.

R_r of both samples decreased from 81% to 56% for dry and from 99% to 84% in the case of physically (hydrolytically) aged samples.

It can be observed that the shape recovery effect decreases because of an increase in the amount of nonrecoverable (plastic) parts of the shape changes with an increase in ϵ_m . This could be a consequence of oriented crystalline structures [47–49]. The observed decrease in recovery effects with an increasing final maximum strain has also been reported for other SMPs [50, 51].

Maximum final elongations do not only affect the shape recovery values but also influence the shape recovery rate of the samples. In Figure 12, the development of reduced strain values ϵ/ϵ_u for dry Estane in the recovery step is depicted as a function of temperature in the range of 55–65°C. As can be indicated from Figure 12, the lower the strains ϵ are, the faster is the recovery around θ_g . This finding might be interesting for applications, where faster recovery is demanded.

4. Conclusion

In the present contribution, we first studied the transport behavior of three substituted compounds (acetone, ethanol, and water) through Estane experimentally and with numerical simulations. It was revealed that even after 1 week, putting the samples in the corresponding solvent bathes, neither enthalpy relaxation nor monomer release, could occur because of the lack of hydrophilic groups. Moreover, it was demonstrated that the θ_g lowering of physically aged samples was due to the plasticization effects and a consequence of higher capability of low molecular weight compounds and

oriented polymer chains for molecular movements in a low energetic state. The increase in the interaction of water molecules with polar chain groups leads to disrupting the weak molecular interactions of adjacent polymer chains. This could be approved by atomistic simulation studies that indicated a θ_g -lowering of freely jointed polymer systems up to 7% for 12% number concentrations of spherical Lennard-Jones (LJ) particles.

Moreover, the influence of physical (hydrolytical) aging, through the incorporation of 3 wt.% water molecules into dry polymer matrices on the functional properties of the Estane, was studied. Dry and physically (hydrolytically) aged samples have been conducted to different maximum strains and different holding times. It could be indicated that the shape fixation of physically (hydrolytically) aged polymers do not differ from dry samples in the range of statistical errors. However, physical (hydrolytic) aging resulted in an obvious better and faster shape recovery ratio as a result of additional physical crosslinks.

We assume that the presented findings might motivate further knowledge-based researches for designing polymer systems with defined SM parameters.

Disclosure

The founding sponsors had no role in the design of the study; in the collection, analysis, or interpretation of data; in the writing of the manuscript; and in the decision to publish the results.

Conflicts of Interest

The authors declare no conflict of interest.

Acknowledgments

The authors are grateful to German Research Foundation for the financial support with the DFG Priority Program SPP 1713 "Chemomechanics" (Grant Project Number STE 969/8-1/8-2). The authors thank Sabine Ludwigs and Carsten Dingler (Institute of Polymer Chemistry, University of Stuttgart) for GPC experiment.

Supplementary Materials

As mentioned in the manuscript, some supporting information can be found in Supplement I. There, one can find the results of GPC experiments (Section S1). In addition to Section 2.6 and for the better understanding of the results, an analytical solution of diffusion for a 1-dimensional boundary value problem is discussed in Section S2 of Supplementary I. Moreover, in addition to Tables 3 and 4, first, a two-successive thermomechanical cycle for dry Estane stretched up to $\epsilon_m = 30\%$ is illustrated and briefly discussed demonstratively. Thereafter, the results of the first runs for the samples stretched up to different maximum strains and with different holding times are also summarized in Tables S1 and S2 of Supplementary I. At the end of Supplementary I Section S4, two runs of DSC are depicted and argued for dry Estane. (*Supplementary Materials*)

References

- [1] M. Behl, M. Y. Razzaq, and A. Lendlein, "Multifunctional shape-memory polymers," *Advanced Materials*, vol. 22, no. 31, pp. 3388–3410, 2010.
- [2] M. Behl, K. Kratz, J. Zottmann, U. Nöchel, and A. Lendlein, "Reversible bidirectional shape-memory polymers," *Advanced Materials*, vol. 25, no. 32, pp. 4466–4469, 2013.
- [3] J. Hu, Y. Zhu, H. Huang, and J. Lu, "Recent advances in shape-memory polymers: structure, mechanism, functionality, modeling and applications," *Progress in Polymer Science*, vol. 37, no. 12, pp. 1720–1763, 2012.
- [4] H. Meng and G. Li, "A review of stimuli-responsive shape memory polymer composites," *Polymer*, vol. 54, no. 9, pp. 2199–2221, 2013.
- [5] M. Heuchel, T. Sauter, K. Kratz, and A. Lendlein, "Thermally induced shape-memory effects in polymers: quantification and related modeling approaches," *Journal of Polymer Science Part B: Polymer Physics*, vol. 51, no. 8, pp. 621–637, 2013.
- [6] T. Sauter, M. Heuchel, K. Kratz, and A. Lendlein, "Quantifying the shape-memory effect of polymers by cyclic thermomechanical tests," *Polymer Reviews*, vol. 53, no. 1, pp. 6–40, 2013.
- [7] T. D. Nguyen, C. M. Yakacki, P. D. Brahmbhatt, and M. L. Chambers, "Modeling the relaxation mechanisms of amorphous shape memory polymers," *Advanced Materials*, vol. 22, no. 31, pp. 3411–3423, 2010.
- [8] J. Choi, A. M. Ortega, R. Xiao, C. M. Yakacki, and T. D. Nguyen, "Effect of physical aging on the shape-memory behavior of amorphous networks," *Polymer*, vol. 53, no. 12, pp. 2453–2464, 2012.
- [9] T. Xie, K. A. Page, and S. A. Eastman, "Strain-based temperature memory effect for Nafion and its molecular origins," *Advanced Functional Materials*, vol. 21, no. 11, pp. 2057–2066, 2011.
- [10] X. Gu and P. T. Mather, "Water-triggered shape memory of multiblock thermoplastic polyurethanes (TPUs)," *RSC Advances*, vol. 3, no. 36, pp. 15783–15791, 2013.
- [11] B. Yang, W. M. Huang, C. Li, C. M. Lee, and L. Li, "On the effects of moisture in a polyurethane shape memory polymer," *Smart Materials and Structures*, vol. 13, no. 1, pp. 191–195, 2004.
- [12] R. Xiao and T. D. Nguyen, "Modeling the solvent-induced shape-memory behavior of glassy polymers," *Soft Matter*, vol. 9, no. 39, pp. 9455–9464, 2013.
- [13] T. Pretsch, I. Jakob, and W. Müller, "Hydrolytic degradation and functional stability of a segmented shape memory poly(ester urethane)," *Polymer Degradation and Stability*, vol. 94, no. 1, pp. 61–73, 2009.
- [14] T. Pretsch, "Durability of a polymer with triple-shape properties," *Polymer Degradation and Stability*, vol. 95, no. 12, pp. 2515–2524, 2010.
- [15] T. Xu and G. Li, "Durability of shape memory polymer based syntactic foam under accelerated hydrolytic ageing," *Materials Science and Engineering: A*, vol. 528, no. 24, pp. 7444–7450, 2011.
- [16] B. F. Pierce, K. Bellin, M. Behl, and A. Lendlein, "Demonstrating the influence of water on shape-memory polymer networks based on poly[(rac-lactide)-co-glycolide] segments *in vitro*," *The International Journal of Artificial Organs*, vol. 34, no. 2, pp. 172–179, 2011.

- [17] W. M. Huang, B. Yang, L. An, C. Li, and Y. S. Chan, "Water-driven programmable polyurethane shape memory polymer: demonstration and mechanism," *Applied Physics Letters*, vol. 86, no. 11, article 114105, 2005.
- [18] G. Huang and H. Sun, "Effect of water absorption on the mechanical properties of glass/polyester composites," *Materials & Design*, vol. 28, no. 5, pp. 1647–1650, 2007.
- [19] Y. Chae Jung, H. Hwa So, and J. Whan Cho, "Water-responsive shape memory polyurethane block copolymer modified with polyhedral oligomeric silsesquioxane," *Journal of Macromolecular Science, Part B*, vol. 45, no. 4, pp. 453–461, 2006.
- [20] E. Ghobadi, M. Heuchel, K. Kratz, and A. Lendlein, "Simulation of volumetric swelling of degradable poly[(rac-lactide)-co-glycolide] based polyesterurethanes containing different urethane-linkers," *Journal of Applied Biomaterials & Functional Materials*, vol. 10, no. 3, pp. 293–301, 2012.
- [21] E. Ghobadi, M. Heuchel, K. Kratz, and A. Lendlein, "Atomistic simulation of the shape-memory effect in dry and water swollen poly[(rac-lactide)-co-glycolide] and copolyester urethanes thereof," *Macromolecular Chemistry and Physics*, vol. 215, no. 1, pp. 65–75, 2014.
- [22] H. Lu, Y. Liu, J. Leng, and S. Du, "Qualitative separation of the physical swelling effect on the recovery behavior of shape memory polymer," *European Polymer Journal*, vol. 46, no. 9, pp. 1908–1914, 2010.
- [23] E. Ghobadi, R. Sivaneshapillai, J. Musialak, and H. Steeb, "Modeling based characterization of thermorheological properties of polyurethane ESTANE™," *International Journal of Polymer Science*, vol. 2016, Article ID 7514974, 11 pages, 2016.
- [24] E. Ghobadi, M. Elsayed, R. Krause-Rehberg, and H. Steeb, "Demonstrating the influence of physical aging on the functional properties of shape-memory polymers," *Polymers*, vol. 10, no. 2, pp. 107–131, 2017.
- [25] C. Schmidt, A. M. S. Chowdhury, K. Neuking, and G. Eggeler, "Studies on the cycling, processing and programming of an industrially applicable shape memory polymer Tecoflex® (or TFX EG 72D)," *High Performance Polymers*, vol. 23, no. 4, pp. 300–307, 2011.
- [26] S. Plimpton and B. Hendrickson, "A new parallel method for molecular dynamics simulation of macromolecular systems," *Journal of Computational Chemistry*, vol. 17, no. 3, pp. 326–337, 1996.
- [27] E. Ghobadi, R. Sivaneshapillai, J. Musialak, and H. Steeb, "Thermo-rheological characterization of polyetherurethane: Parameter optimization and validation," *Constitutive Models for Rubbers IX*, vol. 1, pp. 157–163, 2015.
- [28] E. Ghobadi, M. Heuchel, K. Kratz, and A. Lendlein, "Influence of different heating regimes on the shape-recovery behavior of poly(L-lactide) in simulated thermomechanical tests," *Journal of Applied Biomaterials & Functional Materials*, vol. 10, no. 3, pp. 259–264, 2012.
- [29] E. Ghobadi, M. Heuchel, K. Kratz, and A. Lendlein, "Simulating the shape-memory behavior of amorphous switching domains of poly(l-lactide) by molecular dynamics," *Macromolecular Chemistry and Physics*, vol. 214, no. 11, pp. 1273–1283, 2013.
- [30] A. Marquardt, S. Mogharebi, K. Neuking, F. Varnik, and G. Eggeler, "Diffusion of small molecules in a shape memory polymer," *Journal of Materials Science*, vol. 51, no. 21, pp. 9792–9804, 2016.
- [31] J. Crank, *The Mathematics of Diffusion*, Science Publications, Oxford, UK, 2nd edition, 1975.
- [32] T. M. Aminabhavi and R. S. Khinnavar, "Diffusion and sorption of organic liquids through polymer membranes: 10. Polyurethane, nitrile-butadiene rubber and epichlorohydrin versus aliphatic alcohols (C_1 - C_5)," *Polymer*, vol. 34, no. 5, pp. 1006–1018, 1993.
- [33] U. S. Aithal, T. M. Aminabhavi, and S. S. Shukla, "Diffusivity, permeability, and sorptivity of aliphatic alcohols through polyurethane membrane at 25, 44, and 60 °C," *Journal of Chemical & Engineering Data*, vol. 35, no. 3, pp. 298–303, 1990.
- [34] G. W. C. Hung and J. Autian, "Use of thermal gravimetric analysis in sorption studies II: evaluation of diffusivity and solubility of a series of aliphatic alcohols in polyurethane," *Journal of Pharmaceutical Sciences*, vol. 61, no. 7, pp. 1094–1098, 1972.
- [35] H. Kumar and Siddaramaiah, "A study of sorption/desorption and diffusion of substituted aromatic probe molecules into semi interpenetrating polymer network of polyurethane/poly-methyl methacrylate," *Polymer*, vol. 46, no. 18, pp. 7140–7155, 2005.
- [36] Y. M. Sun and J. Chen, "Sorption/desorption properties of ethanol, toluene, and xylene in poly(dimethylsiloxane) membranes," *Journal of Applied Polymer Science*, vol. 51, no. 10, pp. 1797–1804, 1994.
- [37] J. Burke, "Solubility parameters: theory and application," *The American Institute for Conservation Annual*, vol. 3, pp. 13–58, 1984.
- [38] C. M. Hansen, *The three Dimensional Solubility Parameters and Solvent Diffusion Coefficient*, Danish Technical Press, Copenhagen, Denmark, 1967.
- [39] M. Karimi, "Diffusion in polymer solids and solutions," *Mass Transfer in Chemical Engineering Processes*, pp. 17–41, InTech, 2011.
- [40] E. Muñoz and J. A. García-Manrique, "Water absorption behaviour and its effect on the mechanical properties of flax fibre reinforced bioepoxy composites," *International Journal of Polymer Science*, vol. 2015, Article ID 390275, 10 pages, 2015.
- [41] E. Mahmoudinezhad, A. Marquardt, G. Eggeler, and F. Varnik, "Molecular dynamics simulations of entangled polymers: the effect of small molecules on the glass transition temperature," *Procedia Computer Science*, vol. 108, pp. 265–271, 2017.
- [42] E. Ghobadi, M. Heuchel, K. Kratz, and A. Lendlein, "Influence of the addition of water to amorphous switching domains on the simulated shape-memory properties of poly(l-lactide)," *Polymer*, vol. 54, no. 16, pp. 4204–4211, 2013.
- [43] H. Khajehsaeid, J. Arghavani, R. Naghdabadi, and S. Sohrabpour, "A visco-hyperelastic constitutive model for rubber-like materials: a rate-dependent relaxation time scheme," *International Journal of Engineering Science*, vol. 79, pp. 44–58, 2014.
- [44] A. J. W. McClung, G. P. Tandon, and J. W. Baur, "Deformation rate-, hold time-, and cycle-dependent shape-memory performance of veriflex-e resin," *Mechanics of Time-Dependent Materials*, vol. 17, no. 1, pp. 39–52, 2013.
- [45] D. Santiago, F. Ferrando, and S. De la Flor, "Influence of holding time on shape recovery in a polyurethane shape-memory polymer," *Journal of Materials Engineering and Performance*, vol. 23, no. 7, pp. 2567–2573, 2014.

- [46] J. K. Lee, K. H. Lee, and B. S. Jin, "Structure development and biodegradability of uniaxially stretched poly(l-lactide)," *European Polymer Journal*, vol. 37, no. 5, pp. 907–914, 2001.
- [47] Y. S. Wong, Z. H. Stachurski, and S. S. Venkatraman, "Orientation and structure development in poly(lactide) under uniaxial deformation," *Acta Materialia*, vol. 56, no. 18, pp. 5083–5090, 2008.
- [48] Y. S. Wong and S. S. Venkatraman, "Recovery as a measure of oriented crystalline structure in poly(l-lactide) used as shape memory polymer," *Acta Materialia*, vol. 58, no. 1, pp. 49–58, 2010.
- [49] X. L. Lu, W. Cai, Z. Gao, and W. J. Tang, "Shape memory effects of poly(L-lactide) and its copolymer with poly(ϵ -caprolactone)," *Polymer Bulletin*, vol. 58, no. 2, pp. 381–391, 2007.
- [50] C. Schmidt, K. Neuking, and G. Eggeler, "Functional fatigue of shape-memory polymers," *MRS Proceedings*, vol. 1190, 2009.
- [51] B. K. Kim, S. Y. Lee, and M. Xu, "Polyurethanes having shape memory effects," *Polymer*, vol. 37, no. 26, pp. 5781–5793, 1996.

Research Article

Experimental and Numerical Study of the Interfacial Shear Strength in Carbon Fiber/Epoxy Resin Composite under Thermal Loads

Hongxiao Wang ,¹ Xiaohui Zhang ,¹ Yugang Duan,¹ and Lingjie Meng²

¹School of Mechanical Engineering, State Key Laboratory for Manufacturing Systems Engineering, Xian Jiaotong University, 99 Yanxiang Road, Xian, Shaanxi 710054, China

²School of Chemical Engineering and Technology, Xian Jiao Tong University, 28 West Xianning Road, Xian, Shaanxi 710049, China

Correspondence should be addressed to Xiaohui Zhang; xarzxh@163.com

Received 13 October 2017; Revised 26 December 2017; Accepted 23 January 2018; Published 15 February 2018

Academic Editor: Qi Shen

Copyright © 2018 Hongxiao Wang et al. This is an open access article distributed under the Creative Commons Attribution License, which permits unrestricted use, distribution, and reproduction in any medium, provided the original work is properly cited.

This study examined the influence mechanism of temperature on the interfacial shear strength (IFSS) between carbon fiber (CF) and epoxy resin (EP) matrices under various thermal loads using experimental and numerical simulation methods. To evaluate the change in IFSS as a function of the increase in temperature, a microbond test was performed under controlled temperature environment from 23°C to 150°C. The experimental results showed that IFSS values of CF/EP reduce significantly when the temperature reaches near glass transition temperature. To interpret the effect of thermal loads on IFSS, a thermal-mechanical coupling finite element model was used to simulate the process of fiber pull-out from EP. The results revealed that temperature dependence of IFSS is linked to modulus of the matrix as well as to the coefficients of thermal expansion of the fiber and matrix.

1. Introduction

The interface between fiber and matrix plays an important role in fiber-reinforced composite materials by affecting directly the load transfer efficiency between the fiber and the matrix as well as the mechanical properties of the composites [1, 2]. The interfacial shear strength (IFSS) is a key parameter that influences the adhesion performance between the fiber and matrix [3, 4]. However, because of the heat instability of EP [5, 6] and the significant difference between the fiber and the EP matrix [7], IFSS becomes unstable as it is affected by the curing process as well as service temperature [8].

The coefficients of thermal expansion (CLTE) of EP matrices are almost 100 times higher than the longitudinal thermal expansion coefficient of CF and 10 times greater than the transverse thermal expansion coefficient of CF by absolute value. These differences cause residual thermal stress at the interface during the cooling process [9–11]. As a result, tremendous efforts have been devoted to overcoming these problems. For example, Sockalingam et al. [12] developed a finite element modeling methodology to simulate the residual thermal stress with large CLTE mismatch between the fiber

and the matrix caused by the cooling process. Also, Di Landro and Pegoraro [13] investigated the influence of the processing temperature and cooling rates on the residual stress in polymer composite matrices. They proposed that the residual thermal stress is mainly caused by the mismatch of CLTE between the fiber and matrix that importantly contributes to the fiber-matrix adhesion. Choo et al. [14] studied thermal path-dependency in the stress evolution of continuous-fiber-reinforced composites by comparing cooling and reheat cycles. Their results showed that the effect of time-dependent deformation becomes more significant as the fiber content increases and cooling/heating rate reduces. However, most of the above-mentioned studies mainly focus on the influence of the curing process of IFSS; only a handful of studies were devoted to investigating cured CF/EP service under elevated temperature work conditions.

In fact, IFSS also changed with serviced temperature. For example, Thomason and Yang [15] explored the temperature dependence of IFSS in glass fiber polypropylene composites (GF-PP) and noticed that IFSS in GF-PP is inversely dependent on the testing temperature with a major increase

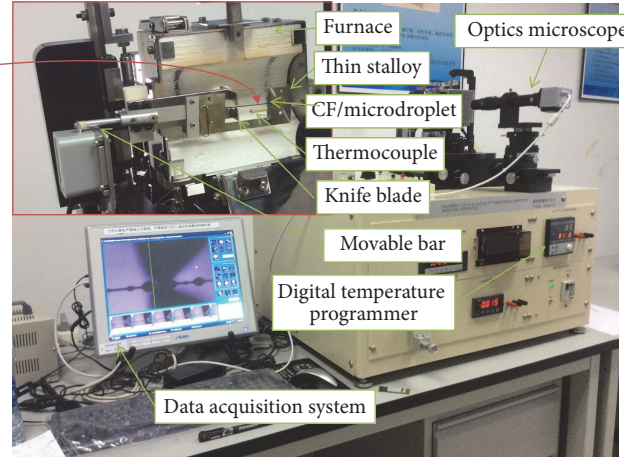
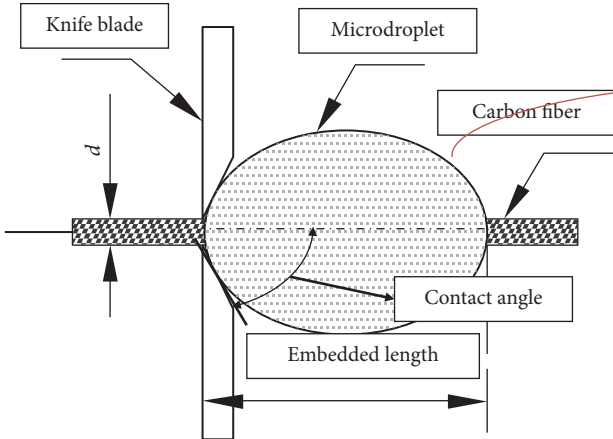


FIGURE 1: Temperature dependence HM410-microdroplet test equipment.

in glass transition region of the PP matrix. In their other paper [16], they found that the magnitude of the thermal residual stress due to mismatch in the thermal expansion coefficients of fiber and matrix was insufficient to explain the magnitude of the system IFSS, and they suggest that the residual stress combined with static adhesion could be the major contributor to the apparent interfacial adhesion in glass fiber-epoxy system, but they did not consider the effects of the temperature of resin on IFSS. In order to develop improved process ability and equipment operating at high temperature, Wang et al. [17] studied the thermal stability of carbon nanotube/epoxy nanocomposite by mechanical and interfacial evaluation at room temperature and 150°C. The results show that addition of low concentration CNT could improve the thermal stability of epoxy resin in turn hence the IFSS under high temperature. Also, the similar conclusions had been reached in similar studies [18]. So, when cured CF/EP service is under changing temperature work conditions, both the mismatch of CLTE between the fiber and matrix and the dependence-temperature of resin will cause a change in IFSS, hence affecting the CFRP performance. As a result, studying the mechanism of the influence of temperature on the interfacial properties of cured composites is of great importance.

The aim of this paper is to investigate the mechanism due to the influence of temperature on the interfacial properties of cured CFRP. In order to get the temperature dependence of IFSS, a microbond test was performed under controlled temperature; thermomechanical property tests were performed to get the Tg and the CLTE of resin matrix; tensile test was performed to measure the value of modulus changed with temperature. Furthermore, a FEM was developed to simulate the process of the microbond test under thermal loads to facilitate interpretation of the experiment observations. The FE analysis was carried out following three steps: (i) application of thermal preload and large mismatch in CTE between CF and EP to analyze the residual thermal stress due to the cooling process, (ii) modeling of the thermal stress in CF/EP under thermal preload through changes from room to the working temperature, and (iii) modeling the process of

single fiber pull-out from the microdroplet using the prestress of both residual thermal and thermal stresses.

2. Experimental

2.1. Materials and Test Sample. The EPs named TF1408 were obtained, respectively, from Hengshen Co. Ltd. Carbon fibers T300 were purchased from Toray Industries, Inc. The single CF was bonded on a thin stally adhered through microdroplet uncured EPs (Figure 1). All the samples were cured at 135°C and kept for 90 minutes in an oven, with the same heating rate and cooling rate of 3°C/min.

2.2. Microbond Testing. The temperature dependence of CF/EP IFSS was measured by HM410-microdroplet test equipment from TOHEI SANJOY, Japan (Figure 1). The temperature was automatically controlled and monitored through a digital temperature programmer. Five tests were performed at room temperature (RT), 60, 90, and 120°C.

The required force to pull out the fiber of cured epoxy resin is measured for each specimen and the interfacial shear strength τ_{IFSS} was estimated by [19, 20]

$$\tau_{\text{IFSS}} = \frac{F_{\max}}{\pi \cdot d_f \cdot l_e}, \quad (1)$$

where F_{\max} is the maximum value of pull-out force, d_f is the diameter of single fiber, and l_e is the embedded length of microdroplet. However, since at the moment when $F = F_{\max}$ the crack length is not zero and the measured F_{\max} value includes the contributions of interfacial adhesion and friction, the value of τ_{IFSS} calculated by (1) is the apparent IFSS.

The diameter of CF utilized in this study was 7 μm. For a big effect of specimen dimensions on the pull-out force and IFSS, the embedded length of EP microdroplet was maintained at 70–90 μm and the contact angle at 40–45°C (Figure 1). The load-displacement curve from each test was recorded to obtain the maximum force (F_{\max}) and a typical example is shown in Figure 2, where F_d is kink force [21]; when the pull-out force reaches this value, the fiber begins to debond from the matrix; F_{\max} is the peak force caused

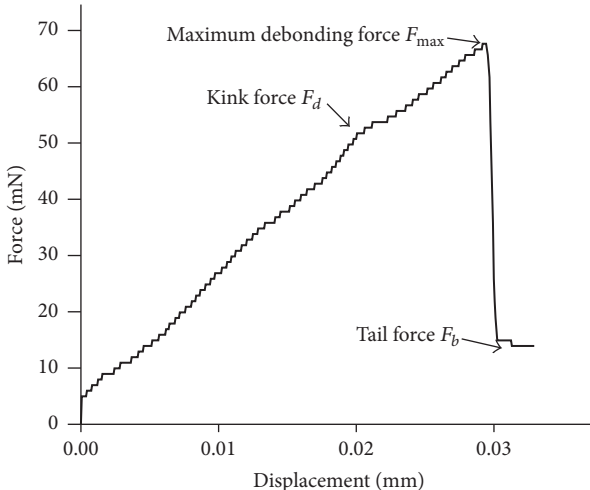


FIGURE 2: Load-displacement curve for the microdroplet test.

by debonding force and the frictional load in debonding regions; F_b is the tail force caused by frictional load when the embedded fiber totally debond from the matrix.

2.3. Thermomechanical Property Tests. The thermomechanical properties of EPs were tested by dynamic mechanical analysis (DMA) and thermal expansion analysis [22]. A dynamic mechanical analyzer (DMA Q800) was used for measurement of the glass transition temperature (T_g) as well as modulus versus temperature curve of both cured EPs. DMA tests were conducted using three-point bending modes (ASTM D5023-15) as it can provide the most analogous approach to normal mechanical testing method [23]. According to ASTM D5023-15, the dimensions utilized for DMA tests were ($60 \times 13 \times 3$ mm) and temperature scanning measurements were performed from 20°C to 150°C at a heating rate of $3^\circ\text{C}/\text{min}$ and an oscillation frequency of 1 Hz. To ensure that measured temperature range includes the temperature of T_g , the real temperature sweep test was performed from 0°C to 200°C . According to ASTM E289, the coefficient of the linear thermal expansion (CLTE) of EPs was measured using a dilatometer (DIL402C) from 20°C to 150°C at a heating rate $5^\circ\text{C}/\text{min}$ for CLTE test specimens of ($25 \times 5 \times 5$ mm).

2.4. Tensile Testing of Epoxy Resin. The moduli changed with different temperature were tested by this test. The temperature dependence of resin under tensile loading was determined using a universal testing machine (CMT4304; MTS, USA) according to the ASTM D638-10 "Standard Test Method for Tensile Properties of Plastics." The dumbbell-shaped samples (type I) were stretched using an extensometer at a rate of $2 \text{ mm}/\text{min}$ and stress-strain curves were recorded for ambient temperatures ranging from RT to 120°C (at 30°C intervals) within the climatic chamber. For each condition, 5 tests were performed.

3. Numerical Simulations Procedures

3.1. Finite Element Modeling. Commercial finite element software Abaqus[®] (version 6.10) was utilized to carry out

TABLE 1: Matrix properties at room temperature used for the numerical simulations.

Test temperature	RT	60°C	90°C	120°C
Young's modulus, E_m (MPa)	3960	3068	2510	1590
Poisson's ratio	0.37	0.37	0.37	0.37
Coefficient of thermal expansion ($10^{-6}/^\circ\text{C}$)	58	60	65	75

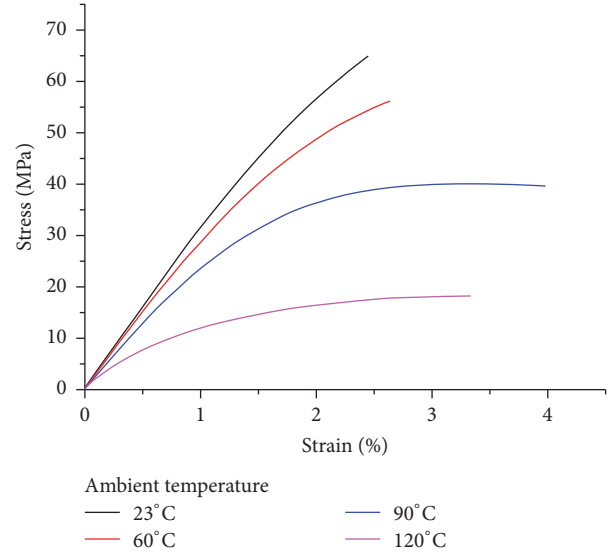


FIGURE 3: Representative stress-strain curves of the epoxy resin under different temperature conditions.

FE calculations. The baseline FE model of the microbond test consists of a single CF with a diameter of $7 \mu\text{m}$ and an epoxy matrix droplet with embedded length of $80 \mu\text{m}$ made by eight-node fully integrated solid elements. The matrix was modeled as an isotropic elastic material with properties shown in Table 1. Here, Young's modulus of resin was the slope of stress-strain curves under linear-elastic range and measured by tensile tests (Figure 3); the thermal expansion of resin under different temperatures was measured by CLTE tests (Figure 4). The fiber was modeled as an orthotropic elastic material with properties shown in Table 2 [24]. The knife blade was modeled as a rigid body and owing to its symmetry, only a quarter of the fiber and droplet were modeled (Figure 5).

3.2. Interfacial Behavior. The fiber-matrix interphase is subjected to the cohesive force and the residual compressive radial force, which results in a sliding friction force in the process of interfacial debonding. So in this study, the interfacial was modeled with cohesive element and coulomb friction contact behavior.

The zero thickness cohesive elements with a mixed-mode traction-separation law [25] (Figure 6) was used to model the process of interface debonding. The failure model of traction-separation used in this study is quadratic stress failure criterion [26] and a Benzeggagh-Kenane (BK) criterion [27] to evaluate, respectively, both the initial damage and

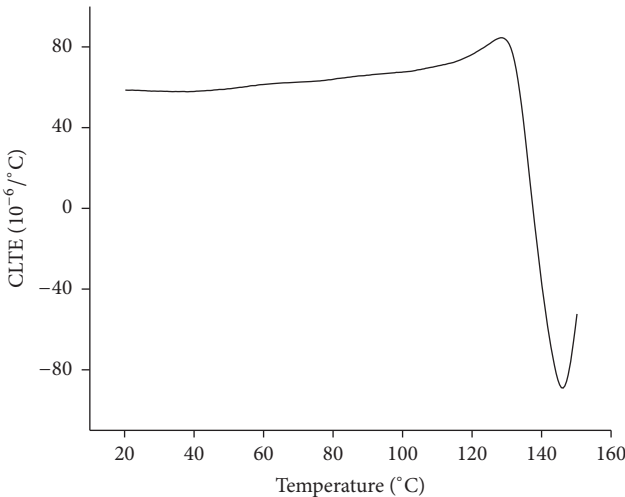


FIGURE 4: Coefficient of thermal expansion of epoxy resin versus temperature.

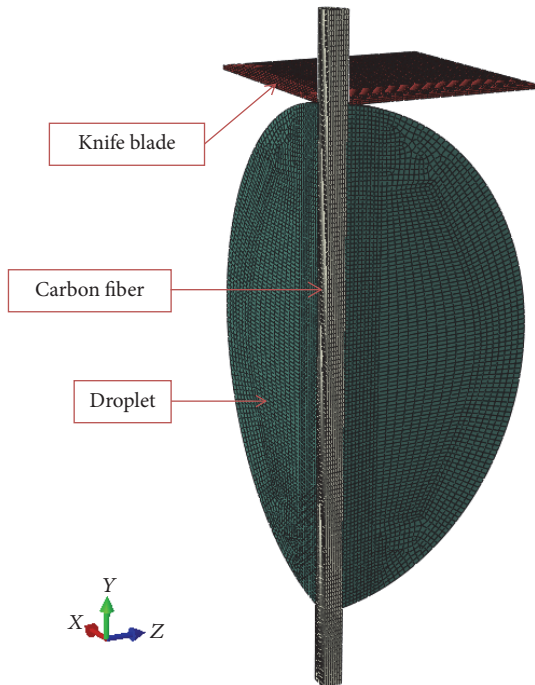


FIGURE 5: Quarter symmetric FEM of the microdroplet test.

crack propagation. The quadratic stress failure criterion was expressed through

$$\left(\frac{\max \langle \sigma_n, 0 \rangle}{N_{\max}} \right)^2 + \left(\frac{\sigma_t}{T_{\max}} \right)^2 + \left(\frac{\sigma_s}{S_{\max}} \right)^2 = 1, \quad (2)$$

where σ_n , σ_s , and σ_t are the stress components of, respectively, pure normal direction, first shear direction, and second shear direction. N_{\max} , S_{\max} , and T_{\max} are the interfacial strengths of, respectively, pure normal direction, first shear direction, and second shear direction. The stiffness coefficient of cohesive element is estimated using the peak stress and the maximum relative displacement by the results

of microbond test. The BK criterion for crack propagation can be evaluated through [27]

$$G_{IC} + (G_{IIC} - G_{IC}) \left\{ \frac{G_{II} + G_{III}}{G_I + G_{II} + G_{III}} \right\}^\eta = G_C, \quad (3)$$

where G_i and G_{iC} ($i = I, II, III$) are the corresponding strain energy release rates and fracture toughness under, respectively, pure mode I, mode II, and mode III loadings. $G_C = G_I + G_{II} + G_{III}$ is the fracture toughness, and η is the BK exponent. Fracture toughness G_{iC} is estimated using the kink force F_d issued from microdroplet test at stress-free temperature through [28]

$$G_{iC} = \frac{rC_{33s}}{2} \left[\frac{F_d}{\pi r^2} + \frac{(\alpha_A - \alpha_m) \Delta T}{2C_{33s}} \right]^2, \quad (4)$$

where F_d is the kink force measured from microbond test, r is the radius of the fiber, and α_A and α_m are, respectively, the axial coefficient for thermal expansion of the fiber and the matrix. ΔT is the difference between the test and stress-free temperatures and C_{33s} is given by

$$C_{33s} = \frac{1}{2} \left[\frac{1}{E_A} + \frac{V_1}{V_2 E_m} \right], \quad (5)$$

where E_A and E_m are, respectively, the fiber axial modulus and matrix tensile modulus. V_1 and V_2 are volume fractions of the fiber and the matrix, respectively. In this study, the traction law for mode I is assumed to be the same as modes II and III.

A coulomb friction is used to model the friction caused by residual compressive radial force. The coefficient of friction during progressive debonding is estimated by the ratio of tail force F_b tested by the results of microbond test (Figure 2) and the radial force caused by the residual thermal stress.

3.3. Residual Thermal Stress Analysis. The residual stresses due to thermal shrinkage during cooling down from the cure temperature to room temperature were simulated by application of thermal preload to the FE model. A thermal preload was applied using T_g as stress-free temperature and the operating temperature as room temperature (23°C). T_g of the epoxy resin was commonly used to define the stress-free temperature in calculation of the residual stress [29]. The model of the knife blade was suppressed in this step and instead an axisymmetric loading was applied to the matrix droplet and fiber. The mixed-mode damage and crack initiation loads were set on the fiber-matrix interphase.

3.4. Thermal Stress Analysis. The thermal stress analysis due to thermal preload was simulated under a prestress of residual thermal stress. A thermal preload was set on the fiber and matrix from room to working temperatures and Young's modulus of the matrix was modified to the corresponding temperature. The model of the knife blade was suppressed in this step too and axisymmetric loading was applied to the matrix droplet and the fiber. A mixed-mode damage and crack initiation loads were set on the fiber-matrix interphase.

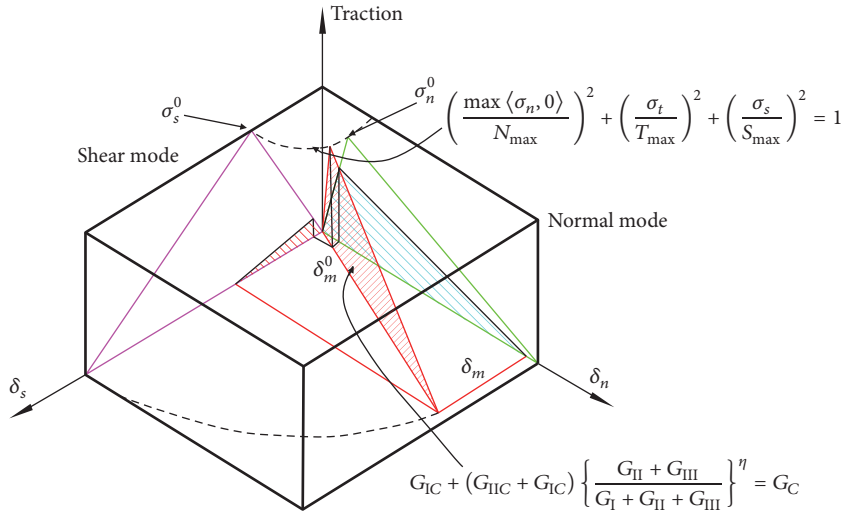


FIGURE 6: Mixed-mode traction-separation law.

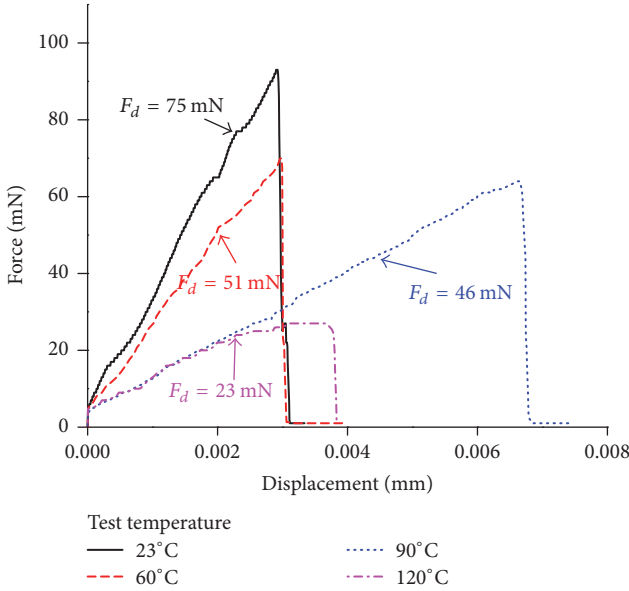


FIGURE 7: Force-displacement curves under different tested temperature by experiment results.

3.5. Microdroplet Debonding Analysis. The process of single fiber pull-out from the microdroplet was modeled under the prestress of residual thermal and thermal stresses. The knife blade was activated and fixed boundary conditions were applied to the knife blade. A contact property was set between the knife blade and droplet and constant displacement loading was applied to the fiber along the axial direction. An axisymmetric loading was applied to the matrix droplet and fiber and mixed-mode damage and crack initiation loads were set on the fiber-matrix interphase.

4. Results and Discussion

Figure 7 shows the force-displacement curve of microbond test under different temperature; the results show that the peak forces are decreased with tested temperature increasing.

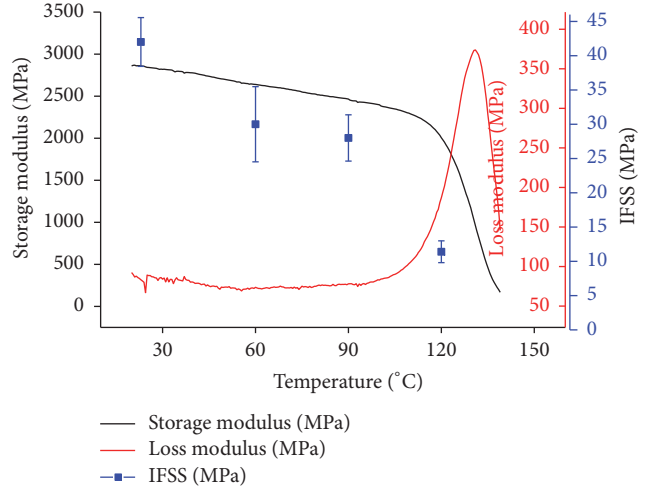


FIGURE 8: EPs matrix storage/loss modulus and apparent IFSS versus temperature.

Correspondently, the apparent IFSS also decreased with tested temperature increasing. Figure 8 illustrates results from the thermomechanical characterization of EPs obtained through DMA and apparent IFSS as a function of temperature. It can clearly be seen that the measured apparent IFSS for CF/EP is significantly affected by the thermal load, where apparent IFSS decreases substantially near T_g . Also, the change point of apparent IFSS decrease with temperature (about 120–130°C from Figure 8) is approximately equal to T_g of EPs (about 123–131°C from Figure 8).

Figure 9 depicts results from the process of fiber pull-out performed at three different temperatures, which further confirmed the effect of temperature on the apparent IFSS. It is clear that failure modes of the fiber pull-out significantly change as temperature increases. At processing temperatures below T_g , increasing the pull-out force induces a crack that propagates along the interface between the fiber and the matrix, where the droplet will be in complete debonding with

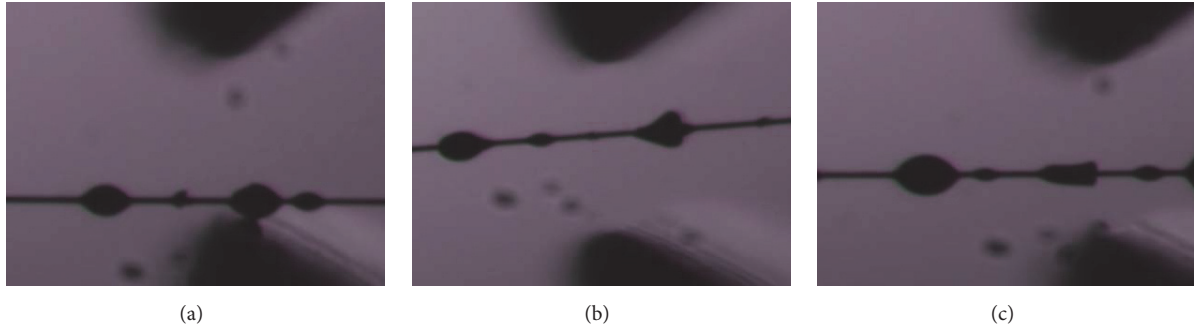


FIGURE 9: The process of fiber outperformed at different temperatures: (a) temperature $< T_g$; (b) temperature near to T_g ; and (c) temperature $> T_g$.

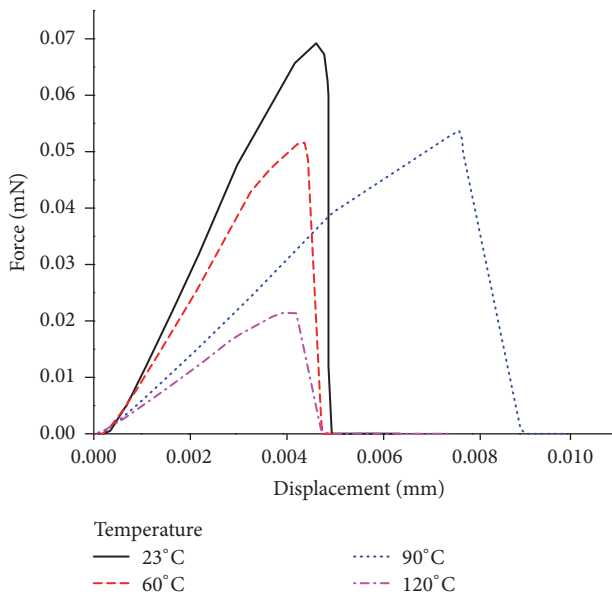


FIGURE 10: Simulated force-displacement curves under different temperature.

very little deformation (Figure 9(a)). When the processing temperature reaches T_g , the stiffness of EP reduces as the pull-out force increases. This induces the droplet to completely debond with larger deformation effect (Figure 9(b)). At processing temperature above T_g , modulus of EP becomes particularly weak due to the relaxation transition in the polymer. As the apparent IFSS is larger than EP, failure will be induced in EP (Figure 9(c)).

However, the above experiment results just proved the effect of temperature on the fiber pull-out peak force and apparent IFSS, the effect mechanism of the thermal stress and modulus on the apparent IFSS cannot be observed from the experiment results. So, it is necessary to analyze this question by finite element analysis. For the different fracture toughness, peak stress, stiffness coefficient of cohesive element, and the different modulus and CLET of resin matrix under 23, 60, 90, and 120°C were predicted by models with the same traction laws as shown in Figure 10. The values of apparent IFSS calculated by the peak force of the experiment and

TABLE 2: Carbon fiber properties at room temperature used for the numerical simulations.

Elastic properties	Carbon fiber
Longitudinal stiffness, E_{11} (MPa)	233130
Transverse stiffness, E_{22} (MPa)	23110
Out-of-plane stiffness, E_{33} (MPa)	23110
Poisson's ratio, ν_{12}	0.2
Poisson's ratio, ν_{13}	0.2
Poisson's ratio, ν_{23}	0.4
Shear modulus, G_{12} (MPa)	8960
Shear modulus, G_{13} (MPa)	8960
Shear modulus, G_{23} (MPa)	8270
Coefficient of thermal expansion α_1 ($10^{-6}/^{\circ}\text{C}$)	-0.54
Coefficient of thermal expansion α_2 ($10^{-6}/^{\circ}\text{C}$)	10.10

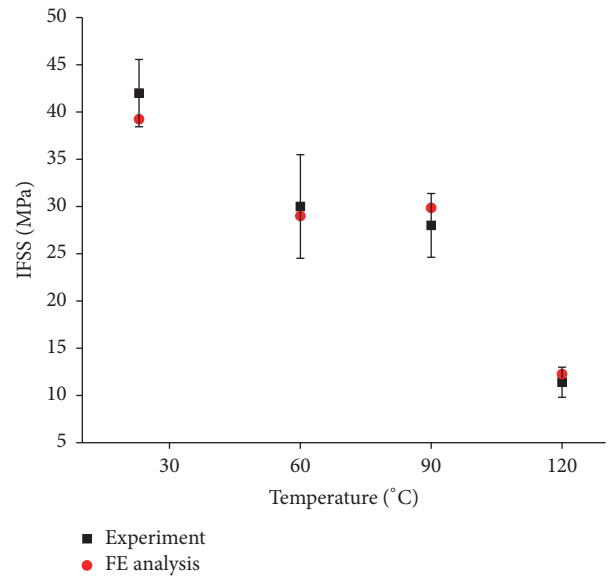


FIGURE 11: Comparison of apparent IFSS between the simulated and experimental data.

simulations are shown in Figure 11. It is clear from Figures 8 and 10 that, although there is still error, the trend of force-displacement curves of FE models is in good agreement with

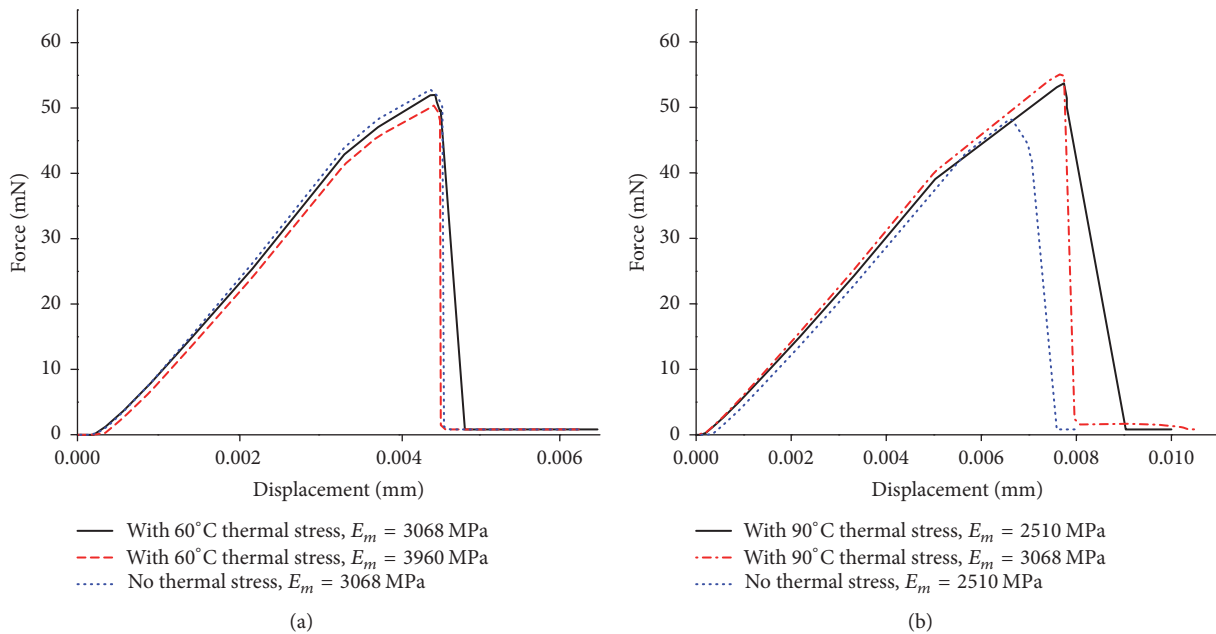


FIGURE 12: Simulated force-displacement curves for the effect of CLET and EP's modulus (a) under 60°C and (b) under 90°C.

the experimental results. And the value of apparent IFSS by FE analysis is in the error range of experimental data.

The results for the same fracture toughness, peak stress, stiffness coefficient of cohesive element with different modulus of EP, and thermal stress under 60 and 90°C are gathered in Figures 12(a) and 12(b). It can be observed from Figure 12 that the thermal stress caused by the mismatch of CLTE under higher temperature can increase the peak force; on the contrary, the peak forces are decreasing with the modulus of resin matrix under higher temperature. So, the temperature dependence of CF/EP IFSS was also linked to the thermal stress caused by the mismatch of CLTE and the modulus of resin matrix. Due to the mismatch of CLTE, the IFSS is increased with temperature increasing and is decreased in Young's modulus with temperature increasing. For the trend of IFSS is decreased with the temperature increasing in this study, the effect of the thermal stress caused by the mismatch of CLTE is lower than the modulus of matrix with temperature increasing.

5. Conclusions

The effects of temperature on the interfacial properties of CF/EP were investigated through a microbond test under controlled temperature environment. The experimental results revealed that apparent IFSS for CF/EP at temperatures below that of glass transition of EP does not show a significant decrease. However, this becomes significantly reduced at higher temperatures than that of glass transition. To interpret the experimental results, a series of FE calculations were carried out to simulate the process of microbond test as a function of the thermal loads. The results show that the thermal stress caused by the mismatch of CLTE under higher temperature can increase the peak force and apparent

IFSS; on the contrary, the peak forces are decreasing with the modulus of resin matrix under higher temperature. The effect of the thermal stress caused by the mismatch of CLTE is lower than the modulus of matrix with temperature increasing.

Conflicts of Interest

The authors declare that there are no conflicts of interest regarding the publication of this paper.

Acknowledgments

The authors acknowledge the financial support by “the Fundamental Research Funds for the Central Universities” (no. xjj201760).

References

- [1] R. Minty, J. Thomason, and H. Petersen, *The Role of The Epoxy Resin: Curing Agent Ratio in Composite Interfacial Strength by Single Fibre Microbond Test*, 2015.
- [2] H. Li, Y. Wang, C. Zhang, and B. Zhang, “Effects of thermal histories on interfacial properties of carbon fiber/polyamide 6 composites: Thickness, modulus, adhesion and shear strength,” *Composites Part A: Applied Science and Manufacturing*, vol. 85, pp. 31–39, 2016.
- [3] K. M. Beggs, L. Servinis, T. R. Gengenbach, M. G. Huson, B. L. Fox, and L. C. Henderson, “A systematic study of carbon fibre surface grafting via in situ diazonium generation for improved interfacial shear strength in epoxy matrix composites,” *Composites Science and Technology*, vol. 118, pp. 31–38, 2015.
- [4] B. Liu, Z. Liu, X. Wang, G. Zhang, S. Long, and J. Yang, “Interfacial shear strength of carbon fiber reinforced polyphenylene sulfide measured by the microbond test,” *Polymer Testing*, vol. 32, no. 4, pp. 724–730, 2013.

- [5] O. Zabihi, H. Khayyam, B. L. Fox, and M. Naebe, "Enhanced thermal stability and lifetime of epoxy nanocomposites using covalently functionalized clay: Experimental and modelling," *New Journal of Chemistry*, vol. 39, no. 3, pp. 2269–2278, 2015.
- [6] G.-R. Xu, M.-J. Xu, and B. Li, "Synthesis and characterization of a novel epoxy resin based on cyclotriphosphazene and its thermal degradation and flammability performance," *Polymer Degradation and Stability*, vol. 109, pp. 240–248, 2014.
- [7] Y. Pan and A. A. Pelegri, "Influence of matrix plasticity and residual thermal stress on interfacial debonding of a single fiber composite," *Journal of Mechanics of Materials and Structures*, vol. 5, no. 1, pp. 129–142, 2010.
- [8] S.-L. Gao and J.-K. Kim, "Cooling rate influences in carbon fibre/PEEK composites. Part II: Interlaminar fracture toughness," *Composites - Part A: Applied Science and Manufacturing*, vol. 32, no. 6, pp. 763–774, 2001.
- [9] A. E. Litherland and T. Le'H, "Transcrysallized interphase in thermoplastic composites. II: Influence of interfacial stress, cooling rate, fibre properties and polymer molecular weight," *Journal of Materials Science*, 1992.
- [10] Y. Wang and T. H. Hahn, "AFM characterization of the interfacial properties of carbon fiber reinforced polymer composites subjected to hydrothermal treatments," *Composites Science and Technology*, vol. 67, no. 1, pp. 92–101, 2007.
- [11] M. Zhu, M. Li, Q. Wu, Y. Gu, Y. Li, and Z. Zhang, "Effect of processing temperature on the micro- and macro-interfacial properties of carbon fiber/epoxy composites," *Composite Interfaces*, vol. 21, no. 5, pp. 443–453, 2014.
- [12] S. Sockalingam, M. Dey, J. W. Gillespie Jr., and M. Keefe, "Finite element analysis of the microdroplet test method using cohesive zone model of the fiber/matrix interface," *Composites Part A: Applied Science and Manufacturing*, vol. 56, pp. 239–247, 2014.
- [13] L. Di Landro and M. Pogoraro, "Evaluation of residual stresses and adhesion in polymer composites," *Composites Part A: Applied Science and Manufacturing*, vol. 27, no. 9, pp. 847–853, 1996.
- [14] H. Choo, M. A. M. Bourke, and M. R. Daymond, "A finite-element analysis of the inelastic relaxation of thermal residual stress in continuous-fiber-reinforced composites," *Composites Science and Technology*, vol. 61, no. 12, pp. 1757–1772, 2001.
- [15] J. L. Thomason and L. Yang, "Temperature dependence of the interfacial shear strength in glass-fibre polypropylene composites," *Composites Science and Technology*, vol. 71, no. 13, pp. 1600–1605, 2011.
- [16] J. L. Thomason and L. Yang, "Temperature dependence of the interfacial shear strength in glass-fibre epoxy composites," *Composites Science and Technology*, vol. 96, pp. 7–12, 2014.
- [17] Z.-J. Wang, D.-J. Kwon, J.-Y. Choi et al., "Inherent and interfacial evaluations of carbon nanotubes/epoxy composites and single carbon fiber at different temperatures," *Composites Part B: Engineering*, vol. 91, pp. 111–118, 2016.
- [18] K. Guru, S. B. Mishra, and K. K. Shukla, "Effect of temperature and functionalization on the interfacial properties of CNT reinforced nanocomposites," *Applied Surface Science*, vol. 349, pp. 59–65, 2015.
- [19] F.-H. Zhang, R.-G. Wang, X.-D. He, C. Wang, and L.-N. Ren, "Interfacial shearing strength and reinforcing mechanisms of an epoxy composite reinforced using a carbon nanotube/carbon fiber hybrid," *Journal of Materials Science*, vol. 44, no. 13, pp. 3574–3577, 2009.
- [20] E. Pisanova, S. Zhandarov, E. Mäder, I. Ahmad, and R. J. Young, "Three techniques of interfacial bond strength estimation from direct observation of crack initiation and propagation in polymer-fibre systems," *Composites Part A: Applied Science and Manufacturing*, vol. 32, no. 3-4, pp. 435–443, 2001.
- [21] S. Zhandarov and E. Mäder, "Characterization of fiber/matrix interface strength: Applicability of different tests, approaches and parameters," *Composites Science and Technology*, vol. 65, no. 1, pp. 149–160, 2005.
- [22] H. Watanabe, N. Yamada, and M. Okaji, "Linear thermal expansion coefficient of silicon from 293 to 1000 K," *International Journal of Thermophysics*, vol. 25, no. 1, pp. 221–236, 2004.
- [23] S. Deng, M. Hou, and L. Ye, "Temperature-dependent elastic moduli of epoxies measured by DMA and their correlations to mechanical testing data," *Polymer Testing*, vol. 26, no. 6, pp. 803–813, 2007.
- [24] M. W. Hyer and S. R. White, *Stress Analysis of Fiber-Reinforced Composite Materials*: WCB, McGraw-Hill, 1998.
- [25] D. Systems, *ABAQUS V 610 3 Documentation*, 2011.
- [26] P. P. Camanho, C. G. Dávila, and M. F. De Moura, "Numerical simulation of mixed-mode progressive delamination in composite materials," *Journal of Composite Materials*, vol. 37, no. 16, pp. 1415–1438, 2003.
- [27] M. L. Benzeggagh and M. Kenane, "Measurement of mixed-mode delamination fracture toughness of unidirectional glass/epoxy composites with mixed-mode bending apparatus," *Composites Science and Technology*, vol. 56, no. 4, pp. 439–449, 1996.
- [28] R. J. Scheer and J. A. Nairn, "A Comparison of Several Fracture Mechanics Methods for Measuring Interfacial Toughness with Microbond Tests," *The Journal of Adhesion*, vol. 53, no. 1-2, pp. 45–68, 1995.
- [29] Y. Jia, W. Yan, and H.-Y. Liu, "Carbon fibre pullout under the influence of residual thermal stresses in polymer matrix composites," *Computational Materials Science*, vol. 62, pp. 79–86, 2012.

Research Article

Stimuli-Responsive Hydrogels Based on Polyglycerol Crosslinked with Citric and Fatty Acids

Leidy C. Solano-Delgado ,¹ César A. Bravo-Sanabria ,^{1,2}
Carolina Ardila-Suárez,^{1,2} and Gustavo E. Ramírez-Caballero 

¹Grupo de Investigación en Polímeros, Escuela de Ingeniería Química, Universidad Industrial de Santander (UIS), Bucaramanga, Colombia

²Centro de Investigaciones en Catálisis, Escuela de Ingeniería Química, Universidad Industrial de Santander (UIS), Bucaramanga, Colombia

Correspondence should be addressed to Gustavo E. Ramírez-Caballero; gusramca@uis.edu.co

Received 26 October 2017; Accepted 24 December 2017; Published 1 February 2018

Academic Editor: Junshi Zhang

Copyright © 2018 Leidy C. Solano-Delgado et al. This is an open access article distributed under the Creative Commons Attribution License, which permits unrestricted use, distribution, and reproduction in any medium, provided the original work is properly cited.

Polyglycerol-based hydrogels from biodegradable raw materials were synthesized by crosslinking reactions of polyglycerol with citric and fatty acids. Three hydrogels were studied varying molar ratios of crosslinking agent. It was found that crosslink amount, type, and size play a crucial role in swelling, thermal, mechanical, and stimuli-responsive properties. The hydrogels absorption capacity changed in response to temperature and pH external stimuli. The hydrogel with the highest swelling capacity absorbed more than 7 times its own weight at room temperature and pH 5. This material increased 14 times its own weight at pH 10. Creep-recovery tests were performed to study the effect of crosslinking agent on mechanical properties. Deformation and percentage of recovery of synthesized hydrogels were obtained. Formation of hydrogels was confirmed using FTIR, and physicochemical properties were analyzed by Scanning Electron Microscopy (SEM), Differential Scanning Calorimetric (DSC), and Dynamic Mechanical Analysis (DMA). This paper aims to give a contribution to biobased hydrogel knowledge from chemical, physicochemical, and mechanical point of view.

1. Introduction

Hydrogels are polymeric crosslinked, hydrophilic, three-dimensional networks that are not soluble in water but can absorb large quantities of this molecule [1, 2]. Due to their swelling ability, hydrogels have been studied extensively for a variety of applications such as drug delivery [3–6], agricultural applications [7, 8], removal of impurities in aqueous solutions [9, 10], biosensors [11], and spectrophotometric determination of drugs [12]. In these applications, swelling capacity and thermal, mechanical, and stimuli-responsive properties are of most interest. These properties are prescribed by the intrinsic properties of the main chain polymer and the crosslinking characteristics, such as type, amount, and size of crosslinking molecules, as well as environmental conditions. In this work, synthesized hydrogels are based on renewable materials; the main chain polymer is polyglycerol, obtained by glycerol polymerization [13], and citric and

fatty acids are the crosslinking molecules. Polyglycerol has a biocompatible and flexible polyether backbone with a high number of hydrophilic functional groups, which increases polyglycerol versatility and enables the production of hydrogels [14]. Citric acid is a relatively small and multifunctional monomer with pendant functional groups that allow future ester bond-crosslink and hydrogen bonding [15, 16]. Fatty acids are relative long monomers with a carboxylic functional group that with chemical modification of double-double bond of unsaturated fatty acids allows the formation of crosslinked polymer structures [17]. The present study focuses on the synthesis and characterization of novel polymeric materials from biodegradable monomers that respond to pH and temperature stimuli. The effect of type, amount, and size of crosslinking agents on thermal, mechanical, and stimuli-responsive properties was investigated.

Previous studies have reported the synthesis of hydrogels by crosslinking glycerol-derived polyglycerol with

TABLE 1: Composition of fatty acids used as crosslinking agent. Characterization was made using a gas chromatography system (Agilent Technologies 6890 series), coupled to a FID detector, using an Agilent DB23 column and SUPELCO 38 FAMES as standards.

Fatty acid	Area percentage (%)
Palmitic	9.08
Stearic	8.12
Oleic	32.14
Linoleic	36.31
Linolenic	3.56
Eicosenoic	4.06
Others	6.71

poly(ethylene glycol) diglycidyl ether PEGDE [14]. The resulting hydrogels exhibited pH-dependent swelling behavior with a higher swelling capability at acidic pH value, compared with swelling at neutral and basic pH values. Significant research has been focused on materials that change their properties in response to external physical and chemical stimuli such as pH, electric field, temperature, and ionic strength of the swelling agent, due to acid or basic pendant functional groups present on the polymer backbone [18–21]. Citric acid has been used as crosslinking agent for hydrogels production, for instance, with poly(vinyl alcohol) [22], with varying glycol unit (ethylene glycol, diethylene glycol, and triethylene glycol) [23], and with cellulose [24]. Fatty acids, such as linoleic and oleic acid, have been traditionally used to improve mechanical properties and chemical resistance in polymeric materials [25, 26].

Formation of hydrogels was confirmed using FTIR. Pendant acidic functional groups were identified in the polymer network which either accepts or releases protons as result of changing external pH. The calorimetric analysis was performed to study the effect of amount and size of crosslinking agents on glass transition temperature. Creep-recovery tests were conducted to elucidate structure-property relationship in mechanical properties. Hydrogels swelling behavior was determined at different pH and temperatures. Finally, SEM micrographs were taken to study morphological properties.

2. Materials and Methods

2.1. Materials. Glycerol (85%) and Sulfuric acid (95%) were obtained from Merck. Citric acid (99%) is a commercial product of Suquin Ltda., Bucaramanga, Co. The mixture of fatty acids used in this study was purchased from *Laboratorios León S.A.*, Bucaramanga, Co. Its composition is listed in Table 1.

2.2. Experimental Procedure

2.2.1. Hydrogels Synthesis. Hydrogels synthesis was carried out in two steps using the same reaction system: first step, polymerization reaction of glycerol to produce polyglycerol, and second step, crosslinking reaction of polyglycerol; see Figure 1. The reaction system consisted in a 50 mL glass

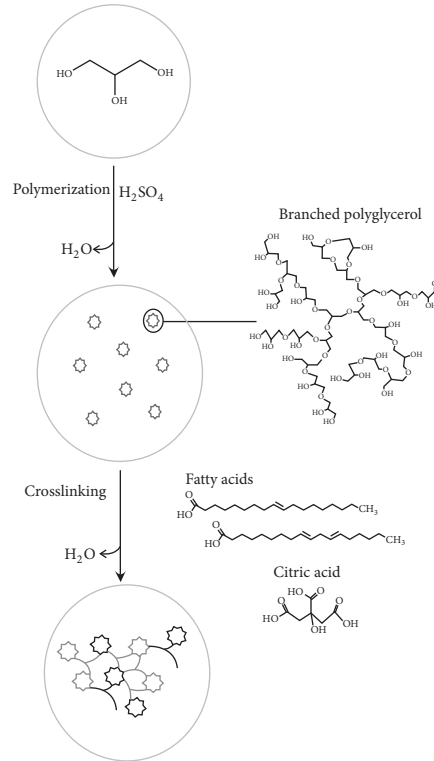


FIGURE 1: Schematic representation of hydrogel synthesis. First, the glycerol polymerization and the subsequent addition of crosslinking agents.

reactor equipped with a nitrogen inlet, catalyst feeding, thermometer inlet, and a distillation trap to continuously remove water from the reaction mixture. The temperature was maintained at 160°C using a temperature-controlled heating bath. A vacuum pump was attached to the reactor through the condenser. Condensation reactions were carried out at pressure of 22 in Hg. 4.8% w/w of Sulfuric acid was used as a catalyst [13]. The crosslinking agents were added to the reaction mass of polymerized glycerol, just before reaching the gel point, without further addition of catalyst. The reaction proceeded until the hydrogel reached the gel point.

Three different hydrogels were synthesized changing the nature of crosslinking agent: a hydrogel with citric acid as crosslinking agent, a hydrogel with fatty acids as crosslinking agent, and a hydrogel with both citric and fatty acids as crosslinking agent. Molar ratio between polyglycerol hydroxyl groups and crosslinking agents carboxyl groups and molar composition of crosslinking agents of synthesized hydrogels are reported in Table 2. After polymerization and crosslinking process, the hydrogels were washed with distilled water to remove catalyst and unreacted monomers.

2.3. Characterization. The synthesized hydrogels were tested to determinate their swelling behavior as a function of time in distilled water at room conditions. Absorption measurements were also made at 35°C, 55°C, and 85°C and pH 4, 7, and 10 to establish if the synthesized hydrogels have a response to temperature and pH. The absorption tests at different pH

TABLE 2: Samples compositions used for the hydrogels synthesis.

Hydrogel	Molar ratios of OH groups of polyglycerol (PG) : COOH groups of crosslinking agents (CG)	Molar compositions of COOH groups of citric acid (CA) and fatty acids (FFAs)
PG-FFAs	1 : 0.05	100% FFAs
PG-CA	1 : 0.45	100% CA
PG-(CA, FFAs)	1 : 0.5	90% CA-10% FFAs

were performed using *Hanna Instruments* buffer solutions. All measurements were done in triplicate. The hydrogels water absorption was calculated using (1) [14].

$$\% S = \frac{W_s - W_d}{W_d} * 100\%, \quad (1)$$

where W_d is the dry hydrogel weight and W_s is the swollen hydrogel weight.

Fourier Transform Infrared Spectroscopy (FTIR) was used to identify functional groups in synthesized hydrogels. The infrared spectra were obtained in transmittance mode in a Thermo Scientific spectrometer (Nicolet 1550 FTIR). Glass transition temperatures were obtained using Differential Scanning Calorimetry (DSC), and measurements were carried out on a DSC Discovery, TA Instruments, Inc. (USA). The samples were subjected to the following thermal schedule: first heating from -80°C to 180°C at $5^{\circ}\text{C}/\text{min}$ to eliminate volatile substances and thermal history of the materials; second, a cooling from 180°C to -90°C at $10^{\circ}\text{C}/\text{min}$; third, final heating from -90°C to 200°C . All scans were performed under nitrogen purge gas of $50\text{ mL}/\text{min}$. Scanning Electron Microscopy (SEM) measurements were performed to study the morphology of synthesized hydrogels. Samples were pretreated by being fully swollen in distilled water, then frozen in liquid nitrogen, and lyophilized for 72 h. Freeze-dried hydrogels were consequently fractured for morphology visualization. The uncoated environmental SEM images were taken using a Quanta FEG 650 at acceleration voltages of 15 kV . Creep-recovery tests of synthesized hydrogels were tested using Dynamic Mechanical Analysis (DMA), and measurements were carried out on a Q800 dynamic mechanical analyzer, TA Instruments Inc. (USA). The samples were swollen and tests were carried out in water medium. Treatments were compressed at 0.007 MPa during 20 min at three different temperatures; after that, the samples were recovered for 20 min.

3. Results and Discussion

3.1. FTIR Spectral Studies of Polymeric Hydrogels. Fourier Transform Infrared Spectroscopy (FTIR) analysis was conducted to synthesized hydrogels and compared with polyglycerol spectra; see Figure 2. The hydrogels and polyglycerol spectra show hydroxyl group band from 3050 to 3600 cm^{-1} indicative of alcohol groups. Hydrogels O-H stretch exhibits a loss of intensity in comparison with polyglycerol as a consequence of crosslinking linkages. The C-H stretching band was

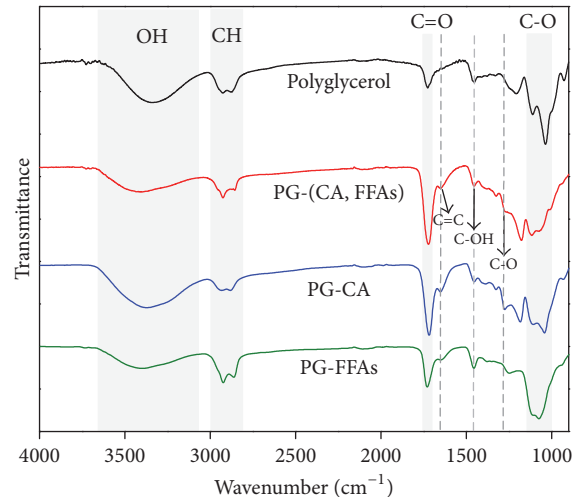


FIGURE 2: FTIR spectra of glycerol-derived polyglycerol and polyglycerol-based hydrogels. The main peaks associated with the structures are highlighted.

observed from 2800 to 3000 cm^{-1} [27]. Hydrogels with fatty acids as crosslinking agents, treatment PG-(CA, FFAs), and treatment PG-FFAs show well-defined C-H stretching as a consequence of hydrocarbon chains of fatty acids. Absorption in the range of 1700 – 1750 cm^{-1} in hydrogels spectrum is related to C=O stretch of aliphatic esters produced by esterification reactions between polyglycerol hydroxyl groups with carboxylic groups present in citric acid and fatty acids. In the specific case of polyglycerol, this absorption is due to acrolein formation [28]. Absorption at 1650 cm^{-1} is associated with C=C group of both unsaturated fatty acids and undesired products such as acrolein.

The spectra showed a peak at 1455 cm^{-1} that corresponds to C-OH in-plane bending and CH₂ bending [28]. The peaks appearing at 1235 – 1290 cm^{-1} in hydrogels spectrum are related to C-O vibration of unreacted carboxylic groups. These pendant acidic functional groups will play a crucial role in stimuli-responsive properties. The C-O vibration of unreacted carboxylic groups is highlighted in Figure 3. It is observed that hydrogel PG-FFAs exhibits lower C-O vibration intensity in comparison with hydrogels that have citric acid as crosslinking agent. This result is due to citric acid structure, which has three carboxylic functional groups, and not all of them react in the crosslink reaction. Finally, absorption at 1000 – 1150 cm^{-1} is related to C-O stretching of the ether groups present in the polyglycerol backbone [14] and etherification reactions between polyglycerol and crosslinking agents. Polyglycerol hydroxyl groups can react by etherification reactions with citric acid hydroxyl group and with fatty acids hydrated carbon-carbon double bonds.

3.2. Thermal Properties. Treatment PG-FFAs exhibits the lowest glass transition at 40.76°C (Figure 4), which is related to the lowest crosslink density and long chain size of fatty acids used as crosslinking agent. Therefore, less temperature is needed to change the hydrogel state from glassy to rubbery.

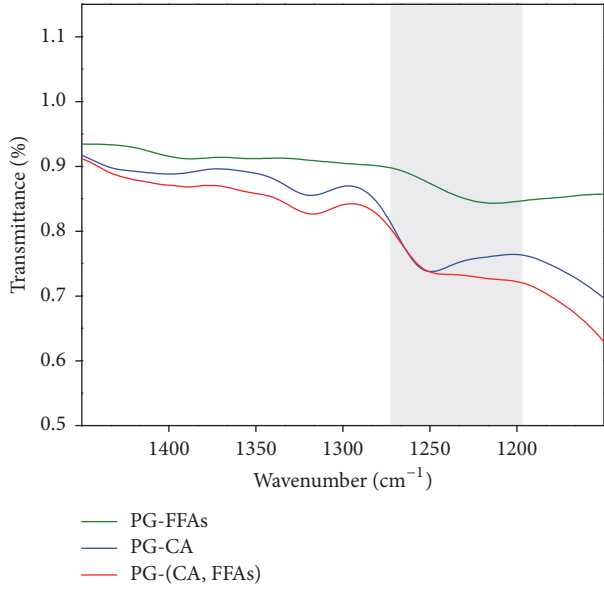


FIGURE 3: Zoom of the FTIR spectra at $1235\text{--}1290\text{ cm}^{-1}$ of the three synthesized hydrogels. The highlighted C-O vibration is related to the unreacted carboxylic groups.

On the other hand, treatment PG-CA exhibits the highest glass transition at 50.70°C . This result is due to higher crosslink density and citric acid short chain, which gives less flexibility to the material. In the particular case of hydrogel PG-(CA, FFAs), this material exhibits a glass transition temperature at 42.87°C , which is between the two glass transitions just described. This result can be explained by the combined features of each used crosslinking agent.

3.3. Mechanical Properties. The adequacy of hydrogels for specific applications depends on their mechanical properties and response times [29]. In this work, mechanical properties were evaluated by a creep-recovery test at different temperatures: 35°C , 55°C , and 70°C . Tests were performed in water medium simulating a typical condition of hydrogels in their applications. Results are shown in Figure 5. In general, all hydrogels have a small transition before a flat equilibrium region. Hydrogels deformation and percentage of strain recovery (SR) at different temperatures depend strongly on crosslink density, size, and type of crosslink agent. PG-FFAs present the highest deformation at all temperatures. This hydrogel has a slight variation of deformation at 35°C and 55°C and a significant increase in deformation at 70°C due to high molecular mobility at temperatures above glass transition temperature. Percentages of recovery of PG-FFAs are relatively low, 38.41, 41.45%, and 27.55% at 35°C , 55°C , and 70°C , respectively. High deformations and relatively low percentages of recovery of PG-FFAs hydrogel are due to low crosslink density and long chains of fatty acids used to form the network. High crosslink density and short chains of citric acid resulted in PG-CA hydrogels with relatively low deformation related to PG-FFA hydrogel. PG-CA hydrogel presented an increase in deformation and decrease in the

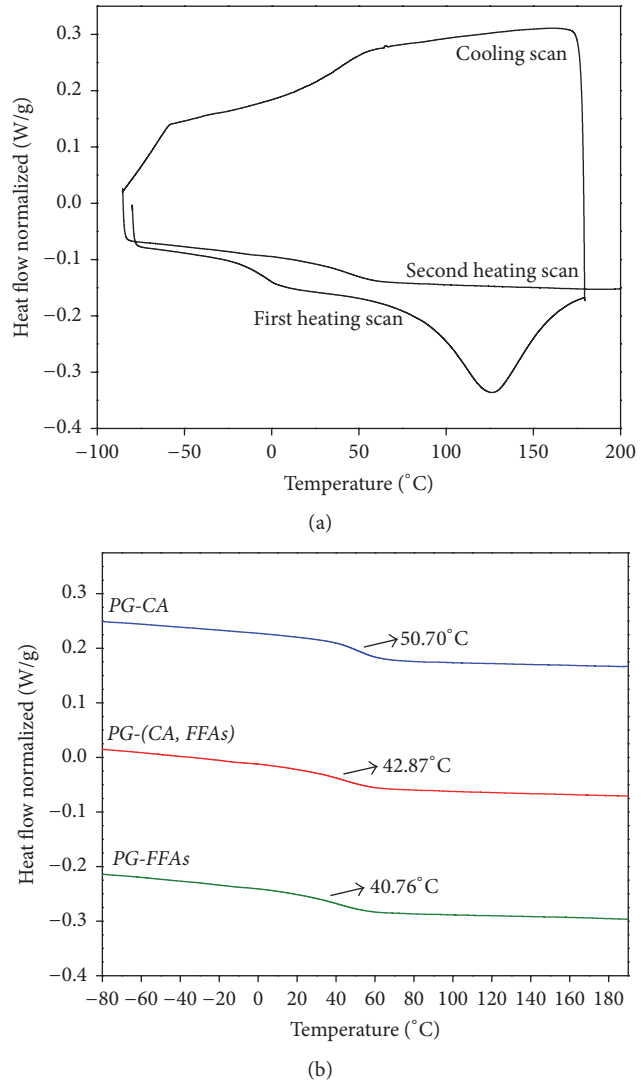


FIGURE 4: (a) First and second heating scan DSC result for hydrogels synthesized. (b) Hydrogels glass transition temperatures found in the second heating scan.

percentage of recovery as temperature increases. This result may be related to hydrogel chains mobility since glass transition temperature is 50°C . Finally, PG-(CA, FFAs) hydrogel has above 55°C the lowest deformation and the highest percentage of recovery of all hydrogels at this temperature.

3.4. Swelling Properties. The hydrogel with the highest swelling degree is PG-(CA, FFAs). It absorbs more than seven times its own weight; see Figure 6. This swelling behavior may be related to the contribution of both crosslinking agents; fatty acids long chains may contribute to large pore sizes, and unreacted hydroxyl groups of citric acid in addition to unreacted polyglycerol hydroxyl groups increase water affinity. Hydrogel PG-CA probably has smaller pore sizes for holding water caused by citric acid short chains. Finally, hydrogel PG-FFAS has only fatty acids that, despite its long

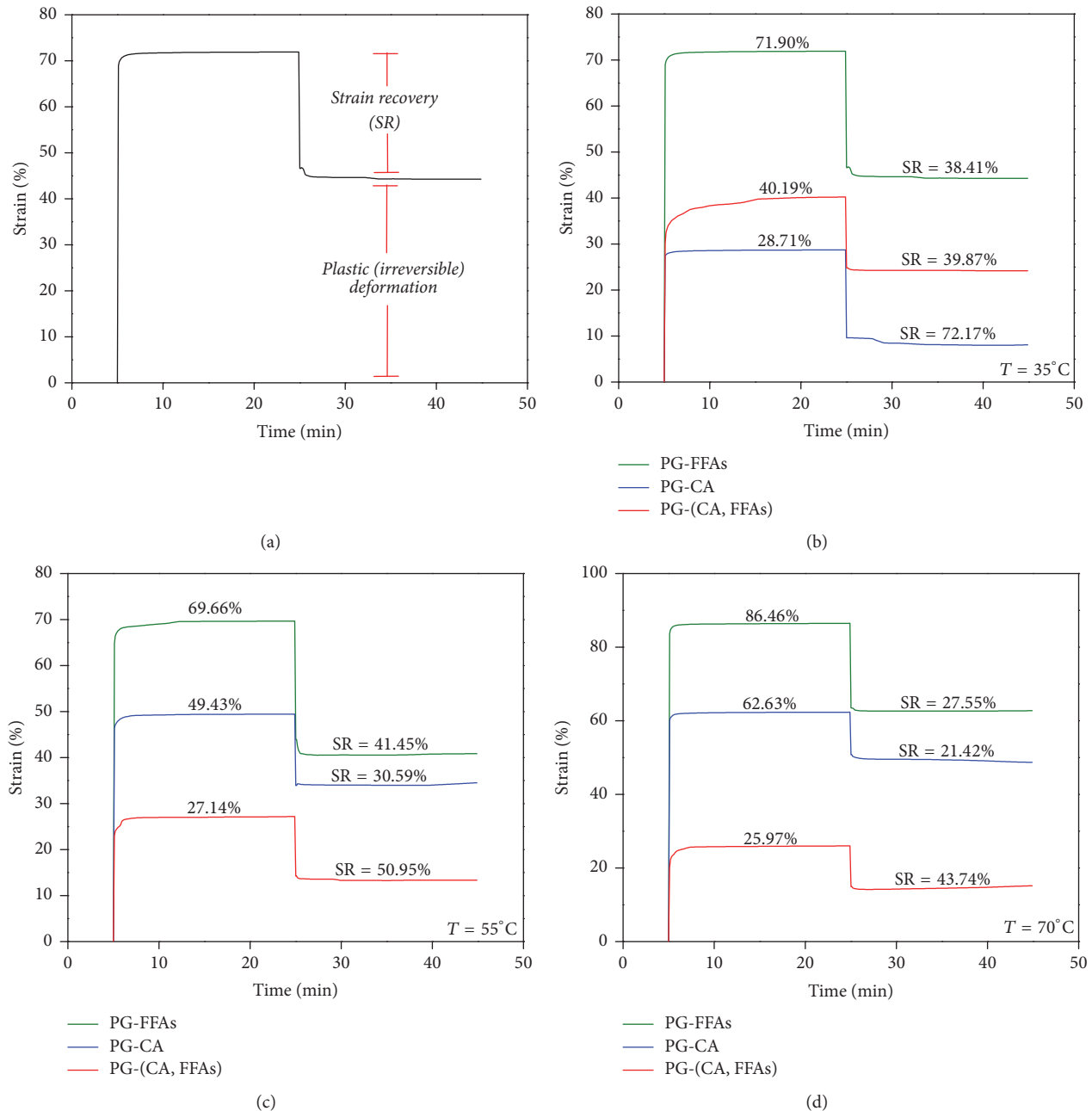


FIGURE 5: Submersion-compression creep for treatments PG-FFAs, PG-CA, and PG-(CA, FFAs) in DMA at 35°C , 55°C , and 70°C .

chain size, its crosslinking degree is low holding limited water molecules within its structure.

3.4.1. Effect of pH on Swelling Behavior. The swelling behavior of hydrogels was studied after 60 minutes of water absorption at pH 4, 5, 7, and 10. From the results, it was concluded that the hydrogels swelling behavior depends on external pH; see Figure 7. The greater swelling capability of hydrogel PG-(CA, FFAs) is observed when the pH value is 10, in which the hydrogel absorbs more than 13.7 times its own weight. At pH 4 and 7, the hydrogel also increases its swelling capability absorbing 8.6 and 10 times their own weights, respectively.

As reported in other studies [20, 30], an explanation for these results is that at basic pH values, the unreacted carboxylic groups become ionized producing carboxylate ions (RCOO^-), and H^+ combines with OH^- from basic solution forming H_2O . Negative charges of carboxylate ions create an electrostatic repulsion between the polymer chains forcing the hydrogel to uncoil, increasing free volumes in the hydrogel network.

In the specific case of treatment PG-FFAs, its swelling degree at high pH is lower in comparison with the other two treatments because this material presents less unreacted carboxylic groups; see Figure 3. A different trend result was

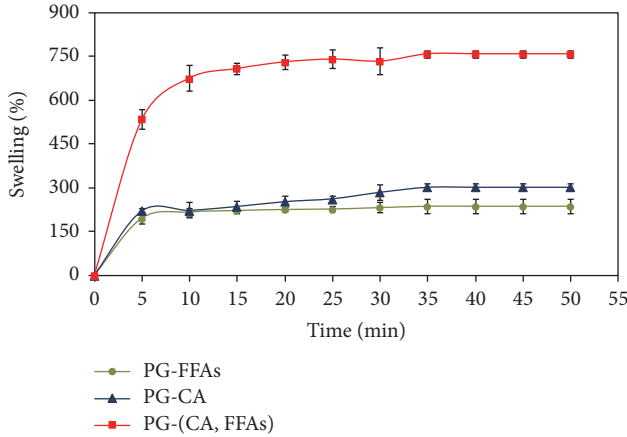


FIGURE 6: Swelling behavior of treatments PG-FFAs (●), PG-CA (▲), and PG-(CA, FFAs) (■). Measurements were taken at 20°C and pH 5 using (1).

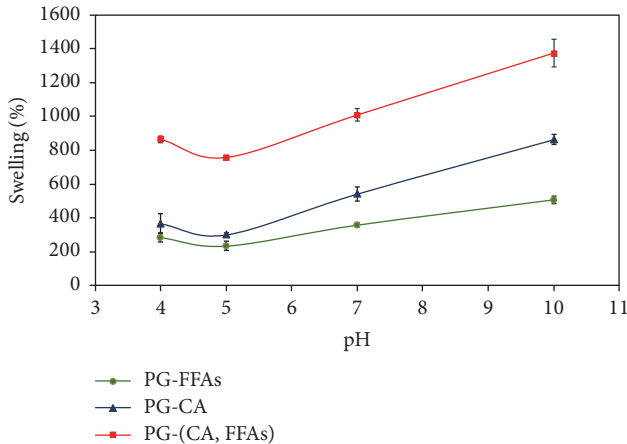


FIGURE 7: pH-dependent swelling behavior of treatments PG-FFAs (●), PG-CA (▲), and PG-(CA, FFAs) (■), measured at 25°C. Swelling percentage was calculated using (1).

obtained at pH 4 where hydrogels showed higher swelling behavior than that at pH 5; this can be related to the attraction of H⁺ ions to hydroxyl and ether groups, as reported before [14]. Swelling results at different pH correlate with unreacted carboxylic groups reported previously in FTIR results; see Figure 3; hydrogels with more free unreacted carboxylic groups have a greater response to changes in pH.

3.4.2. Effect of Temperature on Swelling Behavior. Hydrogels swelling behavior was studied after 60 minutes of water absorption at 20, 35, 55, and 85°C (Figure 8). Results show that at 35°C the three hydrogels present the lowest swelling degree. At this temperature, all hydrogels are below glass transition temperature as shown in Figure 4. At temperatures above 55°C, all hydrogels are above glass transition temperature. As a result, hydrogels chain mobility increases water absorption. The greater swelling capability is observed at 85°C where the PG-(CA, FFAs) hydrogel absorbs water 8.5 times its own weight.

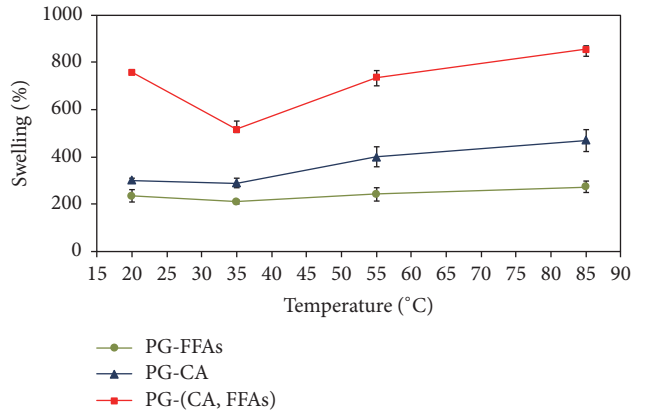


FIGURE 8: The temperature-dependent swelling behavior of treatments PG-FFAs (●), PG-CA (▲) and PG-(CA, FFAs) (■). Swelling percentage was calculated using (1).

3.5. Morphological Properties. Morphology of hydrogel PG-(CA, FFAs) is shown in Figure 9. It was found that the hydrogel exhibits an uneven, rough, heterogeneous, and slightly porous structure. The observed hydrogel pore heterogeneity (pore diameters from 2 to 62 μm) could be related to the randomness of crosslinking reactions between polyglycerol and citric-fatty acids which have different chain lengths and functional groups. Furthermore, the porous structure has interconnected pores forming open channels for capillary absorption of water; see Figure 9(b).

This material looks like a sponge and its swelling process follows the same principle, keeping the water within its structure due to its free volumes. This hydrogel may be considered as macroporous material according to IUPAC [31].

4. Conclusions

The effect of type, amount, and size of crosslinking molecules such as citric and fatty acids on thermal, mechanical, swelling, and stimuli-responsive polyglycerol-based hydrogel properties was studied. The small citric acid molecule used as crosslinking agent produced high crosslink density which manifested itself in higher glass transition temperature, relatively low hydrogel deformation, and higher amount of unreacted carboxylic functional groups that propitiated stimuli-responsive properties. On the other hand, large fatty acids molecules used as crosslinking agent produced low crosslink density which manifested itself in lower glass transition temperature, higher hydrogen deformation, and less unreacted carboxylic functional groups. It was concluded that it is possible to tune hydrogel properties by the judicious combination of citric and fatty acids crosslinking agents. The resulted hydrogel combining both crosslink agents has an intermediate glass transition temperature, relative short deformation with high recovery, and unreacted carboxylic functional groups that improved stimuli-responsive properties in comparison with hydrogels with uncombined crosslinking agents.

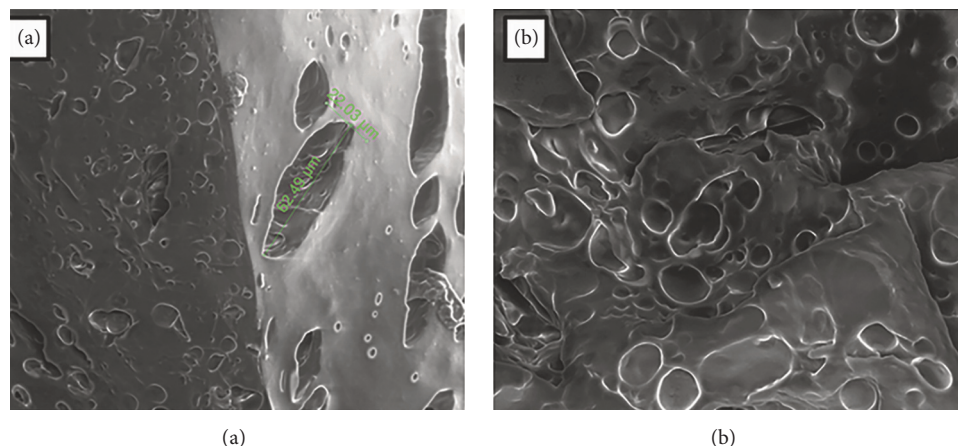


FIGURE 9: SEM micrographs of the hydrogel PG-(CA, FFAs).

Conflicts of Interest

The authors declare that they do not have any conflicts of interest.

Acknowledgments

This work was supported by Vicerrectoría de Investigación y Extensión at Universidad Industrial de Santander (UIS) and funded by the agreement of cooperation (Code 9460) between UIS, Corfasfatos, and Colciencias. Scanning Electron Microscopy (SEM) measurements were supported by Laboratory of Microscopy of Parque Tecnológico Guatiguará (PTG) - UIS. The authors thank Dr. Álvaro Ramírez for reviewing this paper.

References

- [1] A. Słoniewska and B. Palys, "Supramolecular polyaniline hydrogel as a support for urease," *Electrochimica Acta*, vol. 126, pp. 90–97, 2014.
- [2] E. S. Dragan, "Design and applications of interpenetrating polymer network hydrogels. A review," *Chemical Engineering Journal*, vol. 243, pp. 572–590, 2014.
- [3] L. Bédouet, F. Pascale, L. Moine et al., "Intra-articular fate of degradable poly(ethyleneglycol)-hydrogel microspheres as carriers for sustained drug delivery," *International Journal of Pharmaceutics*, vol. 456, no. 2, pp. 536–544, 2013.
- [4] D. S. Jones, G. P. Andrews, D. L. Caldwell, C. Lorimer, S. P. Gorman, and C. P. McCoy, "Novel semi-interpenetrating hydrogel networks with enhanced mechanical properties and thermoresponsive engineered drug delivery, designed as bioactive endotracheal tube biomaterials," *European Journal of Pharmaceutics and Biopharmaceutics*, vol. 82, no. 3, pp. 563–571, 2012.
- [5] Y. Liang and K. L. Kiick, "Heparin-functionalized polymeric biomaterials in tissue engineering and drug delivery applications," *Acta Biomaterialia*, vol. 10, no. 4, pp. 1588–1600, 2014.
- [6] N. K. Singh and D. S. Lee, "In situ gelling pH- and temperature-sensitive biodegradable block copolymer hydrogels for drug delivery," *Journal of Controlled Release*, vol. 193, pp. 214–227, 2014.
- [7] A. I. Raafat, M. Eid, and M. B. El-Arnaouty, "Radiation synthesis of superabsorbent CMC based hydrogels for agriculture applications," *Nuclear Instruments and Methods in Physics Research Section B: Beam Interactions with Materials and Atoms*, vol. 283, pp. 71–76, 2012.
- [8] C. Demitri, F. Scalera, M. Madaghiele, A. Sannino, and A. Maffezzoli, "Potential of cellulose-based superabsorbent hydrogels as water reservoir in agriculture," *International Journal of Polymer Science*, vol. 2013, Article ID 435073, 6 pages, 2013.
- [9] X. Ma, Y. Li, W. Wang, Q. Ji, and Y. Xia, "Temperature-sensitive poly(N-isopropylacrylamide)/graphene oxide nanocomposite hydrogels by in situ polymerization with improved swelling capability and mechanical behavior," *European Polymer Journal*, vol. 49, no. 2, pp. 389–396, 2013.
- [10] S. Saber-Samandari, S. Saber-Samandari, and M. Gazi, "Cellulose-graft-polyacrylamide/hydroxyapatite composite hydrogel with possible application in removal of Cu (II) ions," *Reactive and Functional Polymers*, vol. 73, no. 11, pp. 1523–1530, 2013.
- [11] T. Endo, R. Ikeda, Y. Yanagida, and T. Hatsuzawa, "Stimuli-responsive hydrogel-silver nanoparticles composite for development of localized surface plasmon resonance-based optical biosensor," *Analytica Chimica Acta*, vol. 611, no. 2, pp. 205–211, 2008.
- [12] M. Bahram, F. Hoseinzadeh, K. Farhadi, M. Saadat, P. Najafi-Moghaddam, and A. Afkhami, "Synthesis of gold nanoparticles using pH-sensitive hydrogel and its application for colorimetric determination of acetaminophen, ascorbic acid and folic acid," *Colloids and Surfaces A: Physicochemical and Engineering Aspects*, vol. 441, pp. 517–524, 2014.
- [13] C. Ardila-Suárez, D. Rojas-Avellaneda, and G. E. Ramirez-Caballero, "Effect of Temperature and Catalyst Concentration on Polyglycerol during Synthesis," *International Journal of Polymer Science*, vol. 2015, Article ID 910249, 8 pages, 2015.
- [14] S. Salehpour, C. J. Zuliani, and M. A. Dubé, "Synthesis of novel stimuli-responsive polyglycerol-based hydrogels," *European Journal of Lipid Science and Technology*, vol. 114, no. 1, pp. 92–99, 2012.
- [15] R. T. Tran, Y. Zhang, D. Gyawali, and J. Yang, "Recent developments on citric acid derived biodegradable elastomers," *Recent*

- Patents on Biomedical Engineering*, vol. 2, no. 3, pp. 216–227, 2009.
- [16] D. Gyawali, P. Nair, Y. Zhang et al., “Citric acid-derived in situ crosslinkable biodegradable polymers for cell delivery,” *Biomaterials*, vol. 31, no. 34, pp. 9092–9105, 2010.
 - [17] L. Fertier, H. Koleilat, M. Stemmelen et al., “The use of renewable feedstock in UV-curable materials-A new age for polymers and green chemistry,” *Progress in Polymer Science*, vol. 38, no. 6, pp. 932–962, 2013.
 - [18] M. Hamidi, A. Azadi, and P. Rafiei, “Hydrogel nanoparticles in drug delivery,” *Advanced Drug Delivery Reviews*, vol. 60, no. 15, pp. 1638–1649, 2008.
 - [19] H. Priya James, R. John, A. Alex, and K. Anoop, “Smart polymers for the controlled delivery of drugs – a concise overview,” *Acta Pharmaceutica Sinica B (APSB)*, vol. 4, no. 2, pp. 120–127, 2014.
 - [20] K. S. De, N. R. Aluru, B. Johnson, W. C. Crone, D. J. Beebe, and J. Moore, “Equilibrium swelling and kinetics of pH-responsive hydrogels: models, experiments, and simulations,” *Journal of Microelectromechanical Systems*, vol. 11, no. 5, pp. 544–555, 2002.
 - [21] T. Bartil, M. Bounekhel, C. Cedric, and R. Jeerome, “Swelling behavior and release properties of pH-sensitive hydrogels based on methacrylic derivatives,” *Acta Pharmaceutica*, vol. 57, no. 3, pp. 301–314, 2007.
 - [22] Z. Ajji, “Preparation of poly(vinyl alcohol) hydrogels containing citric or succinic acid using gamma radiation,” *Radiation Physics and Chemistry*, vol. 74, no. 1, pp. 36–41, 2005.
 - [23] D. S. Franklin and S. Guhanathan, “Synthesis and characterization of citric acid-based pH-sensitive biopolymeric hydrogels,” *Polymer Bulletin*, vol. 71, no. 1, pp. 93–110, 2014.
 - [24] C. Demitri, R. Del Sole, F. Scalera et al., “Novel superabsorbent cellulose-based hydrogels crosslinked with citric acid,” *Journal of Applied Polymer Science*, vol. 110, no. 4, pp. 2453–2460, 2008.
 - [25] G. Lligadas, J. C. Ronda, M. Galià, and V. Cádiz, “Oleic and undecylenic acids as renewable feedstocks in the synthesis of polyols and polyurethanes,” *Polymer*, vol. 2, no. 4, pp. 440–453, 2010.
 - [26] M. Moreno, M. Goikoetxea, and M. J. Barandiaran, “Biobased-waterborne homopolymers from oleic acid derivatives,” *Journal of Polymer Science Part A: Polymer Chemistry*, vol. 50, no. 22, pp. 4628–4637, 2012.
 - [27] H. S. Mansur, R. L. Oréfice, and A. A. P. Mansur, “Characterization of poly(vinyl alcohol)/poly(ethylene glycol) hydrogels and PVA-derived hybrids by small-angle X-ray scattering and FTIR spectroscopy,” *Polymer Journal*, vol. 45, no. 21, pp. 7193–7202, 2004.
 - [28] S. Salehpour, *Synthesis of stimuli-responsive hydrogels from glycerol*, University of Ottawa, 2012.
 - [29] S. Abdurrahmanoglu and O. Okay, “Rheological behavior of polymer-clay nanocomposite hydrogels: Effect of nanoscale interactions,” *Journal of Applied Polymer Science*, vol. 116, no. 4, pp. 2328–2335, 2010.
 - [30] J. Liu, Q. Li, Y. Su, Q. Yue, and B. Gao, “Characterization and swelling-deswelling properties of wheat straw cellulose based semi-IPNs hydrogel,” *Carbohydrate Polymers*, vol. 107, no. 1, pp. 232–240, 2014.
 - [31] M. Thommes, K. Kaneko, A. V. Neimark et al., “Physisorption of gases, with special reference to the evaluation of surface area and pore size distribution (IUPAC Technical Report),” *Pure and Applied Chemistry*, vol. 87, no. 9-10, pp. 1051–1069, 2015.

Research Article

Dynamic Electromechanical Response of a Viscoelastic Dielectric Elastomer under Cycle Electric Loads

Junjie Sheng  and Yuqing Zhang

Institute of Systems Engineering, China Academy of Engineering Physics, Mianyang 621999, China

Correspondence should be addressed to Junjie Sheng; scu2005sjj@163.com

Received 8 October 2017; Accepted 28 December 2017; Published 29 January 2018

Academic Editor: Jianwen Zhao

Copyright © 2018 Junjie Sheng and Yuqing Zhang. This is an open access article distributed under the Creative Commons Attribution License, which permits unrestricted use, distribution, and reproduction in any medium, provided the original work is properly cited.

Dielectric elastomer (DE) is able to produce large electromechanical deformation which is time-dependent due to the viscoelasticity. In the current study, a thermodynamic model is set up to characterize the influence of viscoelasticity on the electromechanical and dynamic response of a viscoelastic DE. The time-dependent dynamic deformation, the hysteresis, and the dynamic stability undergoing viscoelastic dissipative processes are investigated. The results show that the electromechanical stability has strong frequency dependence; the viscoelastic DE can attain a larger stretch in the dynamic response than the quasistatic actuation. Furthermore, with the decreasing frequency of the applied electric load, the viscoelastic DE system will present dynamic stability evolution from an aperiodic motion to the quasiperiodic motion. The DE system may also experience a stability evolution from a single cycle motion to multicycle motion with the increasing relaxation times. The value and variation trend of the amplitude of the stretch are highly dependent on the excitation frequency and the relaxation time.

1. Introduction

Due to their fast response time, soft, lightweight, low-cost, and high energy density, dielectric elastomers (DEs) have been developed to use in high performance applications as artificial muscles, Braille displays, life-like robots, tunable lens, and power generators [1–6]. It consists of a soft elastomeric membrane sandwiched between two compliant electrodes on both sides. Most of the existing studies on DEs have focused on quasistatic deformation [5–8], neglecting the effect of inertia and viscoelasticity.

However, to perform as an electromechanical actuator, a Dielectric elastomer (DE) is often subject to transient, time-dependent forces and voltages [9–11] and is mostly expected to deform at high frequencies in applications, where inertia and viscoelasticity can play a significant role in the dynamic application. Applications exploiting the dynamic behavior of DEs have long been realized through experiments including vibrotactile display for mobile applications [12], frequency tuning [13], pumps [14], and acoustic actuator [15]. Recently, researches have been also carried out on modeling the

nonlinear vibrations of hyperelastic DE membranes [16–19]. Zhu et al. [16] studied the resonant behavior of a prestretched membrane of a DE and subsequently analyzed the nonlinear oscillations of a DE balloon [17]. Based on simple geometrical and spherical capacitor assumptions, Yong et al. [18] investigated the dynamics of a thick-walled DE spherical shell. Li et al. [19] analyzed the electromechanical and dynamic analyses of tunable pure-shear DE-based resonator and identified the safe operation range for failure prevention while actuating the resonator. Xu et al. [20] obtained an analytical model for the DE by the Euler-Lagrange equation to study the dynamic analysis of a DE with stretching deformation. Jia et al. [21] investigated the response time and dynamic range for a DE actuator. Li et al. [22] presented an analysis of the nonlinear dynamics of a DE as electromechanical resonator (DEER) configured as a pure-shear actuator. An investigation in our previous paper [23] reported the nonlinear dynamic characteristics of a DE membrane undergoing in-plane deformation. Wang et al. [24] investigated the strain-stiffening effect on the nonlinear vibration of a circular DE membrane subjected to electromechanical load.

Although the above studies have attempted to model the nonlinear dynamical behavior of the DE to probe its time-dependent performance, they have neglected the viscoelasticity of DE. The time-dependency of a DE can cause dissipation in the system and significantly affect its dynamic performance and coupling efficiency [25, 26]. In particular, experiments have shown that viscoelasticity can significantly influence the electromechanical transduction and its application [4, 9, 10, 25–27].

Recently, a few studies have been developed concerning the dynamic performance of viscoelastic DE [28–32]. Zhang et al. [28] studied the coupled nonlinear oscillation and stability evolution of viscoelastic DE under nonequibaxial tensile forces by utilizing the method of virtual work, developed an analytical model to characterize the dynamic performance of a homogeneously deformed viscoelastic DE under the conditions of equal-biaxial force, uniaxial force, and pure-shear state by using the Euler-Lagrange equation [29], and predicted the damping effect on the dynamic performance of DE based on the standard linear solid rheological model [30]. Wang et al. [31] presented a model describing the nonlinear dynamic visco-hyperelastic behaviors of DE and explained the material's dynamic energy dissipation mechanism. However, the effect of viscoelasticity and relaxation time on hysteresis and stability evolution of the DE was neglected in previously reported papers. Zhang et al. [32] investigated the static and dynamic performance of a hinge configuration with integrated dielectric elastomers. Our previous paper [33] also investigated the effect of temperature on the dynamic electromechanical performance of viscoelastic dielectric.

Based on the theory of nonequilibrium thermodynamics [34–36] and the nonlinear vibration modeling [16–19], we aim to characterize the electromechanical and dynamic response of viscoelastic dielectric elastomer, to predict how viscoelasticity affect its dynamic performance and hysteresis process by comparing with the quasistatic response, and to present a physical interpretation on the instability and stability evolution coupled by viscoelasticity, relaxation time, and dynamic deformation.

In this study, the influence of the viscoelasticity effects on the electromechanical and dynamic characteristics of a DE membrane is considered by setting up a thermodynamic model. With the proposed model, the dynamic responses of a DE film subject to a cyclic electric field are investigated and compared with the quasistatic response. Then, the dynamic oscillation, phase diagrams, and Poincaré maps of the viscoelastic DE are studied. A detailed analysis shows the influence of the frequency, viscoelasticity, and relaxation time on the dynamic stability evolution and the hysteresis.

2. Thermodynamic Modeling of a Viscoelastic DE

Considering a piece of viscoelastic dielectric, it deforms when subject to both in-plane biaxial force and a voltage-induced force through the thickness. Figure 1 illustrates a membrane of a DE, sandwiched between two compliant electrodes. The DE deforms from its original configuration $L_1 \times L_2 \times L_3$ to

the current configuration $l_1 \times l_2 \times l_3$ in terms of an equal biaxial expansion. Here, we define λ_i ($i = 1, 2, 3$) = l_i/L_i as the stretch ratio. The stretch λ_i is homogeneous through the DE and is a function of time. Due to the incompressibility of the material, we express the stretch ratio in the thickness direction as $\lambda_3 = \lambda_1^{-1}\lambda_2^{-1}$.

The nominal stresses are defined as $s_1 = P_1/(L_2L_3)$ and $s_2 = P_2/(L_1L_3)$. The nominal electric field is $\tilde{E} = \Phi/L_3$ and the nominal electric displacement is defined by $\tilde{D} = Q/L_1L_2$, the true electric field by $E = \Phi/l_3$, and the true electric displacement by $D = Q/(l_1l_2)$. We adopt the model of ideal DE, assuming that the permittivity of the elastomer ε is taken to be constant. That is, the true electric displacement is taken to be linear in the true electric field, $D = \varepsilon E$ [19, 33, 34]. Based on the assumption of the DE membrane as a parallel capacitor, we obtain the relation between the charge and the voltage as

$$Q = \Phi \frac{\varepsilon L_1 L_2}{L_3} \lambda_1^2 \lambda_2^2. \quad (1)$$

When the membrane is subject to forces and voltage, all three quantities Φ , λ_1 , and λ_2 can vary, so that the variation of the charge is

$$\begin{aligned} \delta Q &= \frac{\varepsilon L_1 L_2}{L_3} \lambda_1^2 \lambda_2^2 \delta \Phi \\ &\quad + \Phi \frac{\varepsilon L_1 L_2}{L_3} (2\lambda_1 \lambda_2^2 \delta \lambda_1 + 2\lambda_2 \lambda_1^2 \delta \lambda_2). \end{aligned} \quad (2)$$

When the dimensions of the DE varies slightly by $\delta \lambda_1$ and $\delta \lambda_2$, the tensile forces do work of $P_1 L_1 \delta \lambda_1 + P_2 L_2 \delta \lambda_2$. Associated with a small amount of charge δQ moving through the conducting wire, the applied voltage does a work of $\Phi \delta Q$. During actuation, the inertia forces in each material element along the x -direction and y -direction are $\rho L_2 L_3 x^2 (d^2 \lambda_1 / dt^2)$ and $\rho L_1 L_3 y^2 (d^2 \lambda_2 / dt^2)$, respectively [19]. The damping forces along the x -direction and y -direction are $c x d \lambda_1 / dt$ and $c y d \lambda_2 / dt$, respectively, which are linear with respect to the deformation velocity in these directions, where ρ is the density of the elastomer and c is the damping coefficient [20]. By its displacement derivative along the x -direction and y -direction, it is not difficult to obtain the inertial force does work and the damping force does work as

$$\begin{aligned} \rho L_2 L_3 \frac{d^2 \lambda_1}{dt^2} \delta \lambda_1 \int_0^{L_1} x^2 dx &= \frac{L_1^3 \rho L_2 L_3}{3} \frac{d^2 \lambda_1}{dt^2} \delta \lambda_1 \\ \rho L_1 L_3 \frac{d^2 \lambda_2}{dt^2} \delta \lambda_2 \int_0^{L_2} y^2 dy &= \frac{L_2^3 \rho L_1 L_3}{3} \frac{d^2 \lambda_2}{dt^2} \delta \lambda_2 \\ c \frac{d \lambda_1}{dt} \delta \lambda_1 \int_0^{L_1} x dx &= \frac{1}{2} c L_1^2 \delta \lambda_1 \frac{d \lambda_1}{dt} \\ c \frac{d \lambda_2}{dt} \delta \lambda_2 \int_0^{L_2} y dx &= \frac{1}{2} c L_2^2 \delta \lambda_2 \frac{d \lambda_2}{dt}. \end{aligned} \quad (3)$$

Thermodynamics requires that, for arbitrary variation of the system, the variation of the free energy of the membrane

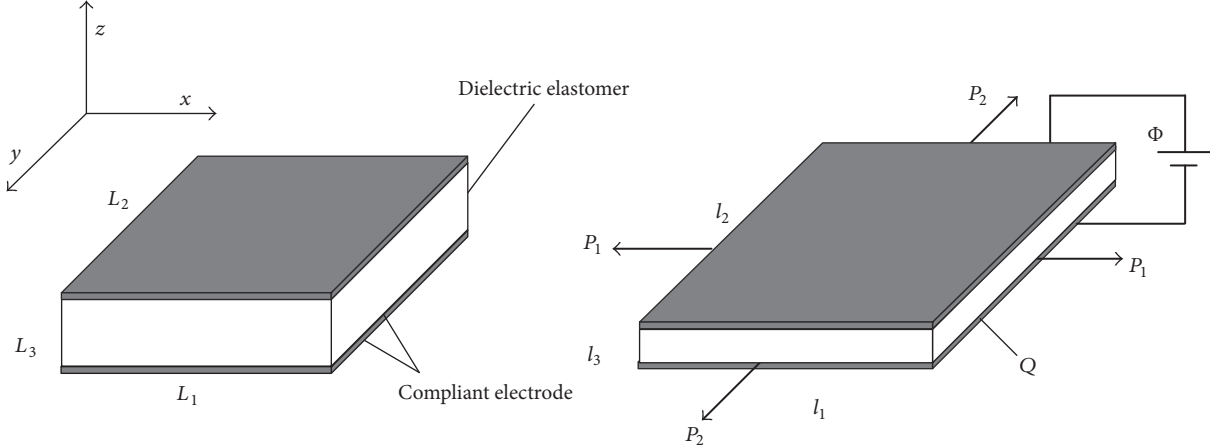


FIGURE 1: Schematics of a viscoelastic dielectric elastomer subject biaxial force in the plane and voltage through the thickness applied via stretchable electrodes.

should equal the work done by the voltage, the prestress, the inertia force, and the damping force; namely,

$$\begin{aligned} L_1 L_2 L_3 \delta W = & \Phi \delta Q + P_1 L_1 \delta \lambda_1 + P_2 L_2 \delta \lambda_2 \\ & - \frac{L_1^3 \rho L_2 L_3}{3} \frac{d^2 \lambda_1}{dt^2} \delta \lambda_1 \\ & - \frac{L_2^3 \rho L_1 L_3}{3} \frac{d^2 \lambda_2}{dt^2} \delta \lambda_2 - \frac{1}{2} c L_1^2 \delta \lambda_1 \frac{d \lambda_1}{dt} \\ & - \frac{1}{2} c L_2^2 \delta \lambda_2 \frac{d \lambda_2}{dt}. \end{aligned} \quad (4)$$

Experiments have verified that the electromechanical responses of DEs are highly rate-dependent, which implies that the deformation and actuation of DEs are highly relying on the rates of mechanical or electrical activation [9, 10]. This rate-dependence is mainly induced by the viscoelasticity of the elastomeric polymer matrix and may consequently influence the electromechanical actuation [27]. Viscoelastic relaxation may be represented by a rheological model of springs and dashpots [34–36]. As the DE exhibits elastic deformation and inelastic deformation, the latter of which is time-dependent, we first model this material by assuming that it is composed of two molecular chain networks, A and B, as sketched in Figure 2. The network A is an ideal hyperelastic chain and deforms reversibly, while the network B relaxes in time and dissipates energy. The viscous deformation is represented by a dashpot.

For the network represented by the spring and the dashpot at the bottom, the stretches (λ_1, λ_2) are due to both the spring and the dashpot; we adopt the well-established multiplication rule that [35–37]

$$\begin{aligned} \lambda_1 &= \lambda_1^e \xi_1, \\ \lambda_2 &= \lambda_2^e \xi_2, \end{aligned} \quad (5)$$

where $(\lambda_1^e, \lambda_2^e)$ are the stretches due to the bottom spring and (ξ_1, ξ_2) are stretches due to the dashpot.

To account for the effect of strain-stiffening, we represent both springs by using the Gent model [36–38]. The free-energy function of the elastomer is the sum of the contributions from the two springs and can be written as

$$\begin{aligned} W = & - \frac{\mu^A J^A}{2} \ln \left(1 - \frac{\lambda_1^2 + \lambda_2^2 + \lambda_1^{-2} \lambda_2^{-2} - 3}{J^A} \right) \\ & - \frac{\mu^B J^B}{2} \ln \left(1 - \frac{\lambda_1^2 \xi_1^{-2} + \lambda_2^2 \xi_2^{-2} + \lambda_1^{-2} \lambda_2^{-2} \xi_1^2 \xi_2^2 - 3}{J^B} \right) \\ & + \frac{\varepsilon}{2} \left(\frac{\Phi}{L_3} \right)^2 \lambda_1^2 \lambda_2^2, \end{aligned} \quad (6)$$

where μ^A and μ^B are the shear moduli of the two springs and J^A and J^B are the extension limits.

A combination of (2) and (4) gives that

$$\begin{aligned} L_1 L_2 L_3 \delta W = & \Phi^2 \frac{\varepsilon L_1 L_2}{L_3} (2 \lambda_1 \lambda_2^2 \delta \lambda_1 + 2 \lambda_1^2 \lambda_2 \delta \lambda_2) \\ & + \Phi \frac{\varepsilon L_1 L_2}{L_3} \lambda_1^2 \lambda_2^2 \delta \Phi + P_1 L_1 \delta \lambda_1 \\ & + P_2 L_2 \delta \lambda_2 - \frac{L_1^3 \rho L_2 L_3}{3} \frac{d^2 \lambda_1}{dt^2} \delta \lambda_1 \\ & - \frac{L_2^3 \rho L_1 L_3}{3} \frac{d^2 \lambda_2}{dt^2} \delta \lambda_2 - \frac{1}{2} c L_1^2 \delta \lambda_1 \frac{d \lambda_1}{dt} \\ & - \frac{1}{2} c L_2^2 \delta \lambda_2 \frac{d \lambda_2}{dt}. \end{aligned} \quad (7)$$

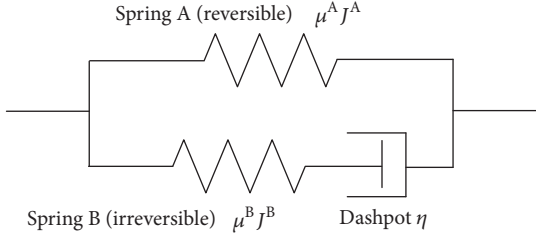


FIGURE 2: A Schematic illustration of a viscoelastic model for dielectric elastomer. It consists of two parallel elements: one element is a spring A and the other is a spring B which connected a dashpot in series.

We assume that the system is in mechanical and electrostatic equilibrium, and we obtain from the standard calculus of variation in (7) that

$$\frac{\partial W}{\partial \lambda_1} = 2\varepsilon \left(\frac{\Phi}{L_3} \right)^2 \lambda_1 \lambda_2^2 + \frac{P_1}{L_2 L_3} - \frac{L_1^2 \rho}{3} \frac{d^2 \lambda_1}{dt^2} - \frac{1}{2} \frac{c L_1}{L_2 L_3} \frac{d \lambda_1}{dt}, \quad (8)$$

$$\frac{\partial W}{\partial \lambda_2} = 2\varepsilon \left(\frac{\Phi}{L_3} \right)^2 \lambda_1^2 \lambda_2 + \frac{P_2}{L_1 L_3} - \frac{L_2^2 \rho}{3} \frac{d^2 \lambda_2}{dt^2} - \frac{1}{2} \frac{c L_2}{L_1 L_3} \frac{d \lambda_2}{dt}, \quad (9)$$

$$\tilde{D} = \frac{\partial W}{\partial \tilde{E}} = \Phi \frac{\varepsilon}{L_3} \lambda_1^2 \lambda_2^2 = \varepsilon \tilde{E} \lambda_1^2 \lambda_2^2. \quad (10)$$

Inserting (6) into (8) and (9), we obtain that

$$\begin{aligned} & \frac{L_1^2 \rho}{3} \frac{d^2 \lambda_1}{dt^2} + \frac{\mu^A (\lambda_1 - \lambda_1^{-3} \lambda_2^{-2})}{1 - (\lambda_1^2 + \lambda_2^2 + \lambda_1^{-2} \lambda_2^{-2} - 3) / J^A} \\ & + \frac{\mu^B (\lambda_1 \xi_1^{-2} - \lambda_1^{-3} \lambda_2^{-2} \xi_1^2 \xi_2^2)}{1 - (\lambda_1^2 \xi_1^{-2} + \lambda_2^2 \xi_2^{-2} + \lambda_1^{-2} \lambda_2^{-2} \xi_1^2 \xi_2^2 - 3) / J^B} \\ & - \varepsilon \left(\frac{\Phi}{L_3} \right)^2 \lambda_1 \lambda_2^2 - \frac{P_1}{L_2 L_3} + \frac{1}{2} \frac{c L_1}{L_2 L_3} \frac{d \lambda_1}{dt} = 0, \\ & \frac{L_2^2 \rho}{3} \frac{d^2 \lambda_2}{dt^2} + \frac{\mu^A (\lambda_2 - \lambda_1^{-2} \lambda_2^{-3})}{1 - (\lambda_1^2 + \lambda_2^2 + \lambda_1^{-2} \lambda_2^{-2} - 3) / J^A} \\ & + \frac{\mu^B (\lambda_2 \xi_2^{-2} - \lambda_1^{-2} \lambda_2^{-3} \xi_1^2 \xi_2^2)}{1 - (\lambda_1^2 \xi_1^{-2} + \lambda_2^2 \xi_2^{-2} + \lambda_1^{-2} \lambda_2^{-2} \xi_1^2 \xi_2^2 - 3) / J^B} \\ & - \varepsilon \left(\frac{\Phi}{L_3} \right)^2 \lambda_1^2 \lambda_2 - \frac{P_2}{L_1 L_3} + \frac{1}{2} \frac{c L_2}{L_1 L_3} \frac{d \lambda_2}{dt} = 0. \end{aligned} \quad (11)$$

To simplify mathematical expressions, we introduce the following dimensionless field variables $s_1 = P_1/(L_2 L_3 \mu)$, $\bar{E} = \Phi/(L_3 \sqrt{\varepsilon/\mu}) = \tilde{E}/\sqrt{\varepsilon/\mu}$, $s_1 = P_2/(L_1 L_3 \mu)$, and $\bar{D} = Q/(L_1 L_2 \sqrt{\varepsilon \mu}) = \tilde{D}/\sqrt{\varepsilon \mu}$.

While the method described here is applicable to general cases, in the following discussion, we will look at a special case when the dielectric film is under equibiaxial stress, such that $L_1 = L_2 = L$, $\lambda_1 = \lambda_2 = \lambda$, $\xi_1 = \xi_2 = \xi$, and $s_1 = s_2 = s$. The symmetry of the problem reduces the governing equations (11) to

$$\begin{aligned} & \frac{\rho L^2}{3\mu} \frac{d^2 \lambda}{dt^2} + \frac{\chi (\lambda - \lambda^{-5})}{1 - (2\lambda^2 + \lambda^{-4} - 3) / J^A} \\ & + \frac{(1 - \chi) (\lambda \xi^{-2} - \lambda^{-5} \xi^4)}{1 - (2\lambda^2 \xi^{-2} + \lambda^4 \xi^4 - 3) / J^B} - \frac{\varepsilon}{\mu} \left(\frac{\Phi}{L_3} \right)^2 \lambda^3 \\ & - s + \frac{1}{2} \frac{c}{\mu L_3} \frac{d \lambda}{dT} = 0, \end{aligned} \quad (12)$$

where $\mu = \mu^A + \mu^B$ and $\chi = \mu^A/\mu$ are the ratio between the equilibrium and instantaneous moduli. The rate of deformation in the dashpot is described by $\xi^{-1} d\xi/dt$. We relate the rate of deformation in the dashpot to the stress on the dashpot and write as [36]

$$\frac{d\xi}{dt} = \frac{\xi \mu^B}{6\eta} \frac{(\lambda^2 \xi^{-2} - \lambda^{-4} \xi^4)}{1 - (2\lambda^2 \xi^{-2} + \lambda^{-4} \xi^4 - 3) / J^B}, \quad (13)$$

where η is the viscosity of the dashpot.

We can see that the qualitative properties of the solutions of (12) and (13) depend on the applied loads and viscoelasticity. Equations (12) and (13) give the equations of motion for a viscoelastic DE, which we use in the following analysis to study the quasistatic response and the dynamic characteristics of a viscoelastic DE.

3. Simulation Results and Discussion

3.1. Quasistatic Response. When the stress s and voltage Φ are quasistatic, the membrane may reach a state of equilibrium. In this case, both the inertial force and the viscous force are zero; in the state of equilibrium, the equation of motion (12) can be expressed as

$$\begin{aligned} & \frac{\chi (\lambda - \lambda^{-5})}{1 - (2\lambda^2 + \lambda^{-4} - 3) / J^A} \\ & + \frac{(1 - \chi) (\lambda \xi^{-2} - \lambda^{-5} \xi^4)}{1 - (2\lambda^2 \xi^{-2} + \lambda^4 \xi^4 - 3) / J^B} - \bar{E}^2 \lambda^3 - s = 0. \end{aligned} \quad (14)$$

The inelastic deformation of the material evolves with relaxation time η/μ^B . Here we will use it to normalize time t by introducing a dimensionless time, $\tau = t \mu^B / \eta$. Using the dimensionless time, we write the kinetic equation (13) as

$$\begin{aligned} & \frac{\chi (\lambda - \lambda^{-5})}{1 - (2\lambda^2 + \lambda^{-4} - 3) / J^A} \\ & + \frac{(1 - \chi) (\lambda \xi^{-2} - \lambda^{-5} \xi^4)}{1 - (2\lambda^2 \xi^{-2} + \lambda^4 \xi^4 - 3) / J^B} - \bar{E}^2 \lambda^3 - s = 0. \end{aligned} \quad (15)$$

In the following analysis, we take $J^A = 110 \text{ kPa}$, $J^B = 55 \text{ kPa}$, $\chi = 0.5$ [36] as representative values for the most widely used DE.

When the viscoelastic DE actuator subject to a cyclic electric load, $\bar{E} = \bar{E}_0 \sin(\omega\tau)$, but not to forces $s = 0$, with $\bar{E}_0 = 0.5$ to avoid instantaneous instability within the selected frequency range and with ω being the dimensionless frequency, the total stretch λ and the inelastic stretch ξ can be easily evolved by solving (14) and (15). The voltage is applied at time $\tau = 0$. The dashpot does not move instantaneously, so that the initial value of the internal variable is $\lambda = \xi = 1$. The time-dependent stretch, nominal electric field-stretch, and nominal electric field-nominal electric displacement curves of representative applied voltage frequency are presented in Figure 3.

It can be seen that, at a relatively high frequency ($\omega = 10$) of the applied electric field, the deformation of the viscoelastic DE could keep in phase with the electric field, as shown in Figure 3(a), but the actuation strain (λ) is relatively small (shown with solid curves in Figure 3(a)). This is because that the voltage was varied on a time-scale much faster than the viscoelastic relaxation time. Subjecting to a cyclic load, as the actuation stretch only depends on the magnitude of the applied voltage, the frequency of the stretch doubles that of the electric field in Figure 3(a), and the mean value of stretch may drift away from the initial equilibrium state. The nominal electric field-stretch response ($\bar{E} - \lambda$) in Figure 3(b) and the nominal electric field-nominal electric displacement response ($\bar{E} - \bar{D}$) in Figure 3(c) show no clear limit cycle, indicating that there will be insignificant hysteresis in the viscoelastic DE for high frequency.

When the frequency of the applied electric field decreases to an intermediate frequency, for example, $\omega = 0.1$, the magnitude of the actuation strain (λ) becomes much larger, and the amplitude of the inelastic stretch is almost the same as that of λ , showing almost fully inelastic deformation. Limit cycles appear on $\bar{E} - \lambda$ and $\bar{E} - \bar{D}$ plots in Figures 3(e) and 3(f). Both plots show hysteresis which indicate that significant amount of energy is dissipated during the electromechanical conversion process.

When the DE is actuated by a relatively low frequency voltage for $\omega = 0.034$, the magnitude of both the actuation stretch and the inelastic stretch attains peak values and there will be most dissipative energy during this cycle, as shown in Figures 3(g), 3(h), and 3(i). The main reason is the geometric nonlinearity introduced by the finite viscoelastic deformation in (14) and (15) according to Hong [34]. When the input electric field is sinusoidal, the output total stretch (λ) and the inelastic stretch (ξ) are not sinusoidal any more. The reason is that the thermoelectromechanically system under a cycle electric load is highly nonlinear and the asymmetry in the shape of the output cyclic deformation $\lambda(\tau)$ at low frequency would lead to significant irreversible energy loss of the system.

However, when the frequency decrease to a critical value, for $\omega \leq 0.033$, the viscoelastic DE will suffer the pull-in instability a little while as plotted in Figures 3(j), 3(k), and 3(l), the instability is marked with “ \times .” When the voltage is

applied at a relatively low frequency, the major part of the total deformation is inelastic as shown in Figure 3(j). This result agrees well with experimental observations [9] that the DE more often suffers the pull-in instability at low stretch rates when inelastic deformation is significant.

3.2. Dynamic Response. When the DE with stretching deformation oscillates under cycle voltage, the inertia force will contribute to the electromechanical performance. In the following, numerical simulation results of the model are presented to show the vibration and oscillation behavior of the viscoelastic DE.

Here we will use the normalized time t by introducing the dimensionless time $\tilde{t} = t/(L\sqrt{\rho/3\mu})$, $\tilde{c} = c/(2\mu L_3 L\sqrt{\rho/3\mu})$ and dimensionless relaxation time $\tilde{\tau} = (\eta/\mu^B)/(L\sqrt{\rho/3\mu})$, and we may reduce (12) and (13) to the following form:

$$\begin{aligned} & \frac{d^2\lambda}{d\tilde{t}^2} + \frac{\chi(\lambda - \lambda^{-5})}{1 - (2\lambda^2 + \lambda^{-4} - 3)/J^A} \\ & + \frac{(1 - \chi)(\lambda\xi^{-2} - \lambda^{-5}\xi^4)}{1 - (2\lambda^2\xi^{-2} + \lambda^4\xi^4 - 3)/J^B} - \bar{E}^2\lambda^3 - s \\ & + \tilde{c}\frac{d\lambda}{dT} = 0, \\ & \frac{d\xi}{d\tilde{t}} = \frac{1}{6\tilde{\tau}} \frac{\xi(\lambda^2\xi^{-2} - \lambda^{-4}\xi^4)}{1 - (2\lambda^2\xi^{-2} + \lambda^{-4}\xi^4 - 3)/J^B}. \end{aligned} \quad (16)$$

To be specific, the following parameters are used in the dynamic examples: $J^A = 110 \text{ KPa}$, $J^B = 55 \text{ KPa}$, $\chi = 0.5$, $\tilde{\tau} = 1$, and $\tilde{c} = 1$ [20, 34–36].

The cyclic electric load, $\bar{E} = \bar{E}_0 \sin(\Omega\tilde{t})$, is applied at time $\tilde{t} = 0$, with $\bar{E}_0 = 0.5$ to avoid instantaneous instability within the selected frequency range and with Ω being the dimensionless frequency. The dashpot does not move instantaneously, so that the initial value of the internal variable is $\lambda(0) = \xi(0) = 1$ and $\dot{\lambda}(0) = 0$. Under these assumptions, when no prestress is applied, $s = 0$, by solving the governing equations (16), the dynamic stability evolution and performance of the viscoelastic elastomer, such as the oscillation diagram, the hysteresis loop, the phase diagram, and the Poincaré map, are simulated.

Due to nonlinearity of the system, the dynamic response of the viscoelastic elastomer under time-dependent electric load can be very complicated. When the representative dimensionless frequency varies from 0 to 10, the viscoelastic DE presents oscillations with varying amplitudes shown in Figures 4–7.

It can be seen that voltage applied at a relative high frequency ($\Omega = 10$) gives a relative small total stretch (λ) and viscous stretch (ξ) in Figure 4(a). At the same time, the nominal electric field-stretch response ($\bar{E} - \lambda$) in Figure 4(b) and the nominal electric field-nominal electric displacement response ($\bar{E} - \bar{D}$) in Figure 4(c) show no clear limit cycle, indicating that there will be insignificant hysteresis in the

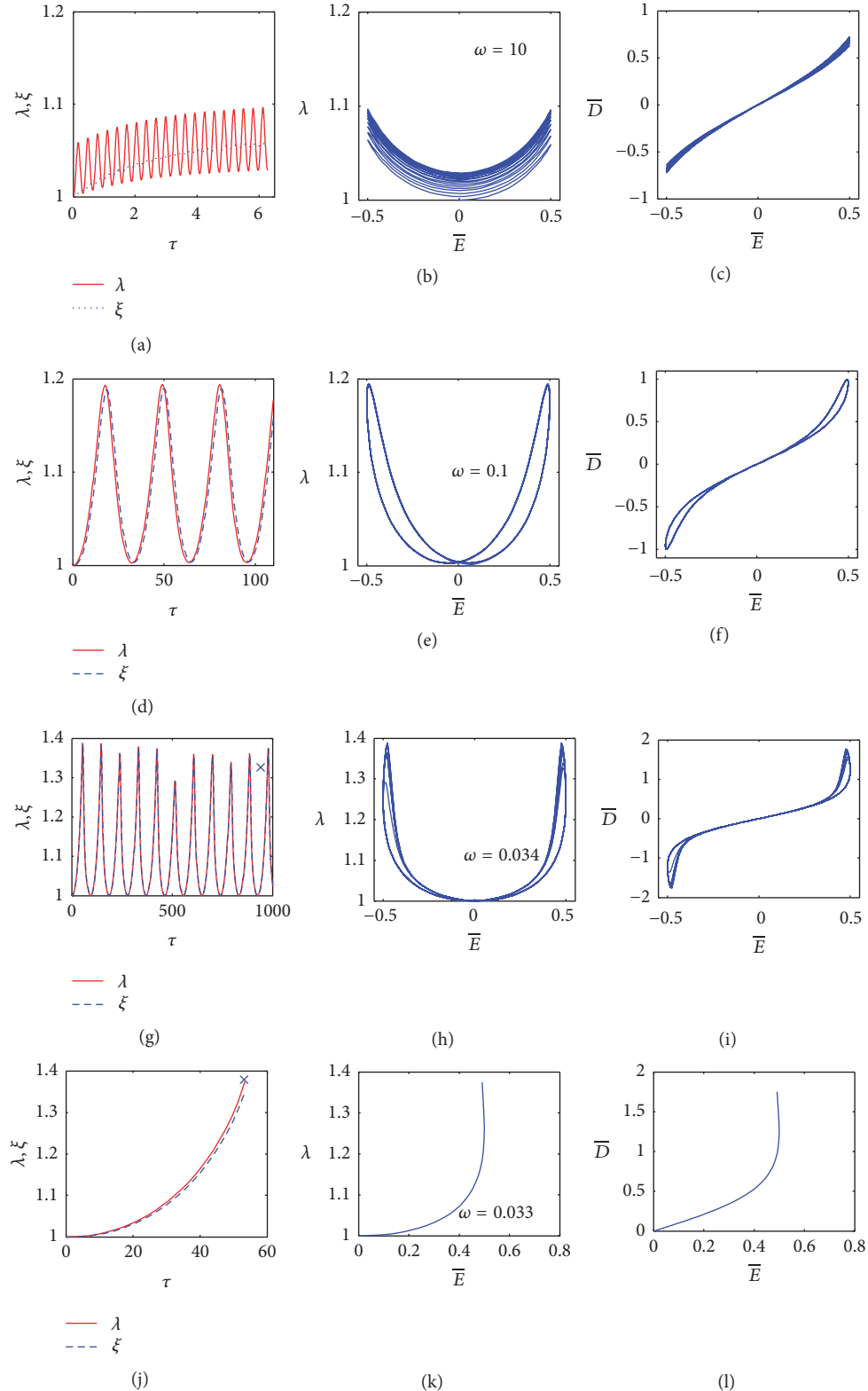


FIGURE 3: A membrane is subject to the applied cyclic nominal electric field. (a), (d), (g), and (j) are the calculated time-dependent total stretch and inelastic stretch. (b), (e), (h), and (k) are the stretch-electric field response. (c), (f), (i), and (l) are the dimensionless nominal electric displacement-nominal electric field curves. Four different dimensionless frequencies are used in the calculation with $\omega = 10$ for (a), (b), and (c), $\omega = 1$ for (d), (e), and (f), $\omega = 0.034$ for (g), (h), and (i), $\omega = 0.033$ for (j), (k), and (l).

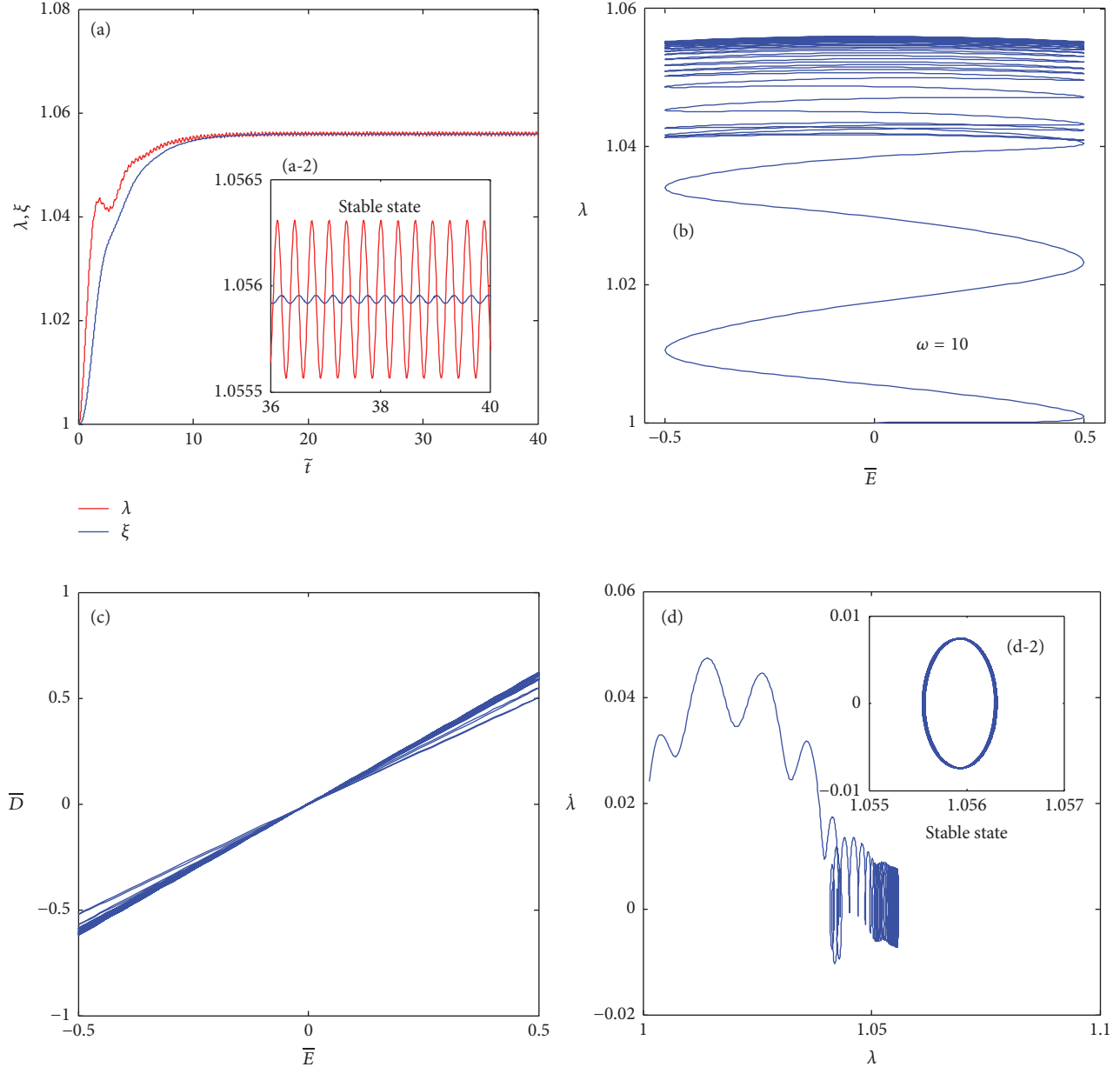


FIGURE 4: The total stretch λ the viscous stretch ξ (a), the nominal electric field-stretch response (b), the nominal electric field-nominal electric displacement (c), and the phase diagram (d) for the dimensionless frequency $\Omega = 10$.

viscoelastic DE for high frequency. The phase diagram in Figure 4(d) is not closed for $\Omega = 10$ at the outset, emerging as a tangle of interlaced curves, which means that the system is aperiodic and unstable. However, the phase diagram in Figure 4(d-2) forms a closed loop after few cycles, implying a quasiperiodic vibration. The amplitude of the stretch λ is extremely small; in other words, the quasiperiodic vibration is almost static.

Figure 5(a) shows the time-dependent behavior of the total stretch and the viscous stretch for $\Omega = 11$. The stretch increases and stabilizes after few cycles. $\bar{E} - \lambda$, $\bar{E} - \bar{D}$ response and the phase diagram are plotted in Figures 5(b), 5(c), and 5(d). As can be seen from Figures 5(b) and 5(c), the hysteresis loop can be observed, indicating dissipation of

energy. The phase paths in Figure 5(d) are presented in a closed loop when the system has achieved stable vibration after few cycles; this result shows that the system undergoes a nonlinear quasiperiodic oscillation.

The dynamic behaviors of the viscoelastic DE for $\Omega = 0.1$ are shown in Figure 6. When the DE is actuated by a relatively low frequency voltage for $\Omega = 0.1$, the magnitude of the total stretch and the viscous stretch are both much larger and there will be significant dissipative energy during this cycle, as shown in Figures 6(a), 6(b), and 6(c), which is similar to the quasistatic response. The phase diagram is closed, indicating a steady state of oscillation, as indicated in Figure 6(d).

In addition, the critical value for the frequency to suppress the pull-in instability can be observed by solving (16).

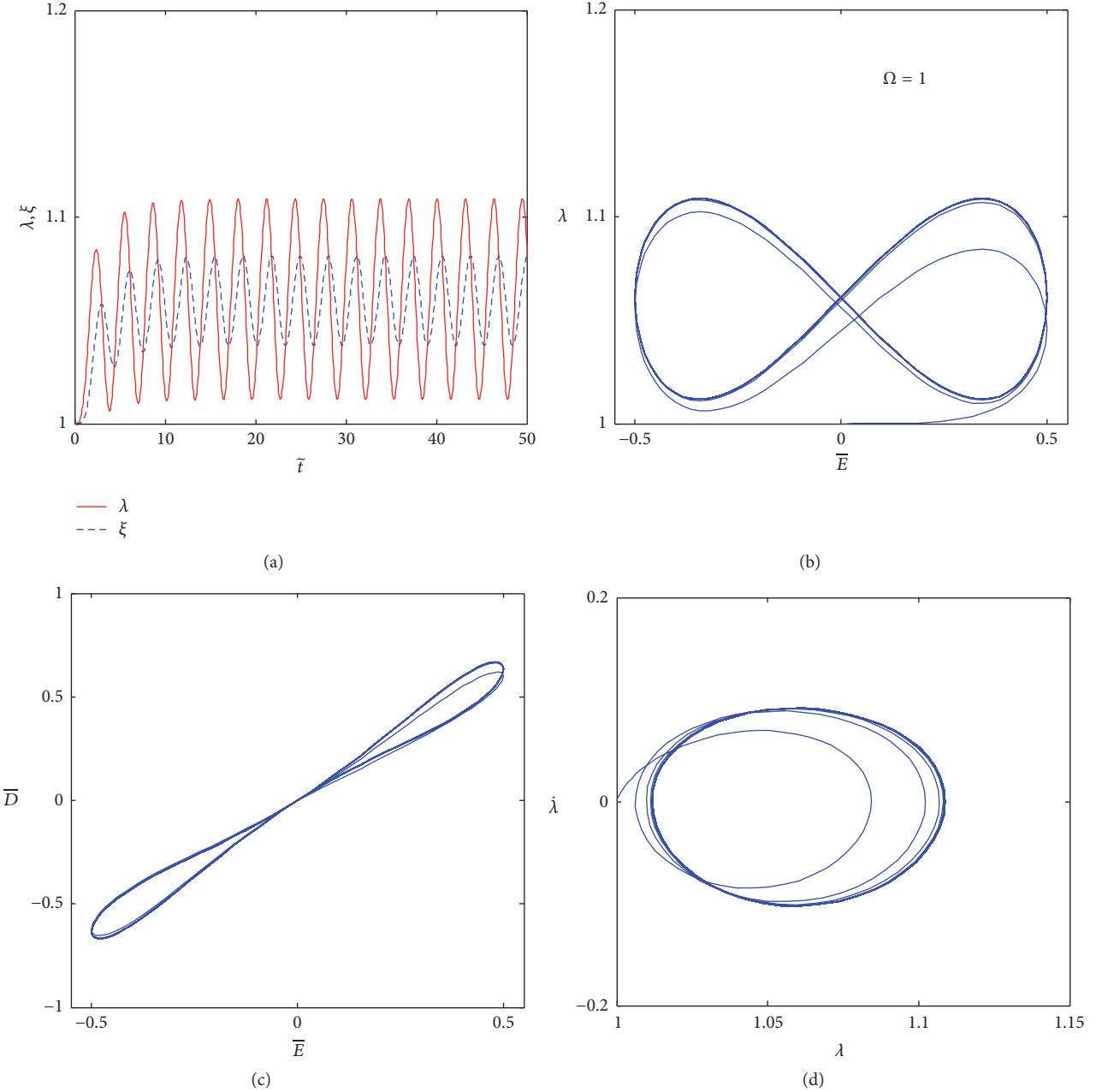


FIGURE 5: The total stretch λ , the viscous stretch ξ (a), the nominal electric field-stretch response (b), the nominal electric field-nominal electric displacement (c), and the phase diagram (d) for the dimensionless frequency $\Omega = 1$.

The critical value of the frequency is 0.0213. The dynamic performances of the viscoelastic dielectric elastomer for very low frequency, $\Omega = 0.0213$, are plotted in Figure 7. It can be seen that the stretch attains a maximum value which is about 1.5 than the critical value of quasistatic response. What is more, the hysteresis loop in the \bar{E} – λ and \bar{E} – \bar{D} plots becomes much bigger as compared with the high frequency in Figures 4–6 and the quasistatic response in Figure 3. That is to say, the dissipation of energy in the dynamic response is bigger than the quasistatic response. The reason is that the dynamic response of DE system under a cycle electric load is highly nonlinear and the asymmetry in the shape of the

output cyclic deformation $\lambda(\tilde{t})$ at low frequency for dynamic oscillation, and the nonlinear and asymmetry become more and more obviously, which would lead to more significant irreversible energy loss of the system in dynamic response. When the applied voltage frequency decrease to the critical value, for $\Omega \leq 0.0213$, the viscoelastic DE will suffer the pull-in instability after a certain time.

Poincaré map can be used to detect the stability transition of the system [20, 23, 28]. The Poincaré maps for the oscillation with the frequency $\Omega = 10, 1, 0.1$, and 0.0213 are shown in Figure 8. It can be concluded that there exists strange attractor in the Poincaré map for the oscillation with

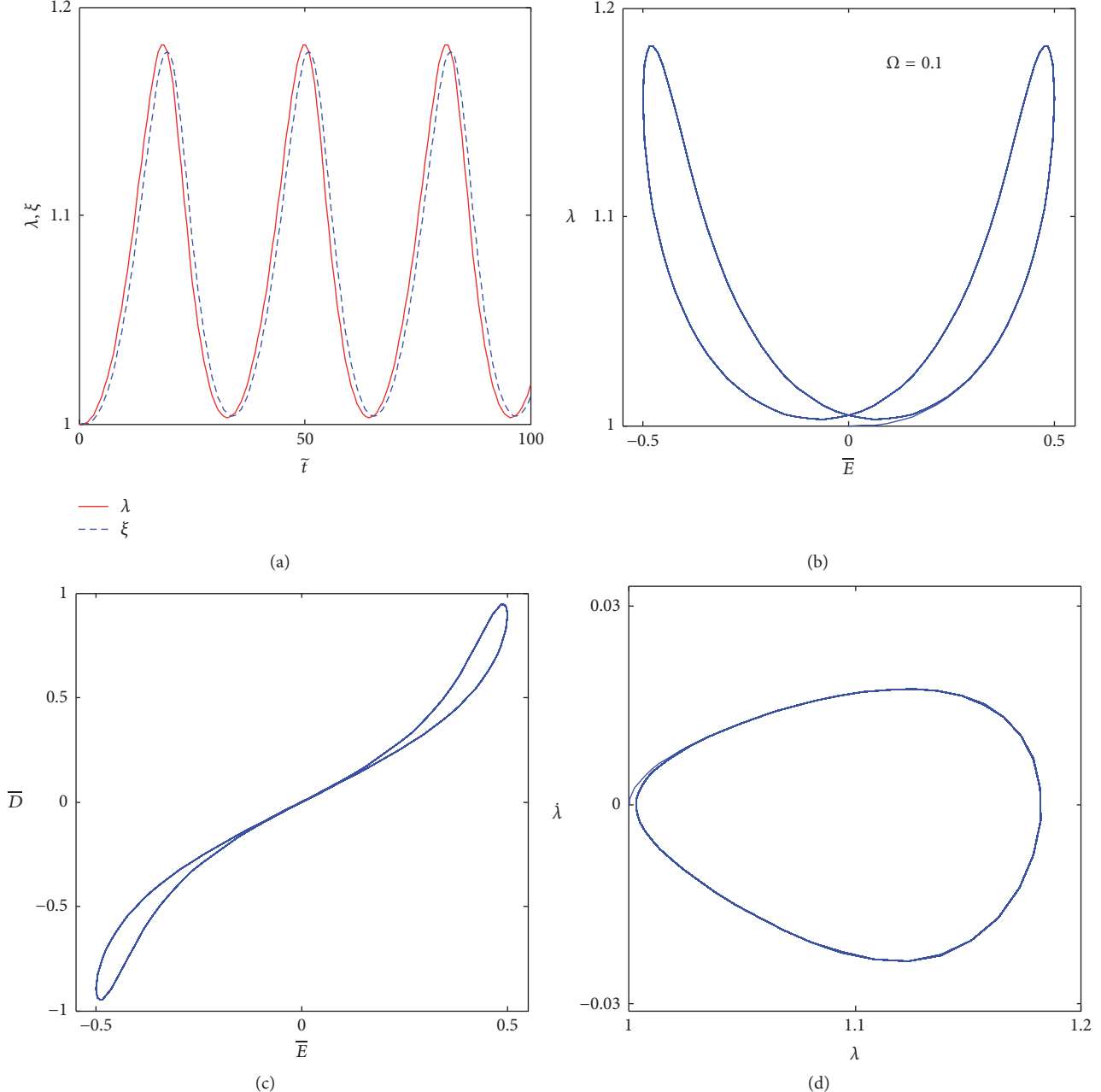


FIGURE 6: The total stretch λ , the viscous stretch ξ (a), the nominal electric field-stretch response (b), the nominal electric field-nominal electric displacement (c), and the phase diagram (d) for the dimensionless frequency $\Omega = 0.1$.

the frequency $\Omega = 10$ in Figure 8(a) for the initiate cycles, which is the representative of an aperiodic vibration motion; with the creep of time, the oscillation of DE the Poincaré map at the frequency of $\Omega = 10$ in Figure 8(a-2) shows one point, indicating single cycle oscillation. That is, the DE experiences a dynamic stability evolution from an aperiodic motion to the quasiperiodic motion for a relative high frequency. With the frequency decreasing, the Poincaré maps at the frequency of $\Omega = 1, 0.1$, and 0.0213 all have finite points, which mean that the motions are quasiperiodic and stable. As shown in Figure 8(b), the motion of DE at $\Omega = 1$ have two periods

at least, compared to single cycle motion for frequencies 0.1 (Figure 8(c)) and 0.213 (Figure 8(d)).

3.3. Effect of Relaxation Time. What is more, the viscoelastic relaxation time of VHB ranges from hundreds of microseconds to hundreds of seconds [39, 40] and affects the creeping deformation ξ of DE; that is, the enhancement of the pre-stretch (prestretch provides advantages to the electromechanical actuation to improve the electrical breakdown strength, avoiding instability and reducing the geometric thickness) followed by short relaxation approximately doubles that of

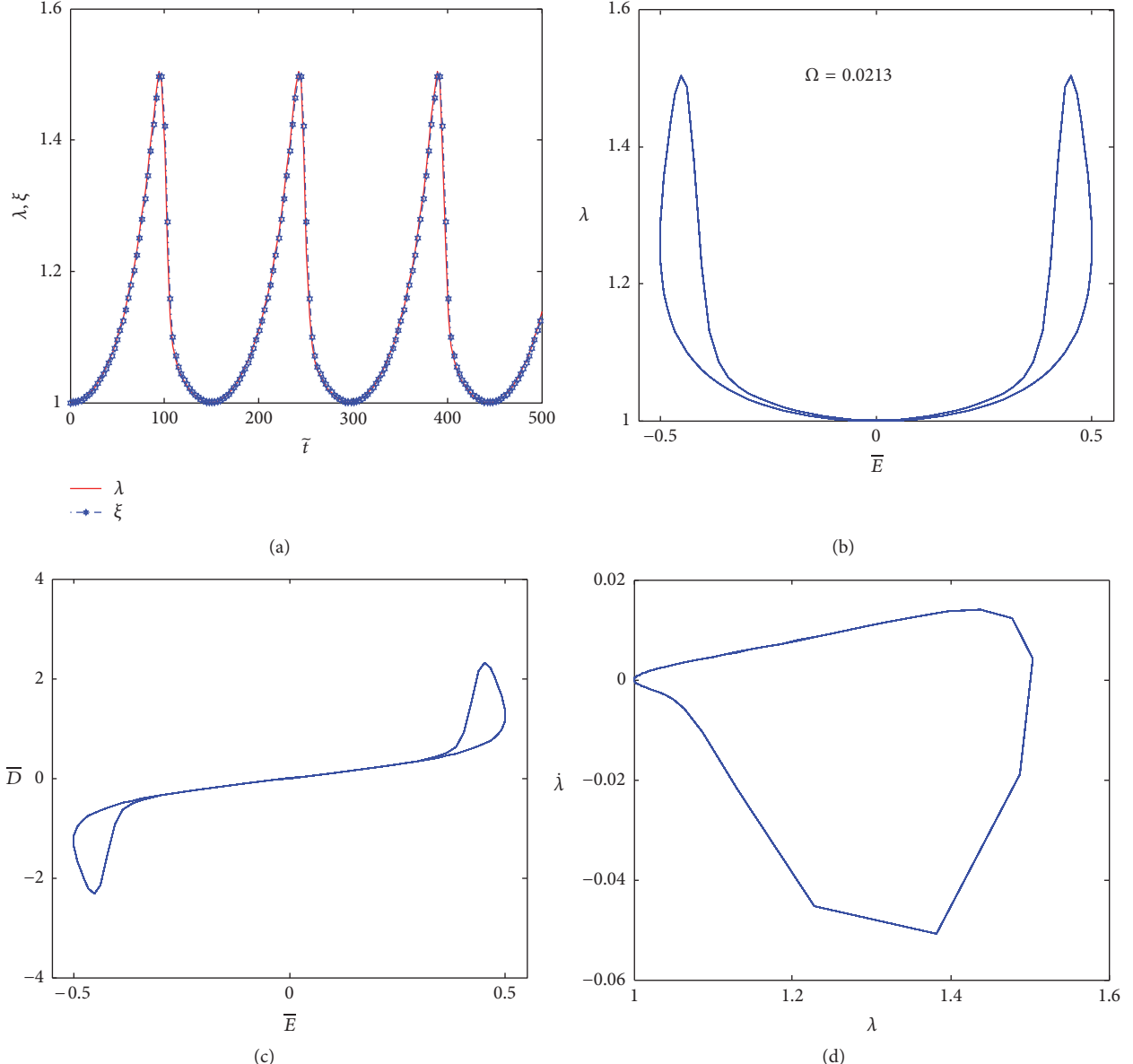


FIGURE 7: The total stretch λ , the viscous stretch ξ (a), the nominal electric field-stretch response (b), the nominal electric field-nominal electric displacement (c), and the phase diagram (d) for the dimensionless frequency $\Omega = 0.0213$.

the same prestretch but with long relaxation [9, 34]. However, the relaxation time effects are seldom analyzed in the scope of viscoelasticity. When no prestress is applied $s = 0$, we solve (16) under three levels of dimensionless viscoelastic relaxation time at the dimensionless frequency of $\Omega = 1$, with $\tilde{\tau} = 1, 10$, and 100 , and plot the solution in Figure 9.

The oscillation of stretch λ exhibits a strong nonlinearity with the coupled effects of relaxation times and frequencies. For a relative high relaxation time of $\tilde{\tau} = 10$ in Figure 9(d), the stretch creeps with time and requires longer time to achieve a stable motion. For a higher relaxation time of $\tilde{\tau} = 100$, the stretch of λ will drift to a larger value at the stable state of oscillation after many cycles as shown in Figure 9(g-2).

It can also be observed that the creeping value of viscous stretch (ξ) reduces gradually with the increasing value of relaxation times (Figures 9(a), 9(d), and 9(g)), and the creep can be almost eliminated in Figure 9(g) when suitable values of relaxation times are applied. When the relaxation time increases, the viscous stretch becomes smaller, that is, because the viscoelastic deformation of the DE fails to keep up with electric field frequency leading to decreasing the viscous stretch.

As illustrated in Figure 9, the λ - $\dot{\lambda}$ phase diagrams (Figures 9(b), 9(e), and 9(h)) are all presented in closed regions indicating that DE system experiences a nonlinear quasiperiodic oscillation and the dynamic oscillation of the DE system is stable. When the relaxation time increases from $\tilde{\tau} = 1$ to

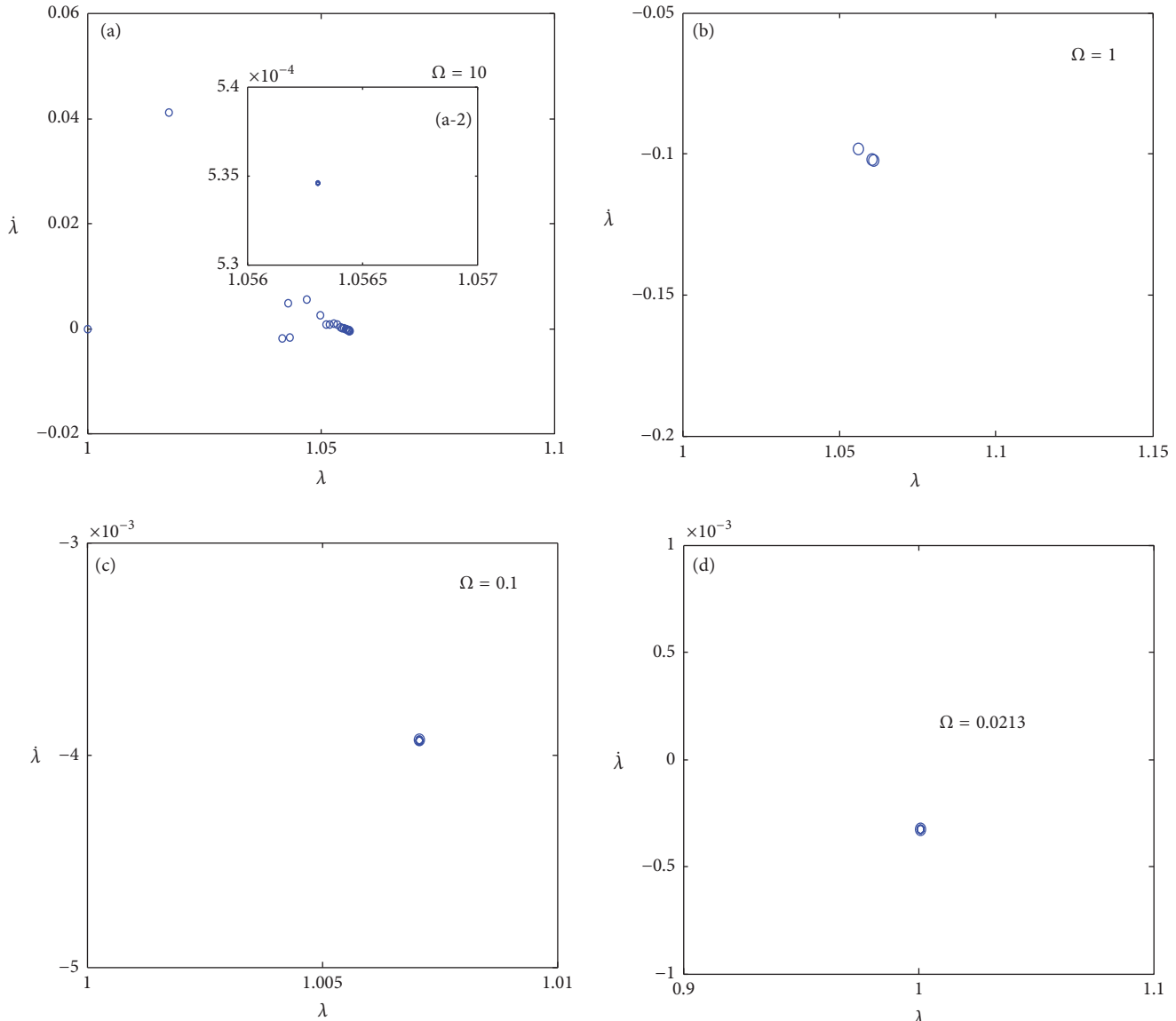


FIGURE 8: Poincaré map for the oscillation under a cyclic electric load with different dimensionless frequencies (a) $\Omega = 10$, (b) $\Omega = 1$, (c) $\Omega = 0.1$, and (d) $\Omega = 0.0213$.

$\tilde{\tau} = 100$, the Poincaré maps (Figures 9(c), 9(f), and 9(i)) all show finite points with 2, 3, and 8, respectively. That is to say, the DE system may experience a stability evolution from a single cycle motion to multicycle motion with the increasing relaxation times for a fixed frequency.

4. Conclusions

Although the dynamics of DE are widely studied recently, this study gives a further understanding of the effect of viscoelasticity and frequency on dynamic response of DE and can help to guide the design of dynamic and static applications in DE actuators.

The dynamic behavior of a viscoelastic DE under a cyclic electric field is presented to compare with the quasistatic

behavior. The time-dependent dynamic deformation, the hysteresis process, and the dynamic stability undergoing viscoelastic dissipative processes are investigated by using the theory of nonequilibrium thermodynamics. The results show that when the frequency of the applied voltage decreases, whether the quasistatic or the dynamic performance, the total stretch and the viscous stretch both become larger. In addition, the energy dissipated per cycle increases with the decreasing frequency and there exists a critical value of the frequency at which the pull-in instability takes place. When the applied voltage frequency is below a critical value, the viscoelastic DE cannot attain a steady state of oscillation and may have instability. The system of the viscoelastic DE also presents stability transition from an aperiodic motion to the quasiperiodic motion for a relative high frequency and experiences a stability evolution from single cycle motion to

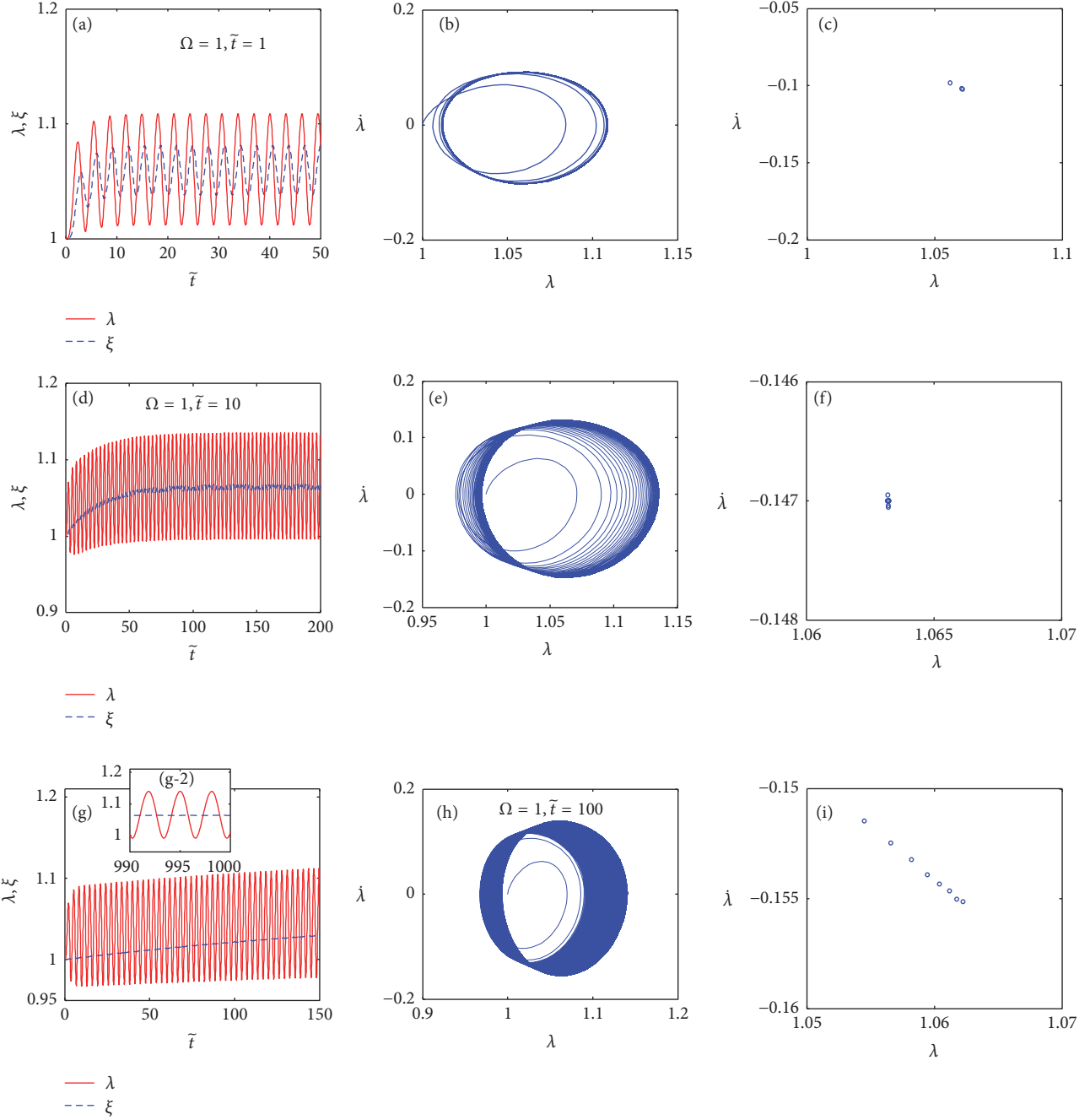


FIGURE 9: The total stretches λ , the viscous stretches ξ ((a), (d), and (g)), the phase diagrams ((c), (e), and (h)), and the Poincaré maps ((c), (f), and (i)) at dimensionless frequency of $\Omega = 1$ for different dimensionless relaxation times $\tilde{t} = 1, 10$, and 100 .

multicycle motion with the increasing relaxation times for a fixed frequency. The creeping value of viscous stretch of the dashpot reduces gradually with the increasing value of relaxation times and the creep can be almost eliminated at a suitable value of relaxation time.

Conflicts of Interest

The authors declare that they have no conflicts of interest.

Acknowledgments

This research was supported by the National Natural Science Foundation of China (Grant no. 11402246). The authors gratefully acknowledge these supports.

References

- [1] J. W. Kwak, H. J. Chi, K. M. Jung et al., "A face robot actuated with artificial muscle based on dielectric elastomer," *Journal of*

- Mechanical Science and Technology*, vol. 19, no. 2, pp. 578–588, 2005.
- [2] G. Kovacs, L. Düring, S. Michel, and G. Terrasi, “Stacked dielectric elastomer actuator for tensile force transmission,” *Sensors and Actuators A: Physical*, vol. 155, no. 2, pp. 299–307, 2009.
- [3] C. Keplinger, M. Kaltenbrunner, N. Arnold, and S. Bauer, “Röntgen's electrode-free elastomer actuators without electromechanical pull-in instability,” *Proceedings of the National Academy of Sciences of the United States of America*, vol. 107, no. 10, pp. 4505–4510, 2010.
- [4] T. McKay, B. O'Brien, E. Calius, and I. Anderson, “Self-priming dielectric elastomer generators,” *Smart Materials and Structures*, vol. 19, no. 5, Article ID 055025, 2010.
- [5] F. Carpi, D. De Rossi, R. Kornbluh, R. Pelrine, and P. Sommer-Larsen, “Dielectric elastomers as electromechanical transducers: Fundamentals, Materials, Devices, Models and Applications of an Emerging Electroactive Polymer Technology,” *Dielectric Elastomers as Electromechanical Transducers*, p. 329, 2008.
- [6] P. Brochu and Q. Pei, “Advances in dielectric elastomers for actuators and artificial muscles,” *Macromolecular Rapid Communications*, vol. 31, no. 1, pp. 10–36, 2010.
- [7] R. K. Sahu, A. Saini, D. Ahmad, K. Patra, and J. Szpunar, “Estimation and validation of maxwell stress of planar dielectric elastomer actuators,” *Journal of Mechanical Science and Technology*, vol. 30, no. 1, pp. 429–436, 2016.
- [8] L. Liu, J. Li, Y. Liu, J. Leng, J. Zhao, and J. Zhao, “Electric field induced variation of temperature and entropy in dielectric elastomers,” *Journal of Mechanical Science and Technology*, vol. 29, no. 1, pp. 109–114, 2015.
- [9] J.-S. Plante and S. Dubowsky, “Large-scale failure modes of dielectric elastomer actuators,” *International Journal of Solids and Structures*, vol. 43, no. 25–26, pp. 7727–7751, 2006.
- [10] J.-S. Plante and S. Dubowsky, “On the performance mechanisms of Dielectric Elastomer Actuators,” *Sensors and Actuators A: Physical*, vol. 137, no. 1, pp. 96–109, 2007.
- [11] M. Molberg, Y. Leterrier, C. J. G. Plummer et al., “Frequency dependent dielectric and mechanical behavior of elastomers for actuator applications,” *Journal of Applied Physics*, vol. 106, no. 5, Article ID 054112, 2009.
- [12] F. Carpi, S. Bauer, and D. De Rossi, “Stretching dielectric elastomer performance,” *Science*, vol. 330, no. 6012, pp. 1759–1761, 2010.
- [13] P. Dubois, S. Rosset, M. Niklaus, M. Dadras, and H. Shea, “Voltage control of the resonance frequency of dielectric electroactive polymer (DEAP) membranes,” *Journal of Microelectromechanical Systems*, vol. 17, no. 5, pp. 1072–1081, 2008.
- [14] J. W. Fox and N. C. Goulbourne, “On the dynamic electromechanical loading of dielectric elastomer membranes,” *Journal of the Mechanics and Physics of Solids*, vol. 56, no. 8, pp. 2669–2686, 2008.
- [15] K. Hochradel, S. J. Rupitsch, A. Sutor, R. Lerch, D. K. Vu, and P. Steinmann, “Dynamic performance of dielectric elastomers utilized as acoustic actuators,” *Applied Physics A: Materials Science & Processing*, vol. 107, no. 3, pp. 531–538, 2012.
- [16] J. Zhu, S. Cai, and Z. Suo, “Nonlinear oscillation of a dielectric elastomer balloon,” *Polymer International*, vol. 59, no. 3, pp. 378–383, 2010.
- [17] J. Zhu, S. Cai, and Z. Suo, “Resonant behavior of a membrane of a dielectric elastomer,” *International Journal of Solids and Structures*, vol. 47, no. 24, pp. 3254–3262, 2010.
- [18] H. Yong, X. He, and Y. Zhou, “Dynamics of a thick-walled dielectric elastomer spherical shell,” *International Journal of Engineering Science*, vol. 49, no. 8, pp. 792–800, 2011.
- [19] T. Li, S. Qu, and W. Yang, “Electromechanical and dynamic analyses of tunable dielectric elastomer resonator,” *International Journal of Solids and Structures*, vol. 49, no. 26, pp. 3754–3761, 2012.
- [20] B.-X. Xu, R. Mueller, A. Theis, M. Klassen, and D. Gross, “Dynamic analysis of dielectric elastomer actuators,” *Applied Physics Letters*, vol. 100, no. 11, Article ID 112903, 2012.
- [21] K. Jia, T. Lu, and T. J. Wang, “Response time and dynamic range for a dielectric elastomer actuator,” *Sensors and Actuators A: Physical*, vol. 239, pp. 8–17, 2016.
- [22] B. Li, J. Zhang, L. Liu, H. Chen, S. Jia, and D. Li, “Modeling of dielectric elastomer as electromechanical resonator,” *Journal of Applied Physics*, vol. 116, no. 12, Article ID 124509, 2014.
- [23] J. Sheng, H. Chen, B. Li, and Y. Wang, “Nonlinear dynamic characteristics of a dielectric elastomer membrane undergoing in-plane deformation,” *Smart Materials and Structures*, vol. 23, no. 4, Article ID 045010, 2014.
- [24] F. Wang, T. Lu, and T. J. Wang, “Nonlinear vibration of dielectric elastomer incorporating strain stiffening,” *International Journal of Solids and Structures*, vol. 87, pp. 70–80, 2016.
- [25] A. York, J. Dunn, and S. Seelecke, “Experimental characterization of the hysteretic and rate-dependent electromechanical behavior of dielectric electro-active polymer actuators,” *Smart Materials and Structures*, vol. 19, no. 9, Article ID 094014, 2010.
- [26] P. Lochmatter, G. Kovacs, and M. Wissler, “Characterization of dielectric elastomer actuators based on a visco-hyperelastic film model,” *Smart Materials and Structures*, vol. 16, no. 2, article no. 028, pp. 477–486, 2007.
- [27] C. Keplinger, M. Kaltenbrunner, N. Arnold, and S. Bauer, “Capacitive extensometry for transient strain analysis of dielectric elastomer actuators,” *Applied Physics Letters*, vol. 92, no. 19, Article ID 192903, 2008.
- [28] J. Zhang, H. Chen, B. Li, D. McCoul, and Q. Pei, “Coupled nonlinear oscillation and stability evolution of viscoelastic dielectric elastomers,” *Soft Matter*, vol. 11, no. 38, pp. 7483–7493, 2015.
- [29] J. Zhang, L. Tang, B. Li, Y. Wang, and H. Chen, “Modeling of the dynamic characteristic of viscoelastic dielectric elastomer actuators subject to different conditions of mechanical load,” *Journal of Applied Physics*, vol. 117, no. 8, Article ID 084902, 2015.
- [30] J. Zhang, J. Zhao, H. Chen, and D. Li, “Dynamic analyses of viscoelastic dielectric elastomers incorporating viscous damping effect,” *Smart Materials & Structures*, vol. 26, no. 1, Article ID 015010, 2017.
- [31] Y. Wang, H. Xue, H. Chen, and J. Qiang, “A dynamic visco-hyperelastic model of dielectric elastomers and their energy dissipation characteristics,” *Applied Physics A: Materials Science & Processing*, vol. 112, no. 2, pp. 339–347, 2013.
- [32] C. Zhang, H. Chen, B. Li, Y. Wang, L. Liu, and D. Li, “Investigation on static and dynamic performance of a hinge configuration with integrated dielectric elastomers,” *Journal of Applied Polymer Science*, vol. 132, no. 11, p. 41630, 2015.
- [33] J. Sheng, H. Chen, L. Liu, J. Zhang, Y. Wang, and S. Jia, “Dynamic electromechanical performance of viscoelastic dielectric elastomers,” *Journal of Applied Physics*, vol. 114, no. 13, Article ID 134101, 2013.
- [34] W. Hong, “Modeling viscoelastic dielectrics,” *Journal of the Mechanics and Physics of Solids*, vol. 59, no. 3, pp. 637–650, 2011.

- [35] X. Zhao, S. J. A. Koh, and Z. Suo, "Nonequilibrium thermodynamics of dielectric elastomers," *International Journal of Applied Mechanics*, vol. 3, no. 2, pp. 203–217, 2011.
- [36] C. Chiang Foo, S. Cai, S. Jin Adrian Koh, S. Bauer, and Z. Suo, "Model of dissipative dielectric elastomers," *Journal of Applied Physics*, vol. 111, no. 3, Article ID 034102, 2012.
- [37] J. Huang, T. Li, C. Chiang Foo, J. Zhu, D. R. Clarke, and Z. Suo, "Giant, voltage-actuated deformation of a dielectric elastomer under dead load," *Applied Physics Letters*, vol. 100, no. 4, Article ID 041911, 2012.
- [38] A. N. A. Gent, "A new constitutive relation for rubber," *Rubber Chemistry Technology*, vol. 69, no. 1, pp. 59–61, 1996.
- [39] M. Wissler and E. Mazza, "Mechanical behavior of an acrylic elastomer used in dielectric elastomer actuators," *Sensors and Actuators A: Physical*, vol. 134, no. 2, pp. 494–504, 2007.
- [40] S. Michel, X. Q. Zhang, M. Wissler, C. Löwe, and G. Kovacs, "A comparison between silicone and acrylic elastomers as dielectric materials in electroactive polymer actuators," *Polymer International*, vol. 59, no. 3, pp. 391–399, 2010.